Gravitational Waves Memory
from Hyperbolic Black Hole Binaries

Dissertation

zur

Erlangung der naturwissenschaftlichen Doktorwürde

(Dr. sc. nat.)

vorgelegt der

Mathematisch-naturwissenschaftlichen Fakultät

der

Universität Zürich

von

LORENZO DE VITTORI

von Dino, TI

Promotionskomitee

Prof. Dr. Philippe Jetzer (Vorsitz und Leitung)
Prof. Dr. Gino Isidori
Prof. Dr. Achamveedu Gopakumar
Dr. Carlos Sopuerta

Zürich, 2015

Summary

The best theory describing gravity we know so far is the General Theory of Relativity (GR). Mostly developed by Albert Einstein in Zürich with the help of his classmate and friend Marcel Grossmann, the theory was completed in 1915, hundred years ago. General Relativity relies on a description of gravity through Riemannian geometry on curved manifolds, connecting thus gravitation to differential geometry. Distant masses attract each other because they deform the surrounding spacetime so that geodesics of other objects passing by bend towards them. One of the most remarkable consequences of this mathematical approach is that accelerated masses produce tiny and periodic perturbations in the curvature of spacetime. A first description of such wave solutions to the linearized equations governing GR was published in 1916, and two years later a complete treatment of the subject was finalized, and those perturbations were given the name "Gravitational Waves".

The chance of detecting any Gravitational Wave (GW) was thought to be very small, due to their extremely tiny nature, and no particular effort in this sense was undertaken. After a century of theoretical studies and experimental developments, we are almost ready to proof the opposite. Gravitational waves are expected to be directly detected for the first time within the next few years, opening a new window onto the observable universe and starting a new era in astronomy and astrophysics.
Claiming a first GW detection is the goal of the last decades of endeavours, but the way to it goes through both highly sensitive experimental settings and accurate theoretical prediction of the expected signal. The present work is part of this common effort and aims to improve the description of gravitational waveforms for some plausible sources radiating in the frequency band to which new generation detectors are sensitive.

In the first part of this thesis we develop a prescription to generate accurate gravitational wave signals from hyperbolic collisions of compact objects, like black holes or neutron stars. Our method is valid for arbitrary eccentricities and masses, and takes into account radiation reaction effects and spin precession, due to spin-orbit coupling correction terms. A major result arising from the simulations we performed to generate waveform templates, is the presence of a non-vanishing component of the metric perturbation: the gravitational memory effect.
In the second part of this work we study the memory in further detail, we analyze its behaviour depending on the parameters of the collision, and find a generalized theoretical prediction of this imprint on the metric left behind by the passage of a gravitational wave.
Finally, we devote our attention to the similar case of compact binaries moving along elliptic orbits, where the periodic eccentric motion is largely influenced by spin-orbit and spin-spin couplings, and where therefore a higher post-Newtonian order description of the dynamics is required in order to get accurate waveform templates.

Zusammenfassung

Die zurzeit beste Theorie der Gravitation ist die Theorie der Allgemeinen Relativität (ART). Hauptsächlich von Albert Einstein in Zürich mit der Hilfe von seinem Studienkollegen und Freund Marcel Grossmann entwickelt, wurde die Theorie im Jahre 1915 vervollständigt, vor genau hundert Jahren. Sie basiert auf einer Beschreibung des Gravitationsfeldes durch die Riemannsche Geometrie in gekrümmten Mannigfaltigkeiten, und bringt somit die Gravitation mit der Differentialgeometrie in Verbindung. Die Tatsache, dass entfernte Massen sich gegenseitig anziehen, ist darauf zurückzuführen, dass sie die umliegende Raumzeit krümmen und verzerren, so dass Geodäten von anderen vorbeigehenden Objekten zu ihnen gebogen werden. Eine bemerkenswerte Folge dieser mathematischen Einstellung ist, dass beschleunigte Massen kleine periodische Störungen in der Krümmung von Raumzeit erzeugen. Eine erste Beschreibung dieser Wellenlösungen zu den linearisierten Feldgleichungen der ART wurde im Jahre 1916 veröffentlicht. Zwei Jahre später wurde eine vollständigere Behandlung herausgegeben und diesen Störungen den Namen "Gravitationswellen" gegeben.

Die Möglichkeit, solche Gravitationswellen überhaupt messen zu können, wurde aufgrund ihrer extrem schwachen Natur eher gering geschätzt. Keine besondere Versuche wurden deshalb in diesem Sinne unternommen. Nach einem Jahrhundert von theoretischer Forschung und experimentellen Entwicklungen sind wir fast bereit, das Gegenteil zu zeigen. Erste direkte Nachweise der Gravitationswellen sind innerhalb der nächsten wenigen Jahre erwartet. Damit wird bald ein neues Fenster auf das beobachtbare Universum geöffnet und eine neue Ära der Astronomie und der Astrophysik wird anfangen.
In den letzten Jahrzehnten hat man sich sehr um eine erste Detektion einer Gravitationswelle bemüht. Der Weg dazu geht aber nicht an hochempfindlichen Messgeräten und genauen theoretischen Vorhersagen vorbei. Die vorliegende Arbeit ist Teil dieser gemeinsamen Leistung und beabsichtigt, die Beschreibung der Wellenformen für einige möglichen Quellen zu verbessern, die im empfindlichen Frequenzbereich der neuen Detektoren ausstrahlen.

Im ersten Teil dieser Dissertation entwickeln wir eine neue Methode, um genaue Wellensignale vorherzusagen, die aus hyperbolischen Kollisionen von kompakten Objekten – wie schwarzen Löchern oder Neutronensternen – entstehen. Unsere Methode gilt für beliebige Exzentrizitäten und Massen und berücksichtigt unter anderem Strahlungsrückwirkungseffekte sowie die Spin-Präzession, bedingt durch Spin-Orbit Korrekturterme in der Dynamik.
Ein wichtiges Ergebnis von den ausführlich durchgeführten Simulationen, um Wellenformen zu erzeugen, ist die Existenz einer nicht verschwindenden Komponente der Feldstörung: der sogenannte *Memory effect*.
Im zweiten Teil dieser Arbeit untersuchen wir dieses "Gedächtnis" genauer, studieren sein Verhalten in Abhängigkeit der Kollisionsparameter, und finden eine allgemeine theoretische Vorhersage dieser von der Gravitationswelle auf der Metrik hinterlassenen Spur.
Schliesslich widmen wir uns dem Studium einer ähnlichen Situation, in welcher ein binäres System sich auf einer elliptischen Bahn bewegt. Die periodische exzentrische Bewegung ist von Spin-Effekten stark beeinflusst. In diesem Fall ist deshalb eine Beschreibung der Dynamik auf höherer post-Newtonscher Ordnung erforderlich, um ein genaues Gravitationswellen-Signal bestimmen zu können.

Acknowledgements

It is only because of the support of many people that I could accomplish my doctoral studies. I wish to give you all many thanks and I would like, in the following, to address the people who influenced me most, being aware that I cannot list everybody and fully express my gratitude.
First of all, I would like to express my profoundest appreciation to my principal supervisor *Prof. Dr. Philippe Jetzer* for the continuous support of my PhD study and research, for his patience, motivation and enthusiasm. Besides providing me the opportunity to do my doctorate at the University of Zurich and to participate in many conferences, schools and research stays, he introduced me to the fascinating field of Gravitational Wave Astronomy. I could also appreciate all the many interesting discussions that often extended beyond physics.

I am particularly grateful to my colleagues who contributed significantly to my scientific research. *Dr. Antoine Klein* guided me through the Masters' thesis and was an inspiration while starting my PhD career. He also helped me publishing the first paper, joined me in many conferences and hosted me in the idyllic campus of the University of Mississippi, which I really appreciated. *Prof. Dr. Achamveedu Gopakumar* sought after me during a conference in Paris proposing me a collaboration which turned out to be crucial for the accomplishment of this thesis. I am very thankful for his patience and carefulness while working with me, and for the very important advices through which I could deepen my knowledge in many aspects of astrophysics. It was a pleasure to host him at the University of Zurich.
I also want to express my special gratitude to *Prof. Dr. Diethard Klatte* for giving me the chance to finance my doctorate as a teaching assistant in mathematics at the institute for Quantitative Business Administration. I particularly appreciated the great atmosphere I experienced in the Physics Institute. *Esther Meier* and *Regina Schmid* provided me solutions to all my administrative problems and always contributed to the nice family atmosphere we breathe in the institute.

A special thank goes to my office colleagues: *Simone Balmelli* who endured my company since secondary school, always listening to my concerns and giving me precious help during all these years, together with *Cédric Huwyler*, *Mario Lubini*, *Crescenzo Tortora*, *Lionel Philippoz* with whom I shared many great moments, especially during conferences and research stays, *Andreas Bleuler*, *Sebastian Elser*, *Yannick Boetzel*, *Andreas Schaerer*, *Davide Fiacconi*, and many others. I had a great time with all them, also and especially outside the University.
I am also very thankful to all the residents of *Allenmoos* for completing my life as a PhD student with the cheerfulness and the happiness of a second family.

Finally, I would like to thank my family. My parents *Chiara* and *Carlo*, my brothers *Francesco* and *Marco* and my sister *Cecilia*, as well as my grandparents, for the big inspiration they have been to me. Since I cannot fully express my gratitude, I will tell them personally.

I am most grateful to all my friends who make my life so happy.

Thank You.

Lorenzo De Vittori Zürich, 1 October 2015

“I dedicate my thesis to all those whose worldline, at some point in spacetime - after having being wandering through the curved geometries of the universe - came to cross the worldline of the Studentenhaus Allenmoos, and may changed their own paths because of this four-dimensional event. ”

Publications

Chapter 4 is based on works published in Phys. Rev. D **86**, 044017 (2012). [1]

Chapter 5 is based on works published in Phys. Rev. D **90**, 124066 (2014). [2]

Chapter 6 is based on works submitted to Phys. Rev. D. [3]

Chapter 7 is based on works still in preparation and not yet published. [4]

Contents

Chapter 1

Introduction

"La plus haute des activités humaines est la recherche de la vérité. Recherche et enseignement se complètent l'un l'autre. L'enseignement empêche le chercheur de s'enfermer dans son problème, le force à étendre ses connaissances et à préciser ses idées. Lorsqu'il pense aux vérités de la foi, il sait que ses connaissances sur les microbes, les atomes ou les soleils ne lui seront ni un secours ni une gêne pour adhérer à la lumière inaccessible et qu'il lui restera, comme à tout homme, à tâcher de se faire un coeur de petit enfant pour entrer dans le Royaume des Cieux. Ainsi Foi et Raison, sans mélange inconvenant ni conflit imaginaire, s'unissent dans l'unité de l'activité humaine."

G. E. Lemaître

Albert Einstein completed his General Theory of Relativity in 1915 [5], one hundred years ago, after a long study of the mathematics governing curved manifolds and generally covariant tensors in differential geometry, with the help of his friend Marcel Grossmann, in Zürich [6,7].

Even before General Relativity (GR) was derived and fully described, many physicists and mathematicians were struggling with the philosophical question about why electromagnetic waves – solutions to the differential equations resumed by James Clerk Maxwell in 1865 [8] – are propagating at a speed which is numerically the same as the speed of light. The theory of Special Relativity seemed to answer many of those issues, by means of invariant Lorentz transformations. However, every attempt to describe gravity within the special relativistic framework failed while considering that it cannot be an action–at–a–distance theory.
In some sense, this fact already required and implied the existence of gravitational waves (GWs) in the theory of gravitation. Indeed, the French mathematician Henri Poincaré proposed the so-called *ondes gravifiques* [9] in 1905.
Once General Relativty was fully formulated, it did not take long before first solutions to Einstein's field equations were derived [10–12].
Already in 1916, just one year later, Einstein himself proposed the description of gravitational waves as solutions to the linearized equations [13,14], setting therewith a milestone in history of human astronomy while opening a new era and a new window on the universe.

Despite the importance of this achievement, during the next forty years there was only little progress in the field, partly due to the fact that GWs amplitudes were clearly very small and

gave no realistic hope to be ever seen nor measured – Einstein himself said repeatedly that it would be impossible to ever detect them – but also because of much controversy and doubts on their existence, even at a theoretical level [15, 16].
In 1959, Bondi, Pirani and Robinson published an important paper [16] on the exact plane wave solution with cylindrical symmetry and in particular about the fact that gravitational waves do carry energy and angular momentum out of the source, and exist not only in the weak-field approximation but also in full General Relativity.
This means that gravitational waves cannot be "gauged away", i.e. set to zero with an appropriate choice of the reference frame or coordinate transformation. This was the starting point of a new golden era of General Relativity and with it of the quest for gravitational waves.
After some pioneering experimental work by Joseph Weber, in 1974 Russel Alan Hulse and Joseph Hooton Taylor [17] discovered a binary pulsar: a rapidly rotating, highly magnetized neutron star emitting a pulse every 59 milliseconds, which together with another neutron star is orbiting around the common center of mass with a period of about 7.7 hours. Through an accurate analysis of the decay of the orbital period and the periastron shift, they noticed that the binary system was slowly loosing energy, possibly carried away by gravitational waves [18]. After many years of accurate measurments [19], we know that the observed rate of change of the period agrees with predictions of General Relativity to better than 0.03 % [20].

Since the discovery of the Hulse-Taylor pulsar, during the last forty years, impressive advances have occurred, both on the theoretical and the experimental side. A huge development in the research on the modelling of astrophysical and cosmological sources of gravitational waves is going on. Analytical methods predicting waveforms, such as the post-Newtonian expansion or the Effective–One–Body approach [21–23] are nowadays validated and compared with simulations from Numerical Relativity, which very rapidly won recognition and established itself in the last decade as one of the most promising techniques to generate accurate waveform templates, especially in late phases of binary sources.
On the experimental side, a huge effort has been done in building highly sensitive detectors on earth. In 1992, Kip Thorne, Ronald Drever and Rainer Weiss founded the Laser Interferometer Gravitational-wave Observatory (LIGO), and after the very first generation of interferometric detectors, such as GEO600 in Hannover, Germany, the initial versions of LIGO, in the US, and Virgo, in Italy, a new generation is currently starting scientific operations under the name of advanced LIGO and advanced Virgo. The sensitivity is incredibly high, aiming to detect strain amplitudes of about 10^{-22} in a wide range of frequencies [24], expecting to see compact binary inspirals and pulsars. We are currently at the dawn of the first direct detections of gravitational waves, right hundred years after the first articles by Einstein.

In this thesis we provide some prescriptions to generate accurate post-Newtonian waveform templates for different systems, and we study some aspects of the structure of the resulting gravitational waves.

In Chapter 2 we introduce the basics of gravitational wave theory and the framework of linearized theory needed for building waveforms, the main goal of the present work. It is mostly based on [25], [26], and [27]. The interested reader may find there additional material and further information.
In Chapter 3 we give some brief insights in the way we describe the physics of the source and shape the amplitude and the phasing of the waveform. Afterwards we explain how the passage of a gravitational wave interacts with an ideal detector, and how real detector work.

Finally we discuss the prospects of detections in this very exciting moment and in the years to come.
Chapters from 4 to 7 are mainly based on the publications [1], [2], [3], and [4], respectively. First we compute the energy spectrum of an unbound interaction between compact masses and compare it with available results for the parabolic limit, in Chapter 4. We extend this work in Chapter 5, where we provide a 1.5 post-Newtonian order accurate prescription for computing waveforms radiated by hyperbolic encounters of spinning compact binaries, with arbitrary mass and spin orientation. In the case of unbound interactions we notice an interesting behaviour of the metric: the memory effect, which is a non-vanishing term in the perturbation, leaving an imprint of the passage of the gravitational wave for all times. In Chapter 6 we study the memory effect in detail and show some dependencies on initial parameters, such as spin orientation, eccentricity and mass ratio. Later on, in Chapter 7, we turn our attention to the more common elliptic case, very well studied in the literature. We provide a quasi-Keplerian parametrization of the dynamics of an eccentric binary, at full second post-Newtonian order, stressing the importance of taking into account eccentricity and spins while generating waveform templates, and completing available results with a new correction term and a better suitable parametrization.
In Chapter 8 we finally resume our work and briefly discuss some of the most important results.

Conventions

Throughout this thesis we will use the following conventions, if not stated differently.
Greek indices denote four-dimensional spacetime indices, as

$$x^\mu \in \{x^0, x^1, x^2, x^3\} = \{ct, x, y, z\} \,,$$

while latin indices denote three-dimensional space indices

$$x^i \in \{x^1, x^2, x^3\} = \{x, y, z\} \,.$$

Boldface symbols denote three-dimensional vectors. The Euclidean scalar product is written with a central dot, while the three-dimensional vector product is denoted by a cross, like

$$\boldsymbol{A}\cdot\boldsymbol{B} = \sum_{i=1}^{3} A^i\, B^i \,, \qquad\qquad (\boldsymbol{A}\times\boldsymbol{B})_i = \epsilon_{ijk}\, A^j\, B^k \,,$$

where ϵ_{ijk} is the three-dimensional totally antisymmetric Levi-Civita symbol with $\epsilon_{123} = +1$. Three-dimensional unit vectors are denoted by a hat, while the norm is written with the non-boldface symbol, as

$$A = |\boldsymbol{A}| \,, \qquad\qquad \hat{\boldsymbol{A}} = \frac{\boldsymbol{A}}{A} \,.$$

We define partial derivatives as

$$\partial_\mu = \frac{\partial}{\partial_\mu} = \left(\frac{1}{c}\partial_t, \partial_i\right) \,,$$

We do not denote derivatives with commas in the indices, as sometimes done in the literature, nor semicolons to denote covariant derivatives.
A dot denotes the time derivative

$$\dot{f}(t) = \frac{\mathrm{d}f}{\mathrm{d}t} \, .$$

The flat spacetime metric is

$$\eta_{\mu\nu} = (-,+,+,+) \, ,$$

while we denote the curved spacetime metric by $g_{\mu\nu}(x)$ and its determinant by g.
The invariant length element is then given by

$$ds^2 = g_{\mu\nu} \, dx^\mu dx^\nu = -c^2 d\tau^2 \, .$$

We use the Einstein summation rule, where repeated upper and lower indices sum over

$$A^\mu \, B_\mu = \sum_{\mu=0}^{3} A^\mu \, B_\mu \, .$$

Then the Christoffel symbols can be written as

$$\Gamma^\rho_{\mu\nu} = \frac{1}{2} g^{\rho\sigma} (\partial_\mu g_{\sigma\nu} + \partial_\nu g_{\sigma\mu} - \partial_\sigma g_{\mu\nu}) \, ,$$

and the Riemann tensor is given by

$$R^\mu{}_{\nu\rho\sigma} = \partial_\rho \Gamma^\mu_{\nu\sigma} - \delta_\sigma \Gamma^\mu_{\nu\rho} + \Gamma^\mu_{\alpha\rho} \Gamma^\alpha_{\nu\sigma} - \Gamma^\mu_{\alpha\sigma} \Gamma^\alpha_{\nu\rho} \, .$$

The Ricci tensor is the contraction of the Riemann tensor $R_{\mu\nu} = R^\alpha{}_{\mu\alpha\nu}$, while the Ricci scalar is the contraction of the Ricci tensor, and is given by $R = g^{\mu\nu} R_{\mu\nu}$.

The energy-momentum tensor $T^{\mu\nu}$ is defined by the variation of the matter action S_M under a metric transformation $g_{\mu\nu} \to g_{\mu\nu} + \delta g_{\mu\nu}$, through the relation

$$\delta S_M = \frac{1}{2c} \int d^4x \, \sqrt{-g} \, T^{\mu\nu} \, \delta g_{\mu\nu} \, .$$

Einstein's Field Equations read

$$R_{\mu\nu} - \frac{1}{2} \, g_{\mu\nu} \, R = \frac{8\pi G}{c^4} \, T_{\mu\nu} \, .$$

Our convention on the Fourier transform of a signal h, denoted by a tilde, is the common one in gravitational wave science, as long as it is not stated differently, and reads

$$\tilde{h}(f) = \int h(t) \, e^{2\pi i f t} \, dt \qquad \Longleftrightarrow \qquad h(t) = \int \tilde{h}(f) \, e^{-2\pi i f t} \, df \, .$$

Chapter 2

General Relativity and Gravitational Waves

"Non quia difficilia sunt non audemus,
sed quia non audemus difficilia sunt."

L. A. Seneca

2.1 A very brief guide to General Relativity

General Relativity is governed by the set of differential *Einstein's field equations* on a four-dimensional manifold, which we usually call *spacetime*. At some point $x = (ct, x^1, x^2, x^3)$ in spacetime the field equations read:

$$R_{\mu\nu} - \frac{1}{2} g_{\mu\nu} R = \frac{8\pi G}{c^4} T_{\mu\nu} . \tag{2.1}$$

The mass-energy density is represented here on the right hand side by the energy-momentum tensor $T_{\mu\nu}$, which contains all the curvature-generating fields. On the left hand side, the curvature is expressed via the *Ricci tensor* $R_{\mu\nu} = R^{\rho}{}_{\mu\rho\nu}$ and the *scalar curvature* $R = R^{\mu}{}_{\mu}$, which are contractions of the Riemann tensor $R^{\rho}{}_{\sigma\mu\nu}$ that measures how vectors change when they are parallel-transported along different paths to the same point. The presence of a non-zero mass-energy density is therefore responsible for a non-zero curvature of the spacetime manifold, governing the motion of both massive and massless bodies. John A. Wheeler expressed it with the following words: "*Matter tells spacetime how to curve, and curved spacetime tells matter how to move.*" [25]
General Relativity is said to be form-covariant, i.e. is invariant under a huge symmetry group, the group of all possible smooth coordinate transformations. This fact arises from the tensorial formulation of the above equations, and has some important consequences. The metric on the curved manifold is given by the tensor $g_{\mu\nu}$ and allows to express the length element $\mathrm{d}s$ in a given coordinate x as

$$\mathrm{d}s^2 = g_{\mu\nu}\, dx^\mu dx^\nu , \tag{2.2}$$

where the dx^μ are coordinate differentials. For a time-like curve – defined by the condition that $\mathrm{d}s^2 < 0$ at all times – we can define the proper time τ through

$$c^2 \mathrm{d}\tau = -\mathrm{d}s^2 = -g_{\mu\nu} dx^\mu dx^\nu , \tag{2.3}$$

which expresses the time measured by a clock traveling along the path. In terms of the four-velocity $u^\mu = \frac{\mathrm{d}x^\mu}{\mathrm{d}\tau}$ we can write this condition as

$$g_{\mu\nu}u^\mu u^\nu = -c^2 \,. \tag{2.4}$$

Now, since one can link two sets of coordinates through a diffeomorphism $x^\mu \to x'^\mu(x)$ and the length element has to be invariant under coordinate transformations, one can write it as $\mathrm{d}s^2 = g_{\mu\nu}(x)\, dx^\mu dx^\nu = g'_{\mu\nu}(x')\, dx'^\mu dx'^\nu$. This implies that the metric transforms as

$$g_{\mu\nu} \to g'_{\mu\nu}(x') = \frac{\partial x^\rho}{\partial x'^\mu}\frac{\partial x^\sigma}{\partial x'^\nu} g_{\rho\sigma}(x) \,. \tag{2.5}$$

We call this the *gauge symmetry* of General Relativity.

In order to find the equations of motion for a test particle one first needs to find a connection between the metric tensor $g_{\mu\nu}$ and the Riemann tensor $R^\rho{}_{\sigma\mu\nu}$. This is what we shall call the *parallel transport* of vectors, and is defined through the *covariant derivative* $\nabla_{\partial_\mu}\partial_\nu = \Gamma^\rho_{\mu\nu}\partial_\rho$, where we introduce the notation $\partial_\mu = \partial/\partial x^\mu$. The covariant derivative shows how a basis vector ∂_μ of the tangent space is differentiated along another basis vector ∂_ν at some point on the manifold. One wants to define the tensor $\Gamma^\rho_{\mu\nu}$ in order that $\nabla g = 0$ always holds. This happens if one imposes the following definition

$$\Gamma^\rho_{\mu\nu} = \frac{1}{2} g^{\rho\sigma}(g_{\mu\sigma,\nu} + g_{\nu\sigma,\mu} - g_{\mu\nu,\sigma}) \,. \tag{2.6}$$

These are called the *Christoffel symbols*. Through them we are able to express the Riemann tensor as

$$R^\rho{}_{\sigma\mu\nu} = \partial_\mu\Gamma^\rho_{\sigma\nu} - \partial_\nu\Gamma^\rho_{\sigma\mu} + \Gamma^\rho_{\alpha\mu}\Gamma^\alpha_{\sigma\nu} - \Gamma^\rho_{\alpha\nu}\Gamma^\alpha_{\sigma\nu} \,, \tag{2.7}$$

and relate it to the metric tensor. In the special case of a flat spacetime manifold, the metric tensor $g_{\mu\nu}$ reduces to the Minkowski tensor

$$\eta_{\mu\nu} = \begin{pmatrix} -1 & 0 & 0 & 0 \\ 0 & 1 & 0 & 0 \\ 0 & 0 & 1 & 0 \\ 0 & 0 & 0 & 1 \end{pmatrix} \tag{2.8}$$

and therefore the Christoffel symbols as well as the Riemann tensor vanish.

The motion of a test particle on the curved spacetime manifold occurs on a *geodesic*, a path on which the covariant derivative of the velocity vanishes. It is the worldline that minimizes the distance between two points, and can be described through the *geodesic equation*

$$\frac{\mathrm{d}^2x^\rho}{\mathrm{d}\tau^2} + \Gamma^\rho_{\mu\nu}\frac{\mathrm{d}x^\mu}{\mathrm{d}\tau}\frac{\mathrm{d}x^\nu}{\mathrm{d}\tau} = 0 \,. \tag{2.9}$$

While the path of a freely falling body follows from the geodesic equation, an accelerated mass will not stay on the same geodesic during the action of a given force. Its new geodesic can therefore be written as $x^\mu(\tau) + \xi^\mu(\tau)$. The deviation of the two geodesics from each other can be computed noting that x^μ satisfies (2.9), while $x^\mu(\tau) + \xi^\mu(\tau)$ satisfies

$$\frac{\mathrm{d}^2(x^\mu + \xi^\mu)}{\mathrm{d}\tau^2} + \Gamma^\mu_{\nu\rho}(x+\xi)\,\frac{\mathrm{d}(x^\nu + \xi^\nu)}{\mathrm{d}\tau}\,\frac{\mathrm{d}(x^\rho + \xi^\rho)}{\mathrm{d}\tau} = 0 \,. \tag{2.10}$$

Now, if $|\xi^\mu(\tau)|$ is small compared to $g_{\mu\nu}$, as it is reasonable to assume with a GW, we can take the difference between (2.10) and (2.9), expand to linear order in ξ and get

$$\frac{\mathrm{d}^2\xi^\mu}{\mathrm{d}\tau^2} + 2\Gamma^\mu_{\nu\rho}(x)\frac{\mathrm{d}x^\nu}{\mathrm{d}\tau}\frac{\mathrm{d}\xi^\rho}{\mathrm{d}\tau} + \xi^\sigma\partial_\sigma\Gamma^\mu_{\nu\rho}(x)\frac{\mathrm{d}x^\nu}{\mathrm{d}\tau}\frac{\mathrm{d}x^\rho}{\mathrm{d}\tau} = 0\,, \tag{2.11}$$

and simplifying by using the covariant derivative, we get the *equation of the geodesic deviation*

$$\frac{\mathrm{D}^2\xi^\mu}{\mathrm{d}\tau^2} = -R^\mu{}_{\nu\sigma\rho}\,\xi^\rho\,u^\nu u^\sigma\,. \tag{2.12}$$

This result shows how the Riemann tensor is responsible for the tidal gravitational force experienced by two nearby time-like geodesics.

At a macroscopic level, all physical processes in the universe are governed by the Eintein's field equation and the geodesic equation. Using different reference frames to write these equations, we can get many insights on how ideal test masses or detectors behave when the gravitational field varies. In section 2.3 we will have a more detailed look on this aspect of the theory. In the next section we discuss how gravitational waves emerge from General Relativity by solving these equations through the linearized theory.

2.2 From GR to GWs: Linearized theory

2.2.1 Linearized Eintein's field equations

As a first step towards the gravitational wave solution, we wish to study how the Einstein's field equations expand around the flat spacetime metric. We consider therefore a flat background with the Minkowski metric $\eta_{\mu\nu}$ with a small perturbation $h_{\mu\nu}$ with $|h_{\mu\nu}| \ll 1$. We can write

$$g_{\mu\nu} = \eta_{\mu\nu} + h_{\mu\nu}\,. \tag{2.13}$$

From this arises the linearized theory. Its basic interpretation is the following: the sources of perturbations are assumed to move on "classical" trajectories, i.e. on flat spacetime metric $\eta_{\mu\nu}$ along paths determined by their mutual influence, e.g. the description of a binary system would be done using Newtonian dynamics, rather than full General Relativity. On the other hand, the response of a test mass to these perturbations is assumed to happen on a general relativistic metric, where $g_{\mu\nu} = \eta_{\mu\nu} + h_{\mu\nu}$ and where we only consider terms up to first order in $h_{\mu\nu}$ when evaluating the Christoffel symbols or the Riemann tensor.
To compute the linearized field equations we evaluate one by one these tensors at linear order, i.e. neglecting terms of the order $\mathcal{O}(h^2)$. Recall that in linearized theory we raise and lower indices with the flat metric $\eta_{\mu\nu}$. The linearized Christoffel symbols are

$$\Gamma_{\rho\mu\nu} = \frac{1}{2}\eta_\rho{}^\sigma(\partial_\nu h_{\mu\sigma} + \partial_\mu h_{\nu\sigma} - \partial_\sigma h_{\mu\nu})\,, \tag{2.14}$$

while the linearized Riemann tensor becomes

$$R_{\mu\nu\rho\sigma} = \frac{1}{2}(\partial_\nu\partial_\rho h_{\mu\sigma} + \partial_\mu\partial_\sigma h_{\nu\rho} - \partial_\mu\partial_\rho h_{\nu\sigma} - \partial_\nu\partial_\sigma h_{\mu\rho})\,. \tag{2.15}$$

For the field equations one still needs to evaluate the linearized Ricci tensor and scalar curvature. We define therefore the flat space *d'Alembert operator* $\Box = \partial_\mu\partial^\mu = \eta_{\mu\nu}\partial^\mu\partial^\nu$ and the trace of $h_{\mu\nu}$ as

$$h = \eta^{\mu\nu}h_{\mu\nu}\,. \tag{2.16}$$

Contracting the linearized Riemann tensor one gets then the Ricci tensor

$$R_{\mu\nu} = R^{\rho}{}_{\mu\rho\nu} = \frac{1}{2}(\partial^{\rho}\partial_{\mu}h_{\rho\nu} + \partial^{\rho}\partial_{\nu}h_{\rho\mu} - \Box\, h_{\mu\nu} - \partial_{\mu}\partial_{\nu}h)\,, \tag{2.17}$$

and the scalar curvature

$$R = R^{\mu}{}_{\mu} = \partial^{\rho}\partial^{\mu}h_{\rho\mu} - \Box\, h\,. \tag{2.18}$$

In order to write the field equations in a compact way, we define the trace-reversed metric

$$\bar{h}_{\mu\nu} = h_{\mu\nu} - \frac{1}{2}\eta_{\mu\nu}\, h\,, \tag{2.19}$$

and we note that $\bar{h} = -\,h$ and therefore the inversion of (2.19) is simply $h_{\mu\nu} = \bar{h}_{\mu\nu} - \frac{1}{2}\eta_{\mu\nu}\,\bar{h}$. Using these results, (2.1) reduces to the *linearized Einstein's field equations*

$$\Box\,\bar{h}_{\mu\nu} + \eta_{\mu\nu}\partial^{\rho}\partial^{\sigma}\bar{h}_{\rho\sigma} - \partial^{\rho}\partial_{\nu}\bar{h}_{\mu\rho} - \partial^{\rho}\partial_{\mu}\bar{h}_{\nu\rho} = -\frac{16\pi G}{c^4}\,T_{\mu\nu}\,. \tag{2.20}$$

At this point we notice that in linearized theory $h_{\mu\nu}$ is invariant under the group of finite Poincaré transformations, i.e. the group of translations and Lorentz transformations[1], as well as under some infinitesimal transformations of the type

$$x^{\mu} \to x'^{\mu} = x^{\mu} + \xi^{\mu}(x)\,, \tag{2.21}$$

where we require that the derivative $|\partial_{\mu}\xi_{\nu}|$ is at most of the same order of smallness as $|h_{\mu\nu}|$. To first order, using the gauge symmetry (2.5), the perturbation tensor $h_{\mu\nu}$ transforms as

$$h_{\mu\nu}(x) \to h'_{\mu\nu}(x') = h_{\mu\nu}(x) - (\partial_{\mu}\xi_{\nu} + \partial_{\nu}\xi_{\mu})\,, \tag{2.22}$$

which for the trace-reversed metric translates to

$$\bar{h}_{\mu\nu}(x) \to \bar{h}'_{\mu\nu}(x') = \bar{h}_{\mu\nu}(x) - (\partial_{\mu}\xi_{\nu} + \partial_{\nu}\xi_{\mu} - \eta_{\mu\nu}\partial_{\rho}\xi^{\rho})\,. \tag{2.23}$$

The derivative of the perturbation behaves as

$$\partial^{\nu}\bar{h}_{\mu\nu} \to (\partial^{\nu}\bar{h}_{\mu\nu})' = \partial^{\nu}\bar{h}_{\mu\nu} - \Box\,\xi_{\mu}\,, \tag{2.24}$$

and since we are always able[2] to impose $\Box\,\xi_{\mu} = \partial^{\nu}\bar{h}_{\mu\nu}$, we have the gauge freedom to pick a reference frame where

$$\partial^{\nu}\bar{h}_{\mu\nu} = 0\,. \tag{2.25}$$

We usually call it the *Lorentz gauge*, in analogy with electrodynamics. The choice of this gauge imposes four conditions to the 4×4 symmetric tensor $h_{\mu\nu}$. This means that the 10 initial independent components are reduced to six. Physically speaking, having a gauge freedom corresponds to the freedom of describing the same physical process in any reference frame with its proper coordinate system. In the same way, choosing a specific gauge means going to a fixed frame. This is what happens while imposing the Lorentz gauge (2.25).

[1]Note that, inserting (2.22) into (2.15), under the gauge freedom also the linearized Riemann tensor can be shown to be invariant, as the perturbation tensor $h_{\mu\nu}$, while under arbitrary transformations through diffeomorphisms in full non-linearized General Relativity it is rather covariant.

[2]For a detailed treatment of this gauge we suggest the interested reader to find further insights e.g. in [25,26].

If we now consider the linearized Einstein's field equations (2.20) under the Lorentz gauge (2.25), we see that the last three terms on the left hand side simply vanish, and thus we are left with a common wave equation in $\bar{h}_{\mu\nu}$ that reads

$$\Box \bar{h}_{\mu\nu} = -\frac{16\pi G}{c^4} T_{\mu\nu} . \tag{2.26}$$

The propagation of perturbation in the linearized theory appears thus as a wave, which we will call a *gravitational wave* (from now on simply GW), with amplitude $\bar{h}_{\mu\nu}(x)$. Within linearized theory, Equation (2.26) is the main tool for computing generation of GWs from any source. However, to study the propagation and visualize the action of GWs with test masses and eventually with a detector, we want to look at the region outside the source, where the energy-momentum tensor $T_{\mu\nu}$ vanishes. In the next section we will see how the metric can be further simplified in vacuum with an appropriate choice of more gauge conditions.

2.2.2 The transverse traceless gauge

We turn now our attention to vacuum solutions of (2.26), where $T_{\mu\nu} = 0$ and hence the wave equation simplifies to

$$\Box \bar{h}_{\mu\nu} = 0 . \tag{2.27}$$

Since the coordinates are given by $x^\mu = (ct, x^1, x^2, x^3)$ and the derivative is $\partial_\mu = (\frac{1}{c}\partial_t, \partial_i)$, the flat space d'Alembert operator can be written as $\Box = -\frac{1}{c^2}\partial_t^2 + \nabla^2$. This implies that any solution of (2.27), which is a gravitational wave, propagates at the speed of light.

In this empty region outside the source, the condition (2.25) does not fix the gauge freedom completely. In fact, one can choose the components of ξ^μ in the coordinate transformation (2.21) such that

$$\Box \xi_\mu = 0 . \tag{2.28}$$

These are four additional constraints we can freely set. The first will be the choice of ξ_0 such that the trace vanishes, $\bar{h} = 0$. In this case, it is straightforward to see that $\bar{h}_{\mu\nu} = h_{\mu\nu}$. Hence in the following we will only refer to the waveform as $h_{\mu\nu}$. The next three constraints we will put are the choice of the ξ_i components, so that $h_{0i} = 0$. Applied on (2.25) we can reduce the Lorentz gauge to $\partial^0 h_{00} = 0$, since for $\mu = 0$ the second term in the relation $\partial^0 h_{00} + \delta^i h_{0i} = 0$ vanishes. This means that the component h_{00} is constant in time, and we will fix it to $h_{00} = 0$ at all times.
In conclusion, this whole set of conditions can be resumed as

$$h_{0\mu} = 0 , \qquad h^i{}_i = 0 , \qquad \partial^j h_{ij} = 0 . \tag{2.29}$$

This is called the *transverse traceless gauge*, or simply the *TT gauge*, since the trace vanishes and the non-zero components of the tensor $h_{\mu\nu}$ are in the plane transverse to the direction of propagation. Note that the 10 initial independent components, reduced to six with the Lorentz gauge, were now further reduced in the TT gauge through four more conditions, and thus we are left with just two degrees of freedom. Furthermore notice that the TT gauge can only be chosen outside the source, since inside $\Box \bar{h}_{\mu\nu} \neq 0$ and only the Lorentz gauge can be taken.
In the following we will denote the metric in the TT gauge by h_{ij}^{TT}.

Solutions to equation (2.27) in the TT gauge are plane waves of the form $h_{ij}^{TT}(x) = e_{ij}(\boldsymbol{k})e^{ikx}$, with $k^\mu = (\omega/c, \boldsymbol{k})$ and $\omega/c = |\boldsymbol{k}|$, and where $e_{ij}(\boldsymbol{k})$ is called the *polarization tensor*. From

(2.29) we know that, once we have fixed the propagation direction along a unit vector $\hat{\boldsymbol{n}} = \boldsymbol{k}/|\boldsymbol{k}|$, the non vanishing components of h_{ij}^{TT} are in the plane transverse to $\hat{\boldsymbol{n}}$. We can choose the z-axis to be along the direction of propagation $\hat{\boldsymbol{n}}$ without loss of generality. Then in the TT gauge we have

$$h_{ab}^{TT}(t,z) = \begin{pmatrix} h_+ & h_\times \\ h_\times & -h_+ \end{pmatrix}_{ab} \cos[\omega\,(t - z/c)]\,, \tag{2.30}$$

where $a, b = 1, 2$ and the h_+ and $h_\times$ are called the "plus" and "cross" polarization amplitudes of the gravitational wave. Recall that the $h_{0\mu}^{TT}$ and the $h_{\mu 0}^{TT}$ components vanish because of the gauge (2.29), while all the other components of the polarization tensor are 0 because of the choice of the z-axis.

Remember that, since General Relativity is invariant under diffeomorphisms, we should be able to go from some general solution $h_{kl}(x)$ only in the Lorentz gauge to the solution in the TT gauge. In oder to do so, we first introduce the symmetric and transverse projector tensor

$$P_{ij}(\hat{\boldsymbol{n}}) = \delta_{ij} - n_i n_j\,, \tag{2.31}$$

which has trace $P_{ii} = 2$. We can now construct another projector tensor which converts any rank 2 tensor to a tensor transverse along $\hat{\boldsymbol{n}}$ and traceless. This is done with the *Lambda tensor*

$$\Lambda_{ij,kl}(\hat{\boldsymbol{n}}) = P_{ik}P_{jl} - \frac{1}{2}P_{ij}P_{kl}\,. \tag{2.32}$$

If we now apply the Lambda tensor to some perturbation $h_{\mu\nu}$ in the Lorentz gauge, but not yet in the TT gauge, we get the gravitational wave projected to the TT gauge, with spatial components h_{ij} given by

$$h_{ij}^{TT} = \Lambda_{ij,kl}\, h_{kl}\,. \tag{2.33}$$

The plane wave solution (2.30) is very simple, and the reason is the good choice of the gauge, or physically speaking the proper choice of the reference frame. In the next section we will explain how this TT frame behaves and why also other frames will be important for interpretation and detection of GWs.

2.3 Interaction of GWs with test masses

In General Relativity, the mathematical procedure of choosing a gauge corresponds physically to selecting a specific reference frame. There are some interesting frames from which one can observe GWs, and each one of them has advantages and disadvantages, and a slightly different physical meaning, to understand which it is sometimes useful to write explicitly the geodesic equation and the equation of geodesic deviation. In this section we shall analyze four important frames: local inertial frames and freely falling frames, the TT frame and the proper detector frame.

Local inertial frames

According to the equivalence principle of General Relativity, it can be shown that it is always possible to change the coordinates in such a way that all the components of the Christoffel symbol vanish at some point P on the spacetime manifold: $\Gamma^{\mu}_{\nu\rho}(P) = 0$. The geodesic equation (2.9) at this point in the local inertial frame obviously reads

$$\left.\frac{\mathrm{d}^2 x^\mu}{\mathrm{d}\tau^2}\right|_P = 0\,, \tag{2.34}$$

which means that in this reference frame a test mass is free falling, but only at one specific point P in spacetime. From this point one can send out geodesics in every direction and reach – at least in a sufficiently small region of the manifold, where geodesics do not intersect – every point in spacetime. Hence, one can build an unambiguous coordinate system, which we usually call *Riemann normal coordinates*. In this frame, however, a test mass only moves freely at one point in spacetime.

Freely falling frames

An extension of the local inertial frame is a coordinate system where a test mass is in free fall all along the geodesic. An example of such a frame is a drag-free satellite, which is moving like a gyroscope and therefore freely spinning, marking the direction of the spatial axes. One can then build a local inertial frame centered on the point where the satellite is at a given time, and then propagate the reference frame along the geodesic on which the satellite moves, keeping the spatial axes oriented in the direction of the gyroscope. The coordinates generated in this way are called *Fermi normal coordinates*. It is straightforward to check that the Christoffel symbol vanishes in every point of the path, making the satellite being at free fall all along its geodesic

$$\left.\frac{\mathrm{d}^2 x^\mu}{\mathrm{d}\tau^2}\right|_{\gamma(\tau)} = 0 \,. \tag{2.35}$$

This reference frame is called *freely falling frame*, and it will be interesting for the description of space-borne GWs detectors, such as eLISA.

TT frame

We now come back to the TT frame, defined through the coordinate choice imposed by the TT gauge, studied in the previous section. The description of GWs in this frame turns out to be very simple, but what does that mean physically?
Let's write down again the geodesic equation, now for a test mass initially at rest:

$$\left.\frac{\mathrm{d}^2 x^i}{\mathrm{d}\tau^2}\right|_{\tau=0} = -\left[\Gamma^i_{\nu\rho}\frac{\mathrm{d}x^\nu}{\mathrm{d}\tau}\frac{\mathrm{d}x^\rho}{\mathrm{d}\tau}\right]_{\tau=0} = -\left[\Gamma^i_{00}\left(\frac{\mathrm{d}x^0}{\mathrm{d}\tau}\right)^2\right]_{\tau=0} , \tag{2.36}$$

where the derivatives of the spatial components vanish, being the test mass at rest at $\tau = 0$. The 00 component of the Christoffel symbol in linearized theory – given in (2.14) – reads thus

$$\Gamma^i_{00} = \frac{1}{2}(2\partial_0 h_{0i} - \partial_i h_{00}) \,. \tag{2.37}$$

However, this quantity vanishes because of the TT gauge conditions (2.29), since both h_{0i} and h_{00} are chosen to be 0. We have therefore a zero acceleration if the test mass is at rest at initial time, and the initial zero spatial velocity will vanish at all times. This means physically that in the TT frame, a particle initially at rest will not move even during the passage of a gravitational wave. The coordinates stretch themselves such that the position of these masses do not change. It would be then correct to take such test masses to mark the coordinates.

Let's consider further how the TT frame behaves by computing explicitly the equation of geodesic deviation (2.11) in this gauge. We write it for the three spatial components $i = 1, 2, 3$ and assume as before that at initial time $\tau = 0$ we have $\mathrm{d}x^0/\mathrm{d}\tau = c$, $\mathrm{d}x^i/\mathrm{d}\tau = 0$. Then we can write

$$\left.\frac{\mathrm{d}^2 \xi^i}{\mathrm{d}\tau^2}\right|_{\tau=0} = -\left[2c\Gamma^i_{0\rho}\frac{\mathrm{d}\xi^\rho}{\mathrm{d}\tau} + c^2\xi^\sigma\partial_\sigma\Gamma^i_{00}\right]_{\tau=0} . \tag{2.38}$$

In the TT gauge we have $\Gamma^i_{00} = 0$, $\Gamma^i_{0j} = (1/2)\partial_0 h_{ij}$. Thus, the second term on the right hand side vanishes, while the first is non-zero only for spatial components, i.e. for $\rho \neq 0$. That yields

$$\left.\frac{\mathrm{d}^2\xi^i}{\mathrm{d}\tau^2}\right|_{\tau=0} = -\left.\dot{h}_{ij}\frac{\mathrm{d}\xi^j}{\mathrm{d}\tau}\right|_{\tau=0} . \tag{2.39}$$

This shows clearly that the coordinate separation between two test masses on nearby geodesics stays constant at all times, even while a gravitational wave is passing, if it is initially constant. Notice, however, that ξ^i is a coordinate distance, not a physical distance. The fact that the coordinate distance between two test masses stays constant when a GW is traveling by, does not mean that there are no physical effects happening, and that gravitational waves could in principle be "gauged away". Using the TT frame one can merely state that it is possible to choose coordinates which stretch themselves following the stretching of the metric given e.g. by the passage of a gravitational wave, in order to maintain constant the coordinates of a test mass initially at rest. Physical effects must instead be investigated using proper distances. This can be done either through the invariant length element ds^2 or with another reference frame.

Proper detector frame

The last reference frame we consider is the most intuitive for an observer and is commonly used by physicists. Coordinates are fixed in a laboratory, and distances – instead of freely falling masses – are taken by an ideal rigid rule, measuring the motion of test masses in response to an incoming gravitational wave. We call it the *proper detector frame*.

In the TT frame we could describe the wave solution in a very simple way, since coordinates were moving along with the metric keeping distances between masses at rest the same at all times. Here, since coordinates are fixed, when the metric expands because of an incoming gravitational wave, test masses change their coordinate positions and therefore distances. This can be studied, again, using the equation of geodesic deviation (2.12). It can be shown (e.g. [26]) that in the proper detector frame, for spatial components, we get

$$\ddot{\xi}^i = \frac{1}{2}\ddot{h}^{TT}_{ij}\,\xi^j , \tag{2.40}$$

where the dots denote here time derivative with respect to the coordinate time of the proper detector frame. From this very simple result we can understand the geodesic displacement of a test mass m as the action of a Newtonian force given by

$$F^i = \frac{m}{2}\ddot{h}^{TT}_{ij}\,\xi^j , \tag{2.41}$$

that is why this frame looks very familiar to some physicist in a laboratory. The action of a gravitational wave on a detector or on a configuration of test masses can therefore be considered in terms of a Newtonian force in a flat spacetime manifold, without need to extend our considerations to General Relativity.

As an example, its action on a ring of test masses on the xy-plane at $z = 0$, with an amplitude set to zero at initial time $h^{TT}_{ij}\big|_{t=0} = 0$, for a "plus" polarized gravitational wave travelling along the z-axis, according to (2.30) is simply given by

$$h^{TT}_{ab} = h_+ \sin\omega t \begin{pmatrix} 1 & 0 \\ 0 & -1 \end{pmatrix}_{ab} , \tag{2.42}$$

recalling that all other components of the $h_{\mu\nu}$ tensor vanish. In an analogous way one can express the effect of a "cross" polarized wave or even of a wave with both components.

If we define $\delta x(t)$, $\delta y(t)$ as the small displacements from the main geodesic induced by the Newtonian force, with $\xi_a(t) = (x_0 + \delta x(t), y_0 + \delta y(t))$, and (x_0, y_0) as the unperturbed positions, then the equation of geodesic deviation in the proper detector frame implies that

$$\delta\ddot{x} = -\frac{h_+}{2}(x_0 + \delta x)\,\omega^2 \sin\omega t \ , \tag{2.43}$$

$$\delta\ddot{y} = +\frac{h_+}{2}(y_0 + \delta y)\,\omega^2 \sin\omega t \ . \tag{2.44}$$

Now, since we keep only linear order in h, we can drop the terms δx, δy, and easily integrate the equations and obtain

$$\delta x(t) = +\frac{h_+}{2} x_0 \sin\omega t \ , \tag{2.45}$$

$$\delta y(t) = -\frac{h_+}{2} y_0 \sin\omega t \ . \tag{2.46}$$

Similarly, one can perform these steps for the "cross" polarization and get

$$\delta x(t) = \frac{h_\times}{2} y_0 \sin\omega t \ , \tag{2.47}$$

$$\delta y(t) = \frac{h_\times}{2} x_0 \sin\omega t \ . \tag{2.48}$$

The resulting deformation of a ring of test masses induced by an incoming "plus" and "cross" polarized gravitational wave is represented in Figure 2.1.

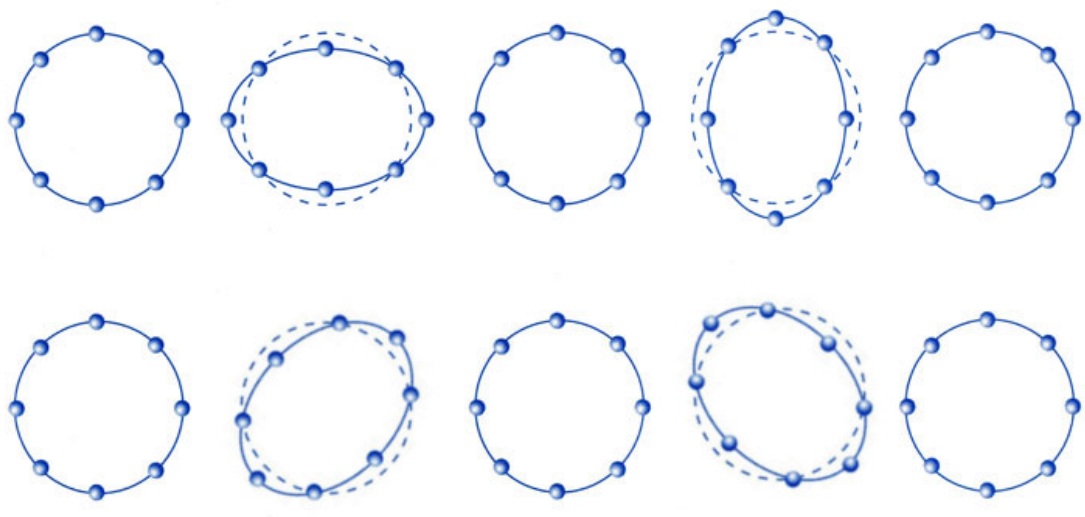

Figure 2.1: The action of a gravitational wave passing through a ring of test masses. The traveling direction is intended to be through the paper. In the above picture we display the action of the "plus" polarization, while on the bottom we show the "cross" polarization. The amplitude of the effect is here $\sim 10^{20}$ times bigger than the usual scale. The credits for this picture go to L.C. Epstein [28]

Chapter 3

Shaping waveforms and hunting black holes

"Scientific progress is the discovery of a more and more comprehensive simplicity... The previous successes give us confidence in the future of science: we become more and more conscious of the fact that the universe is cognizable."

G. E. Lemaître

Our interest towards gravitational waves and our excitement about their possible detection within the next few years is mainly due to the fact that we would be able to directly observe the sources of these perturbations, as well as their configuration and physical behaviour.

So far, in the previous Chapter, we discussed how we can describe the nature of a gravitational wave breaking the covariance of General Relativity and linearizing the field equations, and studied how such a wave propagates through a flat spacetime background and acts on test masses, while looking at the perturbation in a region far away from the source, where many approximations can be used.
Now we will consider the process of generation of gravitational waves. This study is of capital importance. Indeed, from the noisy and loud detector signal, one has to extract the tiny gravitational waves hidden in it, and eventually infer the responsible source, through a process which is usually referred to as *data analysis* and *parameter estimation*. Understanding how a source generates gravitational waves allows us therefore to point out which system is responsible for an eventual GW detection. This is where gravitational wave astronomy arises.

In the next section we will devote our attention to a standard source of gravitational waves: a black hole binary on an approximated circular orbit. Afterwards, we will discuss how a wave interacts with an ideal detector, and we briefly review some of the currently running and planned detectors.

3.1 Generation of gravitational waves

3.1.1 Weak-field and low-velocity approximation

In the previous Chapter we derived the linearized Einstein's field equations (2.26) in the Lorentz gauge

$$\Box \bar{h}_{\mu\nu} = -\frac{16\pi G}{c^4} T_{\mu\nu} . \tag{3.1}$$

This equation is by definition linear in $h_{\mu\nu}$ and can be solved in the same way as in electromagnetism. We define the Green's function $G(x-x')$ through the equation

$$\Box_x G(x-x') = \delta^4(x-x') , \tag{3.2}$$

and we write its solution for our boundary conditions through the retarded time

$$t_{\text{ret}} = t - \frac{|\boldsymbol{x}-\boldsymbol{x'}|}{c} , \tag{3.3}$$

and with $x'^0 = ct'$, $x^0_{\text{ret}} = ct_{\text{ret}}$, which takes the form of the *retarded Green's function*

$$G(x-x') = -\frac{1}{4\pi|\boldsymbol{x}-\boldsymbol{x'}|}\delta(x^0_{\text{ret}} - x'^0) , \tag{3.4}$$

In an analogous way as in electromagnetism (see e.g. [25]), the solution to (3.1) in terms of the retarded Green's function is given by

$$\bar{h}_{\mu\nu}(x) = -\frac{16\pi G}{c^4}\int d^4x'\, G(x-x')T_{\mu\nu}(x') . \tag{3.5}$$

Plugging (3.4) into (3.5) gives finally

$$\bar{h}_{\mu\nu}(t,\boldsymbol{x}) = \frac{4G}{c^4}\int d^3x' \frac{1}{|\boldsymbol{x}-\boldsymbol{x'}|} T_{\mu\nu}\left(t - \frac{|\boldsymbol{x}-\boldsymbol{x'}|}{c}, \boldsymbol{x'}\right) . \tag{3.6}$$

Here we can apply the TT gauge, choosing the coordinate origin to be at the center of mass of the source and the observer to be at the position pointed by the vector $\boldsymbol{x}$, and requiring that the observer is well outside the source. Through (2.33) we can write

$$h^{TT}_{ij}(t,\boldsymbol{x}) = \frac{4G}{c^4}\Lambda_{ij,kl}(\hat{\boldsymbol{n}})\int d^3x' \frac{1}{|\boldsymbol{x}-\boldsymbol{x'}|} T_{kl}\left(t - \frac{|\boldsymbol{x}-\boldsymbol{x'}|}{c}, \boldsymbol{x'}\right) , \tag{3.7}$$

where $\hat{\boldsymbol{n}} = \boldsymbol{x}/r$ and $r = |\boldsymbol{x}|$. Now, if we denote by d the typical size of the source, in the approximation $d \ll r$ we can perform the expansion

$$|\boldsymbol{x}-\boldsymbol{x'}| = r - \boldsymbol{x'}\cdot\,\hat{\boldsymbol{n}} + \mathcal{O}\left(\frac{d^2}{r}\right) . \tag{3.8}$$

Taking the limit $r \to \infty$, i.e. considering the observer far away from the source, we rewrite (3.7) at leading order, where $|\boldsymbol{x}-\boldsymbol{x'}| = r$, and obtain

$$h^{TT}_{ij}(t,\boldsymbol{x}) = \frac{4G}{c^4 r}\Lambda_{ij,kl}(\hat{\boldsymbol{n}})\int d^3x'\, T_{kl}\left(t - \frac{r}{c} + \frac{\boldsymbol{x'}\cdot\,\hat{\boldsymbol{n}}}{c}, \boldsymbol{x'}\right) . \tag{3.9}$$

At this point we consider the fact that the equations simplify significantly if we perform the low velocity expansion. This approximation can be made, since we expect that velocities inside the source are much smaller than the speed of light, i.e. $v/c \ll 1$. In terms of the typical angular frequency ω of the motion inside the source – proportional to v/d – or in terms of the reduced wavelength $\lambda = c/\omega$, this means that $\lambda = \frac{c}{v}d$. Therefore for non relativistic sources the wavelength of a gravitational wave is much larger than its typical size:

$$\lambda \gg d \ . \tag{3.10}$$

In this case, one can perform an expansion in v/c of the energy-momentum tensor in (3.9), as it is done e.g. in [26], and obtain

$$T_{kl}\left(t_{\rm ret} + \frac{\boldsymbol{x'}\cdot\hat{\boldsymbol{n}}}{c}, \boldsymbol{x'}\right) = T_{kl} + \frac{x'^i n^i}{c}\partial_0 T_{kl} + \frac{1}{2c^2}x'^i x'^j n^i n^j \partial_0^2 T_{kl} + \dots \ , \tag{3.11}$$

where all the T_{kl} and their derivatives are evaluated at the retarded point $(t_{\rm ret}, \boldsymbol{x'})$, in the weak field limit where $t_{\rm ret} = t - \frac{r}{c}$. To simplify further the equations, we introduce here important quantities we will use also in later Chapters: the *momenta of the energy-momentum tensor* T^{ij}

$$S^{ij} = \int d^3x \ T^{ij}(t,\boldsymbol{x}) \ , \tag{3.12}$$

$$S^{ij,k} = \int d^3x \ T^{ij}(t,\boldsymbol{x}) \ x^k \ , \tag{3.13}$$

$$S^{ij,kl} = \int d^3x \ T^{ij}(t,\boldsymbol{x}) \ x^k x^l \ , \tag{3.14}$$

$$S^{ij,kl\dots n} = \int d^3x \ T^{ij}(t,\boldsymbol{x}) \ x^k x^l \dots \ x^n \ , \tag{3.15}$$

and the *momenta of the energy density* T^{00}/c^2, also called the *mass momenta*

$$M = \frac{1}{c^2}\int d^3x \ T^{00}(t,\boldsymbol{x}) \ , \tag{3.16}$$

$$M^i = \frac{1}{c^2}\int d^3x \ T^{00}(t,\boldsymbol{x}) \ x^i, \tag{3.17}$$

$$M^{ij} = \frac{1}{c^2}\int d^3x \ T^{00}(t,\boldsymbol{x}) \ x^i x^j, \tag{3.18}$$

$$M^{ijk} = \frac{1}{c^2}\int d^3x \ T^{00}(t,\boldsymbol{x}) \ x^i x^j x^k, \tag{3.19}$$

$$M^{ijk\dots n} = \frac{1}{c^2}\int d^3x \ T^{00}(t,\boldsymbol{x}) \ x^i x^j x^k \dots \ x^n, \tag{3.20}$$

If we now use these definitions and put the low velocity expansion (3.11) into (3.9), we obtain

$$h_{ij}^{TT}(t,\boldsymbol{x}) = \frac{4G}{c^4 r}\Lambda_{ij,kl}(\hat{\boldsymbol{n}})\left[S^{kl} + \frac{1}{c}n_m \dot{S}^{kl,m} + \frac{1}{2c^2}n_m n_p \ddot{S}^{kl,mp} + \dots\right]_{\rm ret} \ , \tag{3.21}$$

where we again write "ret" because the momenta and their derivatives are evaluated at retarded time $t_{\rm ret}$. This equation is usually called the *multipole expansion*, and can be extended

up to arbitrary order while taking into account higher terms in (3.11). Here and in the next two Chapters we will focus on the leading order, the so-called *quadrupolar radiation*, where we neglect terms in $(1/c)$ and higher. In Chapter 6 we will consider higher order terms and make some considerations regarding a systematic multipole expansion.

We notice at this point some interesting facts about these quantities. It is straightforward to see that M is conserved

$$\dot{M} = c\partial_0 M = \frac{1}{c}\int d^3x\ \partial_0 T^{00} = -\frac{1}{c}\int d^3x\ \partial_i T^{0i} = 0\ , \tag{3.22}$$

since $\partial_\nu T^{\mu\nu} = 0$ and $T^{\mu\nu}$ vanishes on the boundary of the region, because we are integrating over a volume larger than the source. Moreover, the linear momentum $\dot{M}^i$ is also conserved, since $\ddot{M}^i = 0$, while the angular momentum $\dot{M}^{ij}$ has a derivative which corresponds to twice the first moment of the energy-momentum tensor: recalling that $\partial_t = c\partial_0$ we can write

$$\ddot{M}^{ij} = \partial_0^2 \int d^3x\ T^{00}\ x^i x^j = \int d^3x\ (\partial_k\partial_l T^{kl})\ x^i x^j = \int d^3x\ 2T^{ij} = 2\,S^{ij}\ . \tag{3.23}$$

This will turn out to be a crucial quantity while computing gravitational radiation. Indeed, the first two mass momenta cannot contribute to gravitational wave emission, since they are conserved. The leading order radiation is instead given by the quadrupole moment, and we can then write the expansion (3.21) as

$$h_{ij}^{TT}(t,\boldsymbol{x}) = \frac{2G}{c^4 r}\,\Lambda_{ij,kl}(\hat{\boldsymbol{n}})\,\ddot{M}^{kl}(t_{\rm ret}) = \frac{2G}{c^4 r}\,\ddot{M}_{ij}^{TT}(t_{\rm ret})\ . \tag{3.24}$$

Imposing $\hat{\boldsymbol{z}}$ as the propagation direction of the gravitational wave, as done previously, without loss of generality, we can compute the components of the quadrupole moment $\ddot{M}^{kl}$ projected on the transverse-traceless gauge using the Lambda tensor, i.e. $\ddot{M}_{ij}^{TT} = \Lambda_{ij,kl}\ddot{M}^{kl}$. We get

$$\ddot{M}_{ij}^{TT} = \Lambda_{ij,kl}(\hat{\boldsymbol{z}})\,\ddot{M}^{kl} = \begin{pmatrix} (\ddot{M}_{11}-\ddot{M}_{22})/2 & \ddot{M}_{12} & 0 \\ \ddot{M}_{21} & -(\ddot{M}_{11}-\ddot{M}_{22})/2 & 0 \\ 0 & 0 & 0 \end{pmatrix}_{ij}\ . \tag{3.25}$$

The "plus" and "cross" polarizations of a gravitational wave traveling in the z direction in the quadrupolar approximation – which we defined in (2.30) – can be directly read from this result

$$h_+ = \frac{1}{r}\frac{G}{c^4}\,(\ddot{M}_{11}-\ddot{M}_{22})\ , \tag{3.26}$$

$$h_\times = \frac{2}{r}\frac{G}{c^4}\,\ddot{M}_{12}\ , \tag{3.27}$$

where again the quantities are evaluated at the retarded time $t_{\rm ret} = t - r/c$. This result can be extended to generic propagation directions $\hat{\boldsymbol{n}}$. Let's introduce the spherical coordinates (ϕ,θ) so that

$$\hat{\boldsymbol{n}} = (\sin\theta\sin\phi, \sin\theta\cos\phi, \cos\theta)\ . \tag{3.28}$$

Then, using the standard tools of geometry, one can transform the previous quantities through the rotation matrices and obtain the general result

$$h_+(t;\phi,\theta) = \frac{1}{r}\frac{G}{c^4}\Big[\,\ddot{M}_{11}(\cos^2\phi - \sin^2\phi\cos^2\theta) + \ddot{M}_{22}(\sin^2\phi - \cos^2\phi\cos^2\theta) - \ddot{M}_{33}\sin^2\theta - \ddot{M}_{12}\sin 2\phi(1+\cos^2\theta) + \ddot{M}_{13}\sin\phi\sin 2\theta + \ddot{M}_{23}\cos\phi\sin 2\theta\Big]\,, \tag{3.29}$$

$$h_\times(t;\phi,\theta) = \frac{1}{r}\frac{G}{c^4}\Big[\,(\ddot{M}_{11} - \ddot{M}_{22})\sin 2\phi\cos\theta + 2\ddot{M}_{12}\cos 2\phi\cos\theta - 2\ddot{M}_{13}\cos\phi\sin\theta + 2\ddot{M}_{23}\sin\phi\sin\theta\Big]\,. \tag{3.30}$$

This final result is very important, since it reduces the whole task of computing gravitational waveforms to the problem of solving the underlying dynamics of the source and evaluating the resulting quadrupole moment. As we will study in Chapters 5, 6 and 7, the very simple result in (3.29)-(3.30), the leading order, needs to be extended to higher order corrections to be precise enough for an eventual parameter estimation with detectors data. For sources in a strong-field regime, e.g. self-gravitating systems such as inspirals of black hole binaries, a combination of a higher multipole expansion and a very accurate description of the dynamics will be required, especially while considering spin-orbit couplings, the effects of radiation reaction, spin-spin corrections, and so on. For the moment being, we restrict our study to the leading quadrupole order and, as an example, we analyze in the next section a standard problem in GW theory: the case of a compact binary on a circular orbit.

3.1.2 GWs from a circular black hole binary

The quadrupole radiation from a two-body system on a circular orbit is a very basic example of how waveforms are computed by solving the dynamics of the emitting source and using the results from linearized theory we have studied so far. In Chapter 5 and 7 we show how to develop a prescription that allows us to generate more sophisticated waveforms arising from complex systems. In particular, the presence of spins, eccentricity and radiation reaction make things more difficult and require a very accurate approach. However, this introductory example aims to illustrate briefly and in a compact way how this process has to be carried out.

We consider a binary system where the compact bodies – e.g. black holes or neutron stars – have masses m_1 and m_2. Let's assume that the motion occurs on a plane along a circular orbit, neglecting any precession of the orbital plane due to spin effects or any variation of the circular motion due to energy loss of the system through gravitational wave emission. Choosing the motion to happen on the (x,y)-plane, the trajectory of the relative motion can be parametrized as

$$x(t) = R\cos(\omega_s t)\,, \quad y(t) = R\sin(\omega_s t)\,, \quad z(t) = 0\,. \tag{3.31}$$

In the center–of–mass frame the second mass moment is $M^{ij} = \mu x^i x^j$, where $\mu = m_1 m_2/m$ is the reduced mass and m the total mass of the binary. Explicitly

$$M_{11} = \mu R^2\cos^2(\omega_s t)\,, \tag{3.32}$$

$$M_{22} = \mu R^2\sin^2(\omega_s t)\,, \tag{3.33}$$

$$M_{12} = \mu R^2\frac{1}{2}\sin(2\omega_s t)\,. \tag{3.34}$$

All the other components of M^{ij} vanish since they contain terms in $z(t)$. The second derivatives of the quadrupole moments are

$$\ddot{M}_{11} = -\,2\mu R^2\omega_s^2\ \cos(2\omega_s t)\ , \tag{3.35}$$
$$\ddot{M}_{22} = +\,2\mu R^2\omega_s^2\ \cos(2\omega_s t)\ , \tag{3.36}$$
$$\ddot{M}_{12} = -\,2\mu R^2\omega_s^2\ \sin(2\omega_s t)\ . \tag{3.37}$$

From the previous section, we know that at leading order the polarization states of the gravitational wave are given by (3.29)-(3.30). Plugging into them the above quantities we obtain

$$h_+(t) = \frac{4G\mu\omega_s^2R^2}{c^4r}\left(\frac{1+\cos^2\theta}{2}\right)\cos(2\omega_s t)\ , \tag{3.38}$$
$$h_\times(t) = \frac{4G\mu\omega_s^2R^2}{c^4r}\cos\theta\ \sin(2\omega_s t)\ , \tag{3.39}$$

where the dependence on ϕ can be absorbed in ωt since for a circular orbit ϕ would only enter the periodic function sin and cos and is therefore just equivalent to a time translation. We notice here some interesting facts. The most important is the frequency of the gravitational wave, which at quadrupolar order turns out to be *twice the frequency of the source*:

$$\omega_{GW} = 2\omega_s\ . \tag{3.40}$$

Another interesting result we obtain is the dependence on the orientation angle θ of the radiation. If the observer sees the source edge-on, i.e. with an angle $\theta = \pi/2$, then the $h_\times$ component vanishes and the wave is only linearly polarized, which results in a loss of information. On the other hand, if the observer sees the source face-on, with an inclination $\theta = 0$, both polarizations have the same amplitude. In this case, since h_+ depends on $\cos(\omega_{GW}t)$ and $h_\times$ depends on $\sin(\omega_{GW}t)$, the gravitational wave is circularly polarized.

In this simple example, the amplitude of the wave as well as the frequency remain constant all along the interaction, which is assumed to last infinitely long. However, in the real case of an inspiral binary the radiated gravitational waves carry energy away from the system, resulting also in a loss of angular momentum, in a decreasing period and increasing frequency of the wave. Since the two masses approach each other and the interaction gets stronger, also the amplitude of the wave will increase. At this point, many of the assumptions we have been using so far cannot be made anymore. In fact, for actual detection we are interested in the strong field regime of General Relativity, where linearized equations are no longer valid, and have to be extended to higher orders. At first order we could use a Newtonian description of the dynamics of a self-gravitating system, and therefore the virial theorem, according to which

$$\frac{1}{2}\frac{G\mu M}{r} = \frac{1}{2}\mu v^2\ . \tag{3.41}$$

In terms of the Schwarzschild radius $r_S = 2GM/c^2$ we could then write

$$r_S/d \sim (v/c)^2\ . \tag{3.42}$$

The extension of linearized theory we need in the strong field regime is then given by an expansion in $r_S/d \sim (v/c)^2$ and is usually called the *post-Newtonian expansion*. This expansions bases on the assumption that velocities inside the source are smaller than the speed of light

c. As the circular binary starts emitting enough energy through gravitational waves, radiation reaction cannot be neglected anymore, energy loss increases the frequency and thus velocities of the binary. Hence, higher order terms in $(v/c)^2$ start getting more and more important. At late phases of the inspiral, just before merger of the binary companions, post-Newtonian formalism plays therefore a key role while shaping accurate waveforms. For a detailed treatment of this subject, see also the Living Review on gravitational radiation from post-Newtonian sources and inspiralling compact binaries by Luc Blanchet [29].

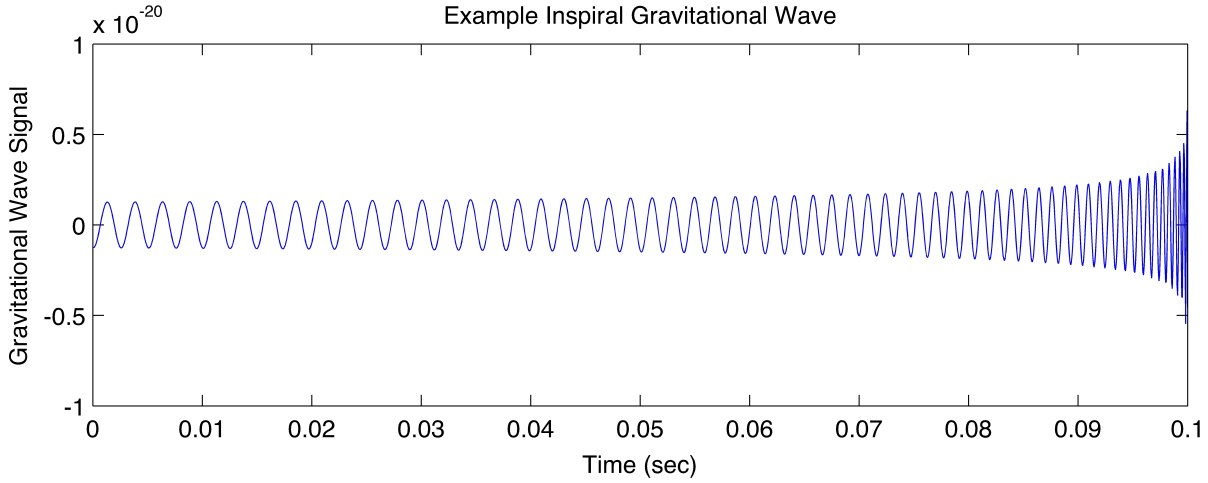

Figure 3.1: An example of a gravitational waveform. In the first part, the binary is moving along a quasi-circular orbit. The loss of energy through gravitational waves is negligible, and one can use results from linearized theory to describe the waveform, such as our Equations (3.38) and (3.39). As soon as the system starts loosing enough energy, a post-Newtonian expansion to higher order in $(v/c)^2$ is required. This is the second part of the plot: the inspiral phase of the binary, which eventually leads to a merger of the two compact bodies, while the frequency, the amplitude and therefore the energy carried away by the gravitational wave increase more and more. Just before the merger and the following ring-down has begun, post-Newtonian theory can no longer be applied and one may finds other prescriptions for generating waveforms, such as Effective One Body formalism or Numerical Relativity. Credits for this illustration go to A. Stuver, for the LIGO collaboration [24, 30].

3.2 Interaction of gravitational waves with a detector

One of the simplest gravitational wave detectors we can imagine is a Michelson-type interferometer. In 1887 Albert A. Michelson and Edward W. Morley performed an experiment in an attempt to detect the relative motion of matter through the stationary "aether". They tried to compare the speed of light along different perpendicular directions. The experimental setting was rather simple, consisting of a source of coherent light, which was split into two separate beams in equally long arms. Light was then reflected back through the arm with a mirror and recombined into a photoreceptor measuring an interference light pattern. Such a system, developed a few years before the cited experiment by Michelson, is usually called *interferometer*.

While the Michelson-Morley experiment can be considered as one of the most famous "failed" experiments – since the presence of aether was not detected and no differences in the speed of light were measured, eventually leading to the theory of Special Relativity – its experimental settings can be very useful for gravitational waves detection.
All current detection attempts rely indeed on the ability of measuring the perturbation of the metric through the change of length of the arms of a sufficiently big interferometer.

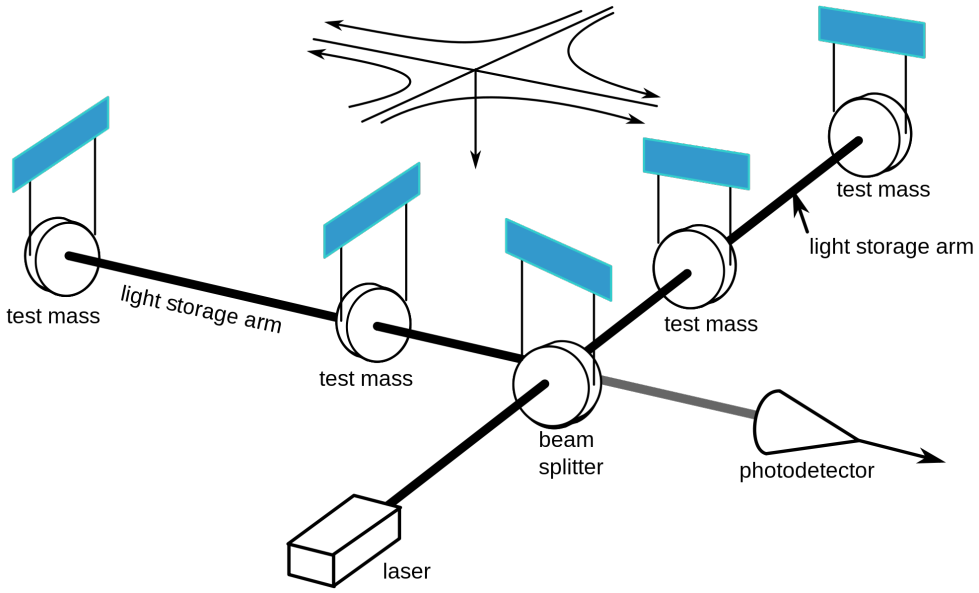

Figure 3.2: An example of an interferometric gravitational wave detector. A laser source emits coherent light, which passes through a beam splitter and is sent into the two equally long detector arms. Light is mirrored forth and back many times, increasing the precision of the interferometer without need of too long arms. Once the photons from both arms recombine reaching the photoreceptor, an interference pattern appears as a result. The imprint of a wave passing through the detector plane is left on this interference pattern, from which one can extract the amplitude and the frequency evolution of the gravitational wave and thus of its source. Picture credits: the LIGO collaboration [24, 30].

Test masses – usually mirrors – are placed at each end of the arms, such that they are at rest and in free fall at least with respect to some degrees of freedom. Recall that in the TT frame, a mass initially at rest stays at rest even during the passage of a gravitational wave, i.e. the coordinates are constant, as we computed in Chapter 2. Physical distances however, expressed through the gauge-invariant length element ds, shrink and stretch in response to the passage of a wave. It is then possible to measure the effect of an incoming wave by looking at how the metric varies. Figure 3.2 illustrates schematically how such an interferometer looks like.

Let's suppose that the arms of the detector are placed along the x and y axes, respectively, while the gravitational wave is travelling in the z direction and passing through the plane of the interferometer. For simplicity, let's also assume that the wave is purely linearly polarized. Setting the origin of the coordinate system at the beam splitter, the position of the mirrors is given by $(L,0,0)$ and $(0,L,0)$. Following the result in (2.30), the metric is given by

$$ds^2 = -c^2dt^2 + [1+h_+(t)]\,dx^2 + [1-h_+(t)]\,dy^2 + dz^2\,, \tag{3.43}$$

where $h_+(t) = h_+ \cos[\omega(t - z/c)]$. Light always follows null geodesics, where $ds^2 = 0$. Hence, for a photon travelling along the x arm of the interferometer we can write

$$dx = \pm\, c\; dt\; [1 + h_+(t)]^{-1/2} = \pm\, c\; dt \left[1 - \frac{1}{2} h_+(t)\right] + \mathcal{O}(h_+^2)\,, \tag{3.44}$$

where the signs depends on the direction of the light beam. Consider now the path of the photon from the beam splitter, at time t_0, to the mirror, at time $t_{1,x}$. We can write

$$\begin{aligned} L_x &= \int_{ct_0}^{ct_{1,x}} dx = \int_{t_0}^{t_{1,x}} c\; dt \left[1 - \frac{1}{2} h_+(t)\right] \\ &= c(t_{1,x} - t_0) - c\frac{h_+}{2\omega}[\sin(\omega t_{1,x}) - \sin(\omega t_0)]\,. \end{aligned} \tag{3.45}$$

Similarly, from the mirror to the photodetector, at time $t_{2,x}$, we can integrate

$$\begin{aligned} -L_x &= \int_{ct_{1,x}}^{ct_{2,x}} dx = \int_{t_{1,x}}^{t_{2,x}} -c\; dt \left[1 - \frac{1}{2} h_+(t)\right] \\ &= -c(t_{2,x} - t_{1,x}) + c\frac{h_+}{2\omega}[\sin(\omega t_{2,x}) - \sin(\omega t_{1,x})]\,. \end{aligned} \tag{3.46}$$

Combining the last two equations we can write

$$t_{2,x} - t_0 = \frac{2L_x}{c} + \frac{h_+}{2\omega}[\sin(\omega t_{2,x}) - \sin(\omega t_0)]\,. \tag{3.47}$$

The same can be done for the light beam travelling in the y arm, where $dy = \pm\, c\; dt\; [1 - h_+(t)]$. One gets

$$t_{2,y} - t_0 = \frac{2L_y}{c} - \frac{h_+}{2\omega}[\sin(\omega t_{2,y}) - \sin(\omega t_0)]\,. \tag{3.48}$$

Since we are in the TT frame, the coordinates of the mirrors stays constant and we can write $L_x = L_y = L$ at any time. For the arrival time difference $\Delta t = t_{2,x} - t_{2,y}$ we get therefore

$$\Delta t = \frac{h_+}{\omega}\; [\sin(\omega(t_0 + 2L/c)) - \sin(\omega t_0)]\;, \tag{3.49}$$

where we replaced $t_{2,x}$ and $t_{2,y}$ through $t_0 + 2L/c$ in the sin terms, which holds at first order. This difference in the arrival time of the two light beams is the origin of the interference pattern in the detector, through which we are thus able to reconstruct the amplitude and the frequency of the signal through the interaction time. Notice that a similar calculation could be done in the proper detector frame, in which case the coordinates of the mirrors $(L_x, 0, 0)$ and $(0, L_y, 0)$ would vary in time. Nevertheless, the length element – being invariant – would yield the same result for the arrival time difference. In the literature the arrival time difference is usually expressed in terms of the differential length change of the arms, which for our case would read

$$\frac{\Delta L(t)}{L} = h_+(t)\,. \tag{3.50}$$

Generalizing these results for arbitrary coordinates of the detector, arbitrary propagation direction and polarization of the gravitational wave, and for arbitrary opening angle between the arms of the detector, the wave signal we observe in the interferometer can be written as

$$h(t) = F_+(\theta, \phi, \psi)\; h_+(t) + F_\times(\theta, \phi, \psi)\; h_\times(t)\,, \tag{3.51}$$

where the angular functions F_+ and $F_\times$ are called *antenna pattern functions* and describe the response of the detector to an incoming wave with spherical coordinates (θ, ϕ) and ψ depends on the polarization of the wave.

3.2.1 Towards detection of gravitational waves

At the time of writing (2015) a new era of gravitational wave astronomy is about to start. After a century of discovery and study of General Relativity and its wave solutions, a century of planning, building, improving and upgrading detectors, we are finally about to directly see gravitational waves and observe the universe with a tool different from electromagnetic waves.

First detections of gravitational waves are expected to happen within the next three years, and are most likely to occur through ground-based laser interferometers. The technical details and the instrumental specifications go beyond the scope of this work, and we encourage the interested reader to stay update though the official channels [24]. In this section we just give a brief qualitative summary of the current state of the art.

Ground-based detectors

The most promising detector for direct discovery of gravitational waves is the Laser Interferometer Gravitational Waves Observer (LIGO) collaboration [30]. It consists of two ground-based laser interferometers, as those we sketched above, with 4 km long arms. The two independent but correlated detectors are placed distant from each other in order to measure uncorrelated background noise and be therefore much more sensitive than a single interferometer. Both are placed in the US, one of them in Hanford (Washington State) and one in Livingston (Louisiana). Initial LIGO detectors were thought to be able to observe in the frequency range of about 40 Hz to 1000 Hz, with the hope of detecting a few nearby compact binary inspirals. The distance range the detector could achieve was about 20 Mpc. The upgraded detector started the first observation run in the last weeks and aims to resolve systems up to 1000 Mpc in the case of black hole binaries – which means and increase of more than 1000 times in volume! – covering a frequency range between about 10 Hz to a few kHz. Once the upgraded advanced LIGO will be operating at full capacity, some hundred detections per year are expected to happen, not only for compact binary inspirals but also pulsars emitting waves with a strain amplitude of less than 10^{-22}.

Space-based detectors

While it is true that advanced LIGO is very likely to be the first interferometer to detect gravitational waves, ground-based detectors will only be the first step towards gravitational wave astronomy. Planned space-based detectors will be able to listen to waves in other frequency ranges, and in a very accurate way, being free from many of the background noises we have on Earth.

The best proposed space-based detector so far is the evolved Laser Interferometer Space Antenna (eLISA) [31], a follow-up of the previously proposed LISA mission. The detector consists of three satellites at a distance of 1 million km orbiting around the sun a few tens of degrees behind the Earth. In Figure 3.3 we show a schematic picture of the eLISA configuration. The frequency range will be between 3×10^{-5} Hz and 1 Hz, meaning that we would be able to observe massive black hole mergers, with an expected rate of about 10 to 100 events per year, as well as a few tens of extreme mass ratio inspirals per year. Moreover, we believe that with such a powerful instrument we should be able to resolve around 3000 galactic binaries out of 30×10^6 in the eLISA band.

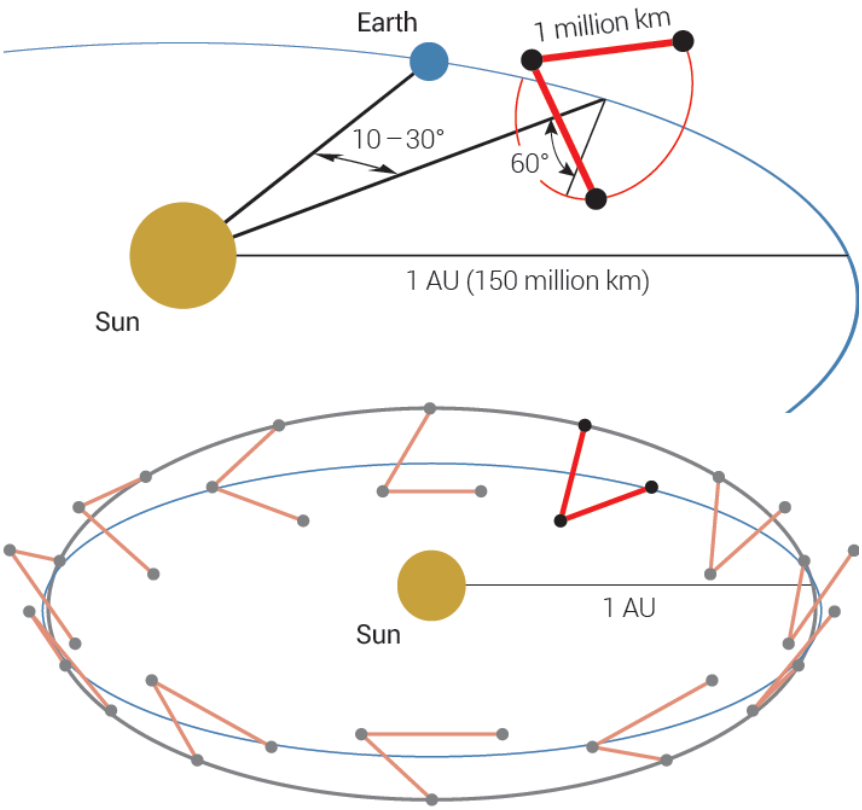

Figure 3.3: The configuration of the proposed eLISA mission. Three freely falling test masses in a triangle shape are orbiting around the Sun behind the Earth. A laser beam is sent from the central satellite to the two other test masses and mirrored back, generating an interference pattern in the detector. The arm length is likely to be 1 million km, but ongoing discussions might end in a 5 million km long arm configuration. The extreme size of the eLISA detector allows very accurate measurements of low frequency sources, especially in the millihertz regime, such as massive black hole binaries or extreme mass ratio inspiral, while the absence of noise caused by motions on Earth will allow a very high sensitivity, up to a characteristic strain of about 10^{-22}. Picture credits: eLISA collaboration [31].

It is obvious that eLISA will be a truly impressive instrument for gravitational wave astronomy, and its achievements could be really spectacular. The launch date is currently set to be in 2034. As we can see in Figure 3.4 the eLISA and LIGO band do not intersect. Both types of detectors can therefore be very important for gravitational wave astronomy, being complementary and aiming to detect different classes of sources.

In the same plot, we also display the sensitivity curve of the International Pulsar Time Array (PTA) [32], consisting in a survey of a set of pulsars emitting pulses with a very precise period and being therefore high precision clocks allowing measurements of variation of the metric between them and the Earth. Since the arm length of this kind of detection is given by the distance of the pulsar itself from the Earth, the range in which PTA is sensitive is at very low frequencies, at about $10^{-9} - 10^{-6}$ Hz [33]. We expect to be able to detect supermassive black hole binaries within the next decade, especially through a common effort aiming to correlate measurements of different surveys.

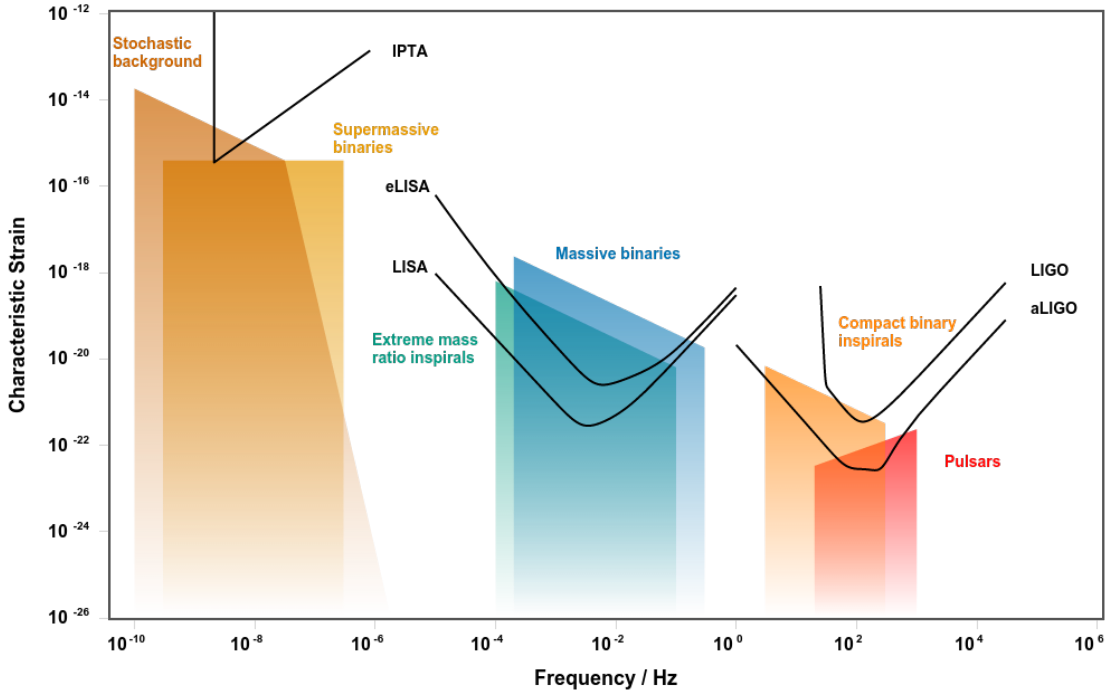

Figure 3.4: The sensitivity curve of ground and space-based detectors, as well as for PTA. As we can see, each detector type is mostly sensitive in a different frequency band. Advanced LIGO, in the Hz – kHz range, will mainly detect inspiralling compact binaries, as well as rapidly rotating, spherically asymmetric pulsars. eLISA instead will be sensitive to massive compact binaries, and has already more than 10 verification binaries, i.e. known systems emitting gravitational waves in the eLISA band, which we should be able to detect since the very beginning of the measurements. Pulsar Timing Arrays will finally be sensitive to sources emitting at very low frequencies, such as supermassive black hole binaries. Future generation detectors might cover better the whole frequency spectrum and hopefully reach strain sensitivities even lower than the already incredible 10^{-22}. The plot was generated with an online tool developed by Christopher Moore, Robert Cole and Christopher Berry [34].

After having seen in Chapter 2 how gravitational waves arise from linearization of General Relativity and how they behave and propagate, we studied at the beginning of this Chapter how gravitational waves are generated inside the source, and under which assumptions prescriptions for computing accurate waveforms can be developed. Also, we have seen how current detectors work and are built. Detection of gravitational waves is indeed a matter of both the construction of appropriate measurement instruments and of the precise knowledge of the waveform itself. Without an accurate waveform database, in fact, it would be very unlikely to extract a signal from the noisy detector output. Previous knowledge of what we expect to measure is therefore an inevitable requirement for gravitational wave astronomy.

In the next Chapters we devote our attention to this theoretical task, studying in particular how waveforms from hyperbolic and eccentric binaries can be generated within the post-Newtonian framework.

Chapter 4

Gravitational wave energy spectrum of hyperbolic encounters

L. De Vittori, Ph. Jetzer, A. Klein

Published in Physical Review D, Volume ***86****, 044017 (2012)* [1]

Abstract

The emission of gravitational waves is studied for a system of massive objects interacting on hyperbolic orbits within the quadrupole approximation following the work of Capozziello et al. [35]. Here we focus on the derivation of an analytic formula for the energy spectrum of the emitted waves. We checked numerically that our formula is in agreement with the two limiting cases for which results were already available: for the eccentricity $e = 1$, the parabolic case whose spectrum was computed by Berry and Gair [36], and the large e limit with the formula given by Turner [37].

4.1 Introduction

Einstein predicted already in 1916 that accelerated masses should emit gravitational waves. The detection of such kind of waves would open a new window in the exploration of our universe. In the last years technology has improved very rapidly, and it is now believed that the precision we reached should enable the direct detection of gravitational waves in few years, both with ground based and space based detectors such as e.g. the proposed eLISA mission. It is, therefore, interesting to study the dynamics of typical systems and their emission of gravitational waves and in particular their frequency spectrum, in order to know at which wave-length range we should expect gravitational radiation.

For the cases of binary systems or spinning black holes on circular and elliptical orbits the resulting energy spectra have already been well studied [38, 39]. The energy spectrum for

parabolic encounters has been computed either by direct integration along unbound orbits [37] or more recently by taking the limit of the Peters and Mathews energy spectrum for eccentric Keplerian binaries [36].
The emission of gravitational waves from a system of massive objects interacting on hyperbolic trajectories using the quadrupole approximation has been studied by Capozziello et al. [35] and analytic expressions for the total energy output derived. However, the energy spectrum has been computed only for the large eccentricity ($e \gg 1$) limit [37]. In this paper we derive the energy spectrum for hyperbolic encounters for all values $e \geq 1$ and we give an analytic expression for it in terms of Hankel functions. We checked numerically that our result in the limit of $e = 1$ is in agreement with the one for parabolic encounters [36] and for large eccentricities with the result given in [37].

4.2 Theoretical framework

Gravitational waves (GWs) are solutions of the linearized field equations of General Relativity and the radiated power to leading order is given by Einstein's quadrupole formula, as follows

$$P = \frac{G}{45\,c^5} \langle \dddot{D}_{ij}\, \dddot{D}_{ij} \rangle \,, \tag{4.1}$$

where we used as definition for the second moment tensors $M_{ij} = \frac{1}{c^2}\int T^{00} x_i x_j \,\mathrm{d}^3x$, and for the quadrupole moment tensor $D_{ij} = 3M_{ij} - \delta_{ij} M_{kk}$. Here and in the following dots denote time derivatives [1].
The quantity M_{ij} depends on the trajectories of the involved masses, and can easily be computed for all type of Keplerian trajectories. To compute the power spectrum, i.e. the amplitude of radiated power per unit frequency, requires a Fourier transform of equation (4.1), which is rather involved (for the elliptical case see e.g. [26]), and we will derive it below for hyperbolic encounters.
In Fig. 4.1 the geometry of an hyperbolic encounter is represented with the most important quantities we will use. Since we will compare our results with those of [36] and [35], it is important to note that not all these quantities are independent from each other, and we will need to know the relations between them. Notice that we assume that the gravitational energy loss during the encounter is negligible and thus that the Keplerian hyperbolic trajectory is a good approximation of the orbit. Clearly, this assumption does depend on the mass ratio and on the distance of closest approach. In the considered cases, where the masses are similar, this holds very well.
The eccentricity e of the hyperbola is (see e.g. [26])

$$e = \sqrt{1 + \frac{2\,E\,L^2}{\mu\,\alpha^2}} \,, \tag{4.2}$$

where $E = \frac{1}{2}\mu\, v_0^2$, since E is a conserved quantity we can take the energy at $t = -\infty$, v_0 being the velocity of the incoming mass m_1 at infinity, the angular momentum $L = \mu\, b\, v_0$, the impact parameter b, the total mass $m = m_1 + m_2$, the reduced mass $\mu = m_1 m_2/m$ and the parameter $\alpha = G\, m\, \mu$.

[1] Note that often in the literature (e.g. [26]) we also find the notation $Q_{ij} = \frac{D_{ij}}{3} = M_{ij} - \frac{1}{3}\delta_{ij} M_{kk}$, equation (4.1) reads then $P_{\mathrm{quad}} = \frac{G}{5\,c^5}\langle \ddot{Q}_{ij}\, \ddot{Q}_{ij} \rangle$. Here and in the following we will use the notation given by [35] and [40].

We notice that the orbit is characterized by only four quantities given as initial conditions: v_0, b and $m_{1,2}$. All the other parameters can be expressed as functions of this fundamental set. We can for instance rewrite the eccentricity as $e = \sqrt{1 + v_0^4\, b^2 \,/\, G^2\, m^2} = e\,(v_0, b, m)$, or the semi-major axis $a = \alpha/\mu v_0^2$, the angle at periastron through $\cos\varphi_0 = -1/e$, or the radius at periastron as $r_{min} = Gm/v_0^2\,(e-1)$, and so on.

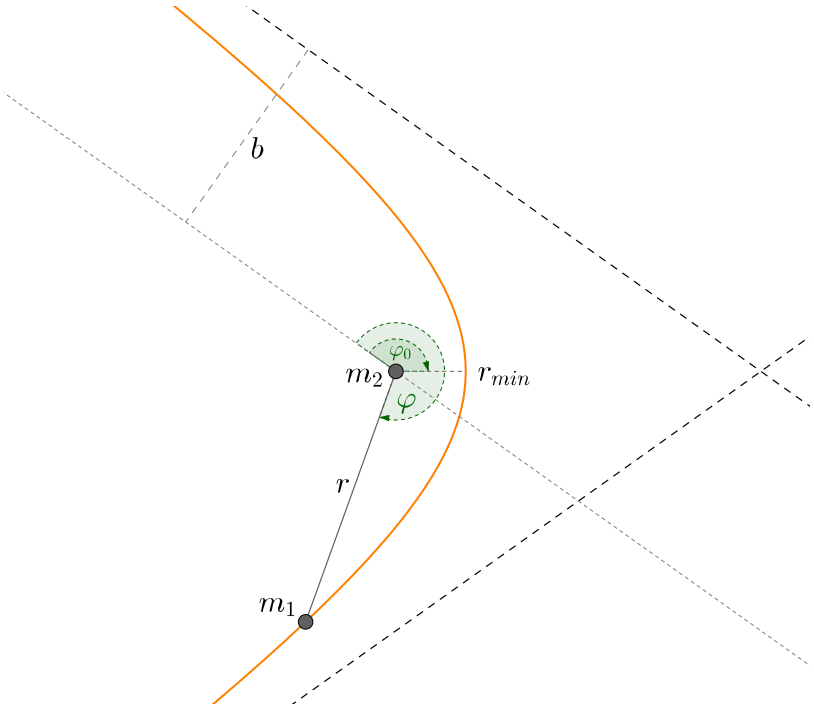

Figure 4.1: The geometry of an hyperbolic encounter and its most important parameters.

Setting the angle of the incident body to $\varphi = 0$ at initial time $t = -\infty$, the radius of the trajectory as a function of the angle and as a function of time is given by

$$r(\varphi) = \frac{a\,(e^2-1)}{1 + e\,\cos(\varphi - \varphi_0)}\,, \tag{4.3}$$

$$r(\xi) = a\,(e\,\cosh\xi - 1)\,, \tag{4.4}$$

with the time parametrized by ξ through the relation

$$t(\xi) = \sqrt{\frac{\mu\, a^3}{\alpha}}\,(e\,\sinh\xi - \xi)\,, \tag{4.5}$$

where ξ goes from $-\infty$ to $+\infty$. Expressing this in Cartesian coordinates in the orbital plane, we finally get the equations for hyperbolic trajectories

$$x(\xi) = a\,(e - \cosh\xi)\,, \tag{4.6}$$

$$y(\xi) = a\,\sqrt{e^2-1}\,\sinh\xi\,. \tag{4.7}$$

4.3 Power spectrum of Gravitational waves from hyperbolic paths

4.3.1 Power emitted per unit angle

In [35] the computation of the power emitted as a function of the angle, as well as the total energy emitted by the system has been already carried out. Here, we briefly present these computations, whose results we will then use.
First we compute the energy and angular momentum of a body within a gravitational potential $\Phi(r)$. In the plane of the orbit the velocity can be written in terms of a tangent and a perpendicular component

$$\mathbf{v} = v_r\,\hat{\mathbf{r}} + v_\varphi\,\hat{\boldsymbol{\varphi}} \tag{4.8}$$

where $v_r = \frac{dr}{dt}$, $v_\varphi = r\,\frac{d\varphi}{dt}$, and where vectors are represented by bold symbols. Thus the total energy per unit mass of the system and the angular momentum can be written as

$$E = \frac{1}{2}\,v^2 + \Phi(r) = \frac{1}{2}\left(\frac{dr}{dt}\right)^2 + \frac{1}{2}\,r^2\left(\frac{d\varphi}{dt}\right)^2 + \Phi(r)\,, \tag{4.9}$$

$$L = \mathbf{r}\times\mathbf{v} = r^2\,\frac{d\varphi}{dt}\,. \tag{4.10}$$

Putting these equations together, using the substitution $u = 1/r$ with $r^2 = L/\dot{\varphi}$ and rearranging, we get

$$\frac{2E}{L^2} = \frac{\dot{u}^2}{\dot{\varphi}^2} + u^2 + \frac{2\Phi}{L^2} = \left(\frac{du}{d\varphi}\right)^2 + u^2 + \frac{2\Phi}{L^2}\,. \tag{4.11}$$

Since E and L are conserved quantities, the derivative of the last expression with respect to u gives

$$0 = \frac{d^2u}{d\varphi^2} + u + \frac{1}{L^2}\,\frac{d\Phi}{du} \quad\Leftrightarrow\quad \frac{d^2u}{d\varphi^2} + u = \frac{G\,m_2}{L^2}\,. \tag{4.12}$$

This is an inhomogeneous linear differential equation of second order, which has the following solution

$$u(\varphi) = B\,\cos(\varphi-\varphi_0) + \frac{G\,m_2}{L^2}\,, \tag{4.13}$$

and substituting back to r we have $\dot{r} = B\,L\,\sin(\varphi-\varphi_0)$. B is a constant depending on the initial conditions and φ_0 is the polar angle corresponding to the periastron distance, i.e. the distance of closest approach between the two interacting bodies (see Fig. 4.1). Its relation to the eccentricity is given by

$$e = -1/\cos\varphi_0\,. \tag{4.14}$$

Using the initial condition for the velocity, and the standard procedure to reduce the two-body problem to a single reduced mass particle moving in a gravitational field generated by the total mass, we see that the orbit of this reduced mass particle reads

$$r(\varphi) = \frac{b\,\sin\varphi_0}{\cos(\varphi-\varphi_0) - \cos\varphi_0}\,. \tag{4.15}$$

In order to compute the emitted power P, given by the quadrupole formula, as a function of the angle, it is convenient to rewrite the Cartesian coordinates x_i in spherical coordinates (the

plane of the orbit corresponds to $\vartheta = \frac{\pi}{2}$) [2]

$$x = r\cos\varphi\sin\vartheta = r\cos\varphi\ , \tag{4.16}$$
$$y = r\sin\varphi\sin\vartheta = r\sin\varphi\ , \tag{4.17}$$
$$z = r\cos\vartheta = 0\ . \tag{4.18}$$

For the second momenta tensors M_{ij} we get accordingly

$$M_{11} = \mu x^2 = \mu r^2\cos^2\varphi\ , \tag{4.19}$$
$$M_{22} = \mu y^2 = \mu r^2\sin^2\varphi\ , \tag{4.20}$$
$$M_{12} = \mu xy = \mu r^2\cos\varphi\sin\varphi = M_{21}\ , \tag{4.21}$$
$$M_{32} = M_{23} = M_{33} = M_{13} = M_{31} = 0\ . \tag{4.22}$$

The term $\dddot{D}_{ij}\dddot{D}_{ij} = \sum_{i,j}\dddot{D}_{ij}\dddot{D}_{ij}$ in the expression for the radiated power can now be simplified to give

$$\langle\dddot{D}_{ij}\dddot{D}_{ij}\rangle\ = 6\,\langle\dddot{M}_{11}^2 + \dddot{M}_{22}^2 + 3\dddot{M}_{12}^2 - \dddot{M}_{11}\dddot{M}_{22}\rangle\ . \tag{4.23}$$

In order to compute this value explicitly, keeping φ as a variable instead of t, we have to transform derivatives in time in derivatives in φ and r. This yields

$$P(\varphi) = -\frac{32\,G\,L^6\mu^2}{45\,c^5\,b^8}f(\varphi,\varphi_0)\ , \tag{4.24}$$

with

$$f(\varphi,\varphi_0) = \frac{\sin(\varphi_0-\frac{\varphi}{2})^4\ \sin(\frac{\varphi}{2})^4}{\tan(\varphi_0)^2\ \sin(\varphi_0)^6}\times\Bigg(150 + 72\cos(2\varphi_0) + 66\cos(2\varphi_0-2\varphi) - 144\Big(\cos(2\varphi_0-\varphi)-\cos(\varphi)\Big)\Bigg)\ , \tag{4.25}$$

which is the result obtained in [35]. In Fig. 4.2 we plot the radiated power P as a function of the angle.

Eq. (4.24) can also be written as follows, using the Schwarzschild radius $r_s = 2Gm/c^2$, and $L = v_0\,b$

$$P = \frac{dE}{dt} = -\frac{4\,r_s v_0^6\,\mu}{45\,c^3\,b^2}f(\varphi,\varphi_0)\ . \tag{4.26}$$

Setting $t = 0$ at periastron, the total energy radiated in GWs by the system during the interaction is given by

$$\Delta E = \int_{-\infty}^{\infty}\left|\frac{dE}{dt}\right|\mathrm{d}t\ . \tag{4.27}$$

Since we know $\frac{dE}{dt}$ as function of φ rather than t, we perform a variable change in the integration and get

$$\Delta E = \frac{4\,r_s\,v_0^5\,\mu}{45\,c^3\,b}\int_{\varphi_1}^{\varphi_2}\frac{\sin^2\varphi_0\,f(\varphi,\varphi_0)}{[\cos(\varphi-\varphi_0)-\cos\varphi]^2}\,\mathrm{d}\varphi\ , \tag{4.28}$$

which can be evaluated taking $\varphi_1 = 0$ as initial angle, and $\varphi_2 = 2\varphi_0$ as the final angle

$$\Delta E = \frac{32\,G\,\mu^2\,v_0^5}{b\,c^5}F(\varphi_0)\ , \tag{4.29}$$

[2] Note that P depends on D_{ij}, which also depends on the x_i present in the integral definition of M_{ij}.

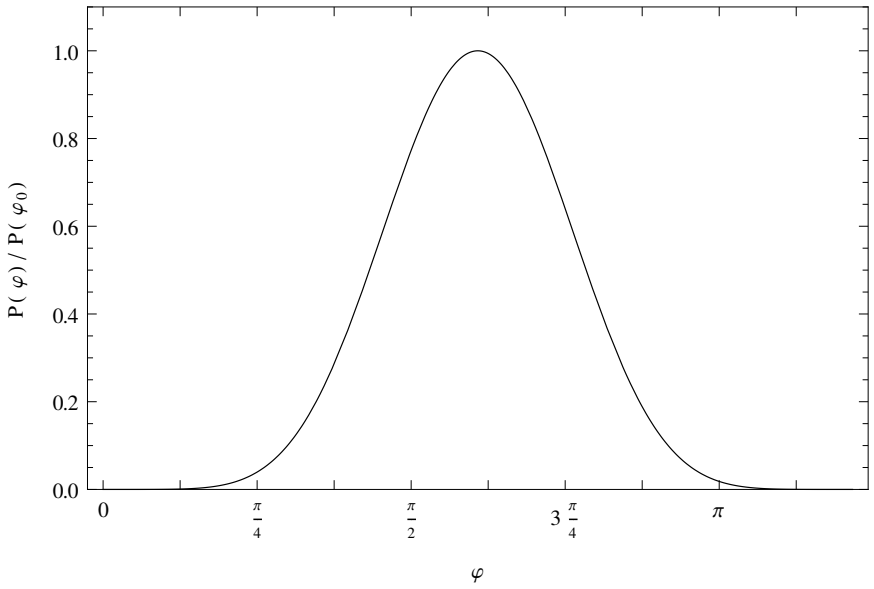

Figure 4.2: Radiated power as a function of the angle during an hyperbolic encounter, for $e = 3$, i.e. $\varphi_0 \simeq 0.6\pi$, according to the relation $e = -1/\cos\varphi_0$.

with

$$F(\varphi_0) = \frac{1}{720\,\tan^2\varphi_0\,\sin^4\varphi_0} \times \big[2628\varphi_0 + 2328\varphi_0\cos 2\varphi_0 + 144\varphi_0\cos 4\varphi_0 - 1948\sin 2\varphi_0 - 301\sin 4\varphi_0\big]\,. \tag{4.30}$$

This means that the total radiated energy of the system can be determined knowing the parameters b and v_0, and of course the mass μ.
In deriving the above equation the implicit assumption has been made, that the energy loss doesn't change the path of the body in the gravitational field, which is reasonable since the emitted energy in form of gravitational waves is rather small. As stated above, this holds very well for the cases we consider here, where the mass ratio is about 1.

4.3.2 Power spectrum

We compute now $P(\omega)$, the Fourier transform of $P(t)$, which describes the distribution of the amplitude of the power emitted in form of gravitational waves depending on the frequency. In the following we use the convention

$$\hat{f}(\omega) := \int_{-\infty}^{\infty} f(t)\, e^{-i\omega t}\, \mathrm{d}t \tag{4.31}$$

In [40] and [41] some hints are given when solving the analogous problem in electrodynamics. The crucial idea is to use Parseval's theorem on the integration of Fourier transforms first, and then to express some quantities in terms of Hankel functions. This allows to compute in an

easier way the Fourier transform of $P(t)$, for which we use the expression given in Eq. (4.1)

$$\begin{aligned}\Delta E = \int P(t)\mathrm{d}t \;&=\; \int P(\omega)\mathrm{d}\omega \;=\; \gamma \int \langle \dddot{D}_{ij}(t)\, \dddot{D}_{ij}(t)\rangle \,\mathrm{d}t \\ &= \gamma \int \left(|\widehat{\dddot{D}_{11}}(\omega)|^2 + |\widehat{\dddot{D}_{22}}(\omega)|^2 + 2|\widehat{\dddot{D}_{12}}(\omega)|^2 + |\widehat{\dddot{D}_{33}}(\omega)|^2\right) \mathrm{d}\omega \,, \end{aligned} \tag{4.32}$$

where $\widehat{\dddot{D}_{ij}}(\omega)$ represents the Fourier transform of $\dddot{D}_{ij}(t)$, and we introduced the constant $\gamma = -G/45c^5$.

It is easy to see that the last equation represents the total amount of energy dissipated in the encounter. Therefore, the integrand in the last line has to be equal to the power dissipated per unit frequency $P(\omega)$, i.e. :

$$P(\omega) = \gamma \left(|\widehat{\dddot{D}_{11}}(\omega)|^2 + |\widehat{\dddot{D}_{22}}(\omega)|^2 + 2|\widehat{\dddot{D}_{12}}(\omega)|^2 + |\widehat{\dddot{D}_{33}}(\omega)|^2\right) . \tag{4.33}$$

As next, we need to compute the $\widehat{\dddot{D}_{ij}}(\omega)$, to square their norm and sum them together in order to get the power spectrum. Note that first we compute the Fourier transform of $D_{ij}(t)$, then we differentiate three times, and only at the end we take the square of their norm. Computing the D_{ij} explicitly - keeping in mind that we use the time parametrization $t(\xi) = \sqrt{\mu\, a^3/\alpha}\,(e\,\sinh\xi - \xi)$ - we get:

$$D_{11}(t) = \frac{m\; a^2}{2}\left((3-e^2)\cosh 2\xi - 8\,e\cosh\xi\right) , \tag{4.34}$$

$$D_{22}(t) = \frac{m\; a^2}{2}\left(4\,e\cosh\xi + (2\,e^2-3)\cosh 2\xi\right) , \tag{4.35}$$

$$D_{33}(t) = \frac{-m\; a^2}{2}\left(4\,e\cosh\xi + e^2\cosh 2\xi\right) , \tag{4.36}$$

$$D_{12}(t) = \frac{3\; m\; a^2}{2}\sqrt{e^2-1}\,\left(2\,e\sinh\xi - \sinh 2\xi\right) . \tag{4.37}$$

The Fourier transform of the third derivatives of $D_{ij}(t)$ is given by

$$\widehat{\dddot{D}_{ij}}(\omega) = i\omega^3\, \widehat{D_{ij}}(\omega) \,, \tag{4.38}$$

thus we have just to compute $\widehat{D_{ij}}(\omega)$. To compute the Fourier transforms we can closely follow the calculations performed e.g. in [40], where the similar problem in electrodynamics of the emitted power spectrum for scattering charged particles on hyperbolic orbits is treated. In particular the following Fourier transforms are used

$$\widehat{\sinh\xi} = -\frac{\pi}{\omega e} H^{(1)}_{i\nu}(i\,\nu e) \,, \tag{4.39}$$

$$\widehat{\cosh\xi} = -\frac{\pi}{\omega} H^{(1)\,\prime}_{i\nu}(i\,\nu e) \,, \tag{4.40}$$

with

$$H^{(1)\,\prime}_{\tilde{\alpha}}(x) = \frac{1}{2}\left(H^{(1)}_{\tilde{\alpha}-1}(x) - H^{(1)}_{\tilde{\alpha}+1}(x)\right) , \tag{4.41}$$

where $H^{(1)}_{\tilde{\alpha}}(x)$ is the Hankel function of the first kind of order $\tilde{\alpha}$, defined as $J_{\tilde{\alpha}}(x) + iY_{\tilde{\alpha}}(x)$, with $J_{\tilde{\alpha}}(x), Y_{\tilde{\alpha}}(x)$ the Bessel functions of first and second kind, respectively, and where the frequency ν is defined as $\nu = \omega\sqrt{\frac{\mu a^3}{\alpha}}$.

Taking the above results for $D_{ij}(t)$ we get[3]

$$\widehat{D_{11}}(\omega) = \frac{a^2 m \pi}{4\omega}\left[16 e H_{i\nu}^{(1)\prime}(i\nu e) + (e^2-3) H_{i\nu}^{(1)\prime}(i\nu e/2)\right], \tag{4.42}$$

$$\widehat{D_{22}}(\omega) = \frac{a^2 m \pi}{4\omega}\left[(3-2e^2) H_{i\nu}^{(1)\prime}(i\nu e/2) - 8 e H_{i\nu}^{(1)\prime}(i\nu e)\right], \tag{4.43}$$

$$\widehat{D_{33}}(\omega) = \frac{a^2 m \pi}{4\omega}\left[8 e H_{i\nu}^{(1)\prime}(i\nu e) + e^2 H_{i\nu}^{(1)\prime}(i\nu e/2)\right], \tag{4.44}$$

$$\widehat{D_{12}}(\omega) = \frac{3 a^2 m \pi}{4\omega e}\sqrt{e^2-1}\left[H_{i\nu}^{(1)}(i\nu e/2) - 4 e H_{i\nu}^{(1)}(i\nu e)\right]. \tag{4.45}$$

Inserting this result into Eq. (4.33), using Eq. (4.38), we get the power spectrum of the gravitational wave emission for hyperbolic encounters

$$P(\omega) = -\frac{G a^4 m^2 \pi^2}{720 c^5}\,\omega^4\, F_e(\omega), \tag{4.46}$$

where the function $F_e(\omega)$ is

$$\begin{aligned} F_e(\omega) \;=\; & \left|\left[16 e H_{i\nu}^{(1)\prime}(i\nu e) + (e^2-3) H_{i\nu}^{(1)\prime}(i\nu e/2)\right]\right|^2 + \\ & \left|\left[(3-2e^2) H_{i\nu}^{(1)\prime}(i\nu e/2) - 8 e H_{i\nu}^{(1)\prime}(i\nu e)\right]\right|^2 + \\ & \left|\left[8 e H_{i\nu}^{(1)\prime}(i\nu e) + e^2 H_{i\nu}^{(1)\prime}(i\nu e/2)\right]\right|^2 + \\ & \frac{9(e^2-1)}{e^2}\left|\left[H_{i\nu}^{(1)}(i\nu e/2) - 4 e H_{i\nu}^{(1)}(i\nu e)\right]\right|^2. \end{aligned} \tag{4.47}$$

In Fig. 4.3 the function $\omega^4 F_e(\omega)$ is plotted for some some values of e: this is the frequency power spectrum of gravitational radiation emitted by an hyperbolic encounter. Unfortunately the expression for $F_e(\omega)$ is rather complicated and we could not find an analytical way to simplify it. We thus made some numerical tests to check its validity and clearly the integral of (4.46) has to be equal to ΔE in (4.29), which was obtained by integrating over the power emitted per unit frequency, i.e.:

$$\int_0^\infty P(\omega)\,\mathrm{d}\omega = \Delta E\,. \tag{4.48}$$

We have checked the validity of this equality for different sets of values, comparable to those used in [35], e.g. $b = 1\mathrm{AU}$, $v_0 = 200$ km/s, and $m_{1,2} = 1.4\,\mathrm{M}_\odot$, or similar.
For all of these sets we got agreement within numerical accuracy.
More interesting is the case where the eccentricity approaches $e = 1$. According to Eq. (4.2) this is the case e.g. with the set of initial conditions $b = 2$ AU, $v_0 = 6.4$ km/s and $m_{1,2} = 1.4\,M_\odot$. Since this is a limit case for a parabolic trajectory, we can directly compare our result with the one studied by [36], and indeed they coincide, within numerical accuracy. For a discussion about the feasibility of an analytical comparison see Appendix B.

[3]Notice that we obtain also constant terms in these four equations. However, they can be dropped, since we can freely change the origin of coordinates while keeping invariant the description of the quadrupole radiation, as explained e.g. in [26] in section 3.3.5. Note also that in fact these terms would in any case vanish for merely mathematical reasons, since the Fourier transform would multiply them with a Dirac delta function $\delta(\omega)$ and a factor $(-i\omega)^3$ from the third derivative. This expression vanishes for all $\omega \neq 0$ because of the $\delta(\omega)$, and for $\omega = 0$ because of the multiplying factor $(-i\omega)^3$.

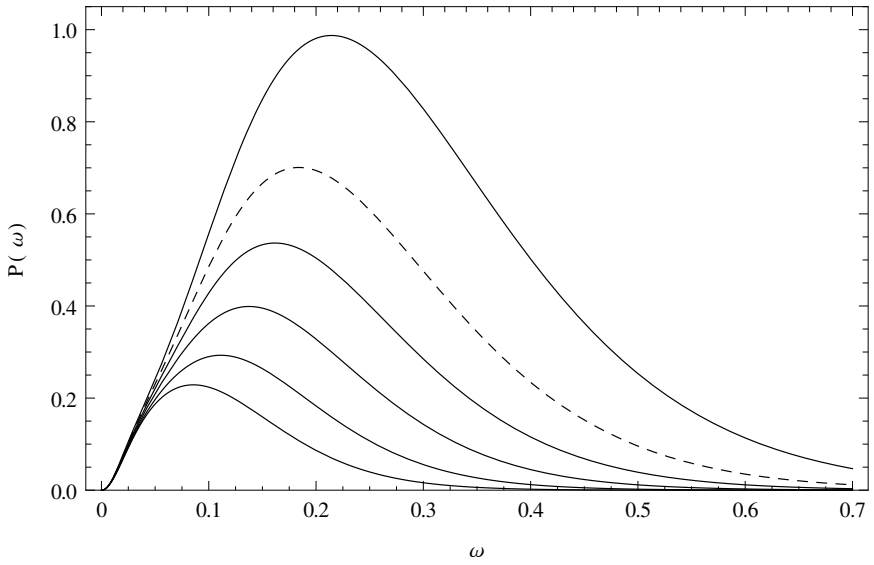

Figure 4.3: The frequency power spectrum of gravitational radiation emitted by an hyperbolic encounter. On the x-axis we have the angular frequency ω expressed in mHz units, whereas on the y-axis the amplitude of $P(\omega)$ is normalized to the maximum value of the $e \sim 2.5$ case. These are the expected emissions generated by a system of two supermassive black holes with $m = 10^7 M_\odot$, impact parameter $b = 10$ AU, and different relative velocities. With lower velocities the interactions are stronger and the eccentricity decreases. These spectra, in order from the highest to the lowest, represent systems with $v_0 = 3.4 \times 10^7$ m/s ($e \sim 2.5$), $v_0 = 3.5 \times 10^7$ m/s ($e \sim 3$), $v_0 = 3.6 \times 10^7$ m/s ($e \sim 3.1$), $v_0 = 3.75 \times 10^7$ m/s ($e \sim 3.4$), $v_0 = 4 \times 10^7$ m/s ($e \sim 3.8$), $v_0 = 4.5 \times 10^7$ m/s ($e \sim 4.7$), respectively. In particular the case with $e \sim 3$ (plotted with the dashed line) is discussed in the conclusions. As one can see, for higher eccentricities the peak frequency slowly decreases. This is only true for values of v_0 up to $\sim 6 \times 10^7$ m/s, whereas above it increases again. Moreover, decreasing the mass or increasing the impact parameter changes the eccentricity as well. We should be able to detect incoming waves in that range e.g. with eLISA, since the peak at ~ 0.2 mHz fits in its observable band. For a more detailed discussion see Sec. 4.4. and e.g. [31].

4.3.3 The limit for $e \gg 1$

As next we turn to the large e limit and compare our result with the one given in [37] and [42]. The expression for the total energy emitted during an hyperbolic interaction is written in [37] as

$$\Delta E = \frac{8}{15}\frac{G^{7/2}}{c^5}\frac{m^{1/2}\, m_1^2\, m_2^2}{r_{min}^{7/2}}\; g(e)\,, \tag{4.49}$$

where r_{min} is the radius at periastron, and the enhancement factor $g(e)$ turns out to be

$$\frac{24 \arccos\left(\frac{-1}{e}\right)\left(1 + \frac{73}{24}e^2 + \frac{37}{96}e^4\right) + \sqrt{e^2-1}\left(\frac{301}{6} + \frac{673}{12}e^2\right)}{(e+1)^{7/2}}\,. \tag{4.50}$$

Clearly this expression is equivalent to our result (4.29) for all values of $e > 1$. Indeed, using the following relations for the radius r_{min} and the angle φ_0 at periastron:

$$e = \frac{-1}{\cos\varphi_0}\,, \quad r_{min} = r(\varphi_0) = b\frac{\sin\varphi_0}{1-\cos\varphi_0} = \frac{Gm}{v_0^2}(e-1)\,, \tag{4.51}$$

both expressions can be written as functions of only three parameters describing the encounter: e, m and v_0, and it is then straightforward to see that

$$\Delta E_Q = \Delta E_T \ , \tag{4.52}$$

where ΔE_Q denotes the energy computed according to Eq. (4.29) and ΔE_T the one according to Eq. (4.49).

Following [37] again, we find out that in the limit for large e, the $g(e)$ factor can be simplified and written as:

$$\tilde{g}(e) = \frac{37\pi}{8}\sqrt{e} \ + \ \mathcal{O}(\, e^{-1/2}) \ , \tag{4.53}$$

which also agrees with the result of Wagoner and Will [42]. This yields a simple form for the energy emitted during the path:

$$\Delta \tilde{E}_T = \frac{8}{15}\frac{G^{7/2}}{c^5}\frac{m^{1/2}\, m_1^2\, m_2^2}{r_{min}^{7/2}}\ \tilde{g}(e) \ , \tag{4.54}$$

That leads then to the formula for the energy spectrum valid for large e:

$$\begin{aligned} P(\sigma) = \frac{G^{7/2} m^{1/2}\, m_1^2\, m_2^2}{c^5 \quad r_{min}^{7/2}}\frac{8}{15\pi}\sqrt{e} \ \times \ \Big\{ 12 \left[\sigma^2 K_2(\sigma) - \sigma K_1(\sigma) \right]^2 \\ + 3 \left[\, 2\sigma^2 K_1(\sigma) + \sigma K_0(\sigma) \right]^2 + \sigma^2 K_0^2(\sigma) \Big\} \ , \end{aligned} \tag{4.55}$$

where $K_{\tilde{\alpha}}(x)$ are the modified Bessel functions of the second kind, σ is the frequency rescaled $\sigma = \omega\tau$, in terms of the characteristic time scale τ of the gravitational wave, which is defined as τ =(periastron distance)/(periastron velocity).

Comparing our total energy from the quadrupole approximation, Eq. (4.29), with the expression for the energy $\Delta \tilde{E}_T$ (4.54) by [37] with the simplified factor (4.53) valid in the large e limit, we see that they coincide for large eccentricities, having e.g. a 1% difference after $e = 100$, and a 5% difference after $e = 20$ as shown in Fig. 4.4.
In fact we see that the behavior of the variation goes as $(\Delta E_Q - \Delta \tilde{E}_T)/\Delta \tilde{E}_T \propto 1/e$, confirming the fact that for the parabolic limit $\Delta E_Q = 2\,\Delta \tilde{E}_T$, so that one would underestimate the energy emitted by a factor of 2 taking this approximation [37].

4.4 Conclusions

Short gravitational wave burst-like signals are expected in the data stream of detectors. Although these signals will likely be too short to allow us to measure the parameters of the emitting system accurately, the results presented in this paper could be used to get a rough estimate of these parameters, by observing the position of the peak, the amount of energy released and the timescale of the interaction.
Given the knowledge of the power spectrum we can easily see which kind of hyperbolic encounters could generate gravitational waves detectable e.g. with eLISA, advanced LIGO or advanced VIRGO. Measurements from unbound interactions with ground-based detectors could

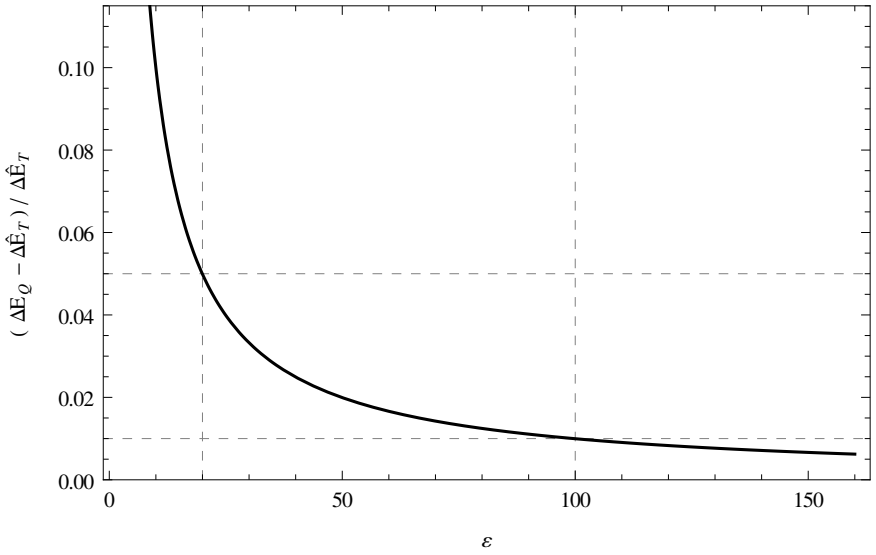

Figure 4.4: The converging behavior of the total energy emitted in an hyperbolic encounter according to the quadrupole approximation ΔE_Q, Eq. (4.29), towards the result of [37], Eq. (4.49). The plotted line is $(\Delta E_Q - \Delta\tilde{E}_T)/\Delta\tilde{E}_T$ as function of the eccentricity e.

in principle be possible, though the energy emitted at e.g. ±200 Hz is below the minimum threshold for advanced LIGO or advanced VIRGO, making detections unlikely but not impossible. The space-based interferometer instead is expected to cover frequencies ranging from 0.03 mHz up to 1 Hz (see e.g. [31]), where the interactions could release more energy.
An unbounded collision between two intermediate-mass black holes, let's say of $10^3 M_\odot$ each, with an encounter velocity of 2000 km/s at a distance of 1 AU, would generate, according to our Eq. (4.46), a frequency spectrum with peak around 0.04 mHz, with 80% of the emission in the range between 0.01 and 0.07 mHz, i.e. in the lower range limit of eLISA. Another possible example of measurable impact would be an encounter between two supermassive black holes with mass, e.g., comparable to the expected mass of Sagittarius A*, the black hole believed to be at the center of our galaxy, i.e. $\sim 10^7 M_\odot$. With a distance of some AU, and a high velocity (we want to exclude the bounded case) of tens of thousands km/s, such a collision would generate an energy spectrum with peak at ~ 0.2 mHz with 80% between 0.03 and 0.37 mHz, thus in the observable range of eLISA. (Its energy spectrum is plotted with a dashed line in Fig. 4.3.)
Interestingly, the time window of such events is enough to allow measurements. Indeed, for encounters up to $e \sim 5$ with peak in the mHz to Hz regime, we are in the time scale of 1 day, if we choose the cutoff of the interaction at an angle of $\varphi = 3/4\,\varphi_0$, i.e. where the path starts to approach significantly the asymptote (see Fig. 4.1). For instance, for the two examples above, the interactions would last about 54h and 9h, respectively. Estimates for the rate of such events have been considered e.g. in [43]. They consider e.g. typical compact stellar cluster around the Galactic Center, and expect an event rate of 10^{-3} up to unity per year, depending on the radius of the object and the amount of such clusters in the near region.
After a discussion with L. Blanchet we realized that there is a possibility to treat the problem in an alternative way. Starting from the Keplerian equations of motion, one could take the solution of Peters and Mathews [38], bring the argument onto the imaginary axis and - making use of equations (9.6.2-9.6.4) in Abramowitz & Stegun [44] - find the energy spectrum in terms of Hankel functions.

We believe that with the wave-form found here one should be able to classify the different encounters depending on the detected shape, and therefore get a better insight into the map of our galaxy or the near universe.

4.5 Acknowledgments

We thank N. Straumann for useful discussions and for bringing to our attention the relevant treatment of the hyperbolic problem in electrodynamics in Landau & Lifschitz. We also thank L. Blanchet for his encouragement and for pointing out the possibility of treating the same problem in another way, as discussed in the conclusions. Finally, we would also like to thank the referee for useful comments, and C. Berry for helping clarifying some details.

4.6 Appendix

4.6.1 On the Fourier Transform of $\sinh\xi$ and $\cosh\xi$

In section 4.3.2 we used the relations (4.39-4.40) without any proof. Since we didn't find any reference where the proof is shown explicitly, we will show in the following where these two relations arise from. In Landau and Lifshitz [40] the equations we used in the cited section are

$$\widehat{\sinh\xi} = -\frac{\pi}{\omega e} H_{i\nu}^{(1)}(i\nu e)\,, \tag{4.56}$$

$$\widehat{\cosh\xi} = -\frac{\pi}{\omega} H_{i\nu}^{(1)\,\prime}(i\nu e)\,, \tag{4.57}$$

but in fact the general relations we want to show - [40], §70, equation (70.15) - are

$$\widehat{y(t)} = \frac{a\sqrt{e^2-1}\,\pi}{\omega e} H_{i\nu}^{(1)}(i\nu e)\,, \tag{4.58}$$

$$\widehat{x(t)} = \frac{a\,\pi}{\omega} H_{i\nu}^{(1)\,\prime}(i\nu e)\,. \tag{4.59}$$

I. Fourier Transform of $y(t)$

We know that the time can also be parametrized with ξ using the transformation

$$t(\xi) = \sqrt{\frac{\mu a^3}{\alpha}}\,(e\,\sinh\xi - \xi) \tag{4.60}$$

which allows to write

$$y(\xi) = a\sqrt{e^2-1}\,\sinh\xi \tag{4.61}$$

We can now start with the computation of the Fourier transform:

$$\begin{aligned}\widehat{y}(\omega) :&= \int_{-\infty}^{\infty} y(t)\, e^{-i\omega t}\, dt = \int_{-\infty}^{\infty} y(\xi)\, e^{-i\omega t(\xi)}\, \frac{dt(\xi)}{d\xi}\, d\xi = \int_{-\infty}^{\infty} y(\xi)\, \frac{-1}{i\omega}\, \frac{d}{d\xi} e^{-i\omega t(\xi)}\, d\xi \\ &= -\frac{a\sqrt{e^2-1}}{i\,\omega} \int_{-\infty}^{\infty} \sinh\xi\, \frac{d}{d\xi} e^{-i\omega t(\xi)}\, d\xi \overset{(*^1)}{=} \frac{a\sqrt{e^2-1}}{i\,\omega} \int_{-\infty}^{\infty} \cosh\xi\, e^{-i\omega t(\xi)}\, d\xi \\ &= \frac{a\sqrt{e^2-1}}{i\,\omega} \int_{-\infty}^{\infty} (\cosh\xi - \frac{1}{e} + \frac{1}{e})\, e^{-i\omega t(\xi)}\, d\xi \\ &= \frac{a\sqrt{e^2-1}}{i\,\omega\, e} \Big[\underbrace{\int_{-\infty}^{\infty} (e\,\cosh\xi - 1)\, e^{-i\omega t(\xi)}\, d\xi}_{\mathscr{A}} + \underbrace{\int_{-\infty}^{\infty} e^{-i\omega t(\xi)}\, d\xi}_{\mathscr{B}} \Big] \end{aligned} \tag{4.62}$$

We now compute separately $\mathscr{A}$ and $\mathscr{B}$:

$$\mathscr{A} = \int_{-\infty}^{\infty} \frac{dt}{d\xi} \sqrt{\frac{\alpha}{\mu\, a^3}}\, e^{-i\omega t(\xi)}\, d\xi = \sqrt{\frac{\alpha}{\mu\, a^3}} \int_{-\infty}^{\infty} \frac{-1}{i\omega}\, \frac{d}{d\xi}\, e^{-i\omega t(\xi)}\, d\xi \overset{(*^2)}{=} 0 \tag{4.63}$$

$$\mathscr{B} = \int_{-\infty}^{\infty} e^{-i\omega\sqrt{\frac{\mu a^3}{\alpha}}\,(e\,\sinh\xi - \xi)}\, d\xi = \int_{-\infty}^{\infty} e^{-i\,\nu e\,\sinh\xi + i\,\nu\xi}\, d\xi \overset{(*^3)}{=} i\pi\, H_{i\nu}^{(1)}(i\,\nu e) \tag{4.64}$$

Hence we have:

$$\widehat{y}(\omega) = \frac{a\sqrt{e^2-1}}{i\,\omega\, e} \Big[0 + i\pi\, H_{i\nu}^{(1)}(i\,\nu e) \Big] = \frac{a\sqrt{e^2-1}\,\pi}{\omega e} H_{i\nu}^{(1)}(i\,\nu e) \tag{4.65}$$

■

where $(*^1)$ follows from partial integration and the boundaries vanish, we have the same situation for $(*^2)$, and in $(*^3)$ we used the defining relation of the Hankel functions.

II. Fourier Transform of $x(t)$

We now show equation (4.59) in a similar way: again with the time parametrization through ξ we can write

$$x(\xi) = a\,(e - \cosh\xi) \tag{4.66}$$

Its Fourier transform can be taken as follows:

$$\begin{aligned}
\widehat{x}(\omega) :&= \int_{-\infty}^{\infty} x(t)\, e^{-i\omega t}\, dt = \int_{-\infty}^{\infty} x(\xi)\, e^{-i\omega t(\xi)}\, \frac{dt(\xi)}{d\xi}\, d\xi = \int_{-\infty}^{\infty} x(\xi)\, \frac{-1}{i\omega}\, \frac{d}{d\xi}\, e^{-i\omega t(\xi)}\, d\xi \\
&= \frac{-a}{i\omega} \int_{-\infty}^{\infty} (e - \cosh\xi)\, \frac{d}{d\xi}\, e^{-i\omega t(\xi)}\, d\xi = \frac{-a}{i\omega} \int_{-\infty}^{\infty} \sinh\xi\, e^{-i\omega t(\xi)}\, d\xi \\
&= \frac{-a}{i\omega} \int_{-\infty}^{\infty} \frac{e^{\xi} - e^{-\xi}}{2}\, e^{-i\omega t(\xi)}\, d\xi = \frac{-a}{i\omega} \int_{-\infty}^{\infty} \frac{e^{\xi} - e^{-\xi}}{2}\, e^{-i\nu e\sinh\xi + i\nu\xi}\, d\xi \\
&= \frac{-a}{i\omega}\, \frac{1}{2} \Big[\int_{-\infty}^{\infty} e^{\xi}\, e^{-i\nu e\sinh\xi + i\nu\xi}\, d\xi - \int_{-\infty}^{\infty} e^{-\xi}\, e^{-i\nu e\sinh\xi + i\nu\xi}\, d\xi \Big] \\
&= \frac{-a}{i\omega}\, \frac{1}{2} \Big[\int_{-\infty}^{\infty} e^{-i\nu e\sinh\xi + (i\nu+1)\xi}\, d\xi - \int_{-\infty}^{\infty} e^{-i\nu e\sinh\xi + (i\nu-1)\xi}\, d\xi \Big] \\
&= \frac{-a}{i\omega}\, \frac{1}{2} \Big[i\pi H^{(1)}_{i\nu+1}(i\nu e) - i\pi H^{(1)}_{i\nu-1}(i\nu e) \Big] \qquad (4.67) \\
&= \frac{a\pi}{\omega}\, \frac{1}{2} \Big[H^{(1)}_{i\nu-1}(i\nu e) - H^{(1)}_{i\nu+1}(i\nu e) \Big] \qquad (4.68)
\end{aligned}$$

Hence, using the formula for the derivative given in (4.41) we get:

$$\widehat{x}(\omega) = \frac{a\pi}{\omega} H^{(1)\,\prime}_{i\nu}(i\nu e) \qquad (4.69)$$

■

4.6.2 Analytical comparison of the parabolic limit

In section 4.3.2 we discuss the parabolic limit of our result for the energy spectrum, where $e \to 1$. A numerical check of its validity with respect to the previous known quantity, in [36], is quite straightforward. Nevertheless it would be interesting to find an analytical agreement between these two formulae.
Taking that limit the last part of our equations drops away, and only three terms remain. These can be greatly simplified, since in the $e = 1$ limit the second and third are similar and $F_e(\omega)$ becomes

$$F_e(\omega) = \left[16 H^{(1)\,\prime}_{i\nu}(i\nu e) - 2 H^{(1)\,\prime}_{i\nu}(i\nu e/2)\right]^2 + 128 \left[H^{(1)\,\prime}_{i\nu}(i\nu e)\right]^2 + 2 \left[H^{(1)\,\prime}_{i\nu}(i\nu e/2)\right]^2 . \qquad (4.70)$$

Following the book by Abramowitz & Stegun [44] and the work done in [36] we see two facts. First, the frequency in the order of these functions goes as $(1-e)^{-3/2}$ (see Eq. (10) in [36]), and therefore in the limit $e \to 1$, ν goes to infinity. Second, we note that the order is also in the argument, therefore when $\nu \to \infty$ we can write the Hankel functions in terms of Airy functions $\mathrm{Ai}(x)$, e.g. Eq. (9.3.45) in [44]:

$$H^{(1)\,\prime}_{i\nu}(i\nu e) \propto \left\{ \frac{\mathrm{Ai}(e^{2\pi i/3}\nu^{2/3}\zeta)}{\nu^{4/3}} \sum_{k=0}^{\infty} \frac{c_k(\zeta)}{\nu^{2k}} + \frac{\mathrm{Ai}'(e^{2\pi i/3}\nu^{2/3}\zeta)\, e^{2\pi i/3}}{\nu^{2/3}} \sum_{k=0}^{\infty} \frac{d_k(\zeta)}{\nu^{2k}} \right\}, \qquad (4.71)$$

where ζ is a function of e defined as

$$\frac{2}{3}\zeta^{3/2} = \ln\frac{1+\sqrt{1-e^2}}{e} - \sqrt{1-e^2}\,, \qquad (4.72)$$

see Eq. (9.3.38) in [44]. If we only take the first order of the series, we have for the derivatives a term in $\mathrm{Ai}(x)$ and one in $\mathrm{Ai}'(x)$. Again using [44] we find Eq. (10.4.26 - 10.4.31) which express these terms in form of modified Bessel functions of the second kind:

$$K_{\pm 1/3}(\zeta) = \pi\sqrt{3/z}\,\mathrm{Ai}(z)\,, \tag{4.73}$$

$$K_{\pm 2/3}(\zeta) = -\pi\sqrt{3}/z\,\mathrm{Ai}'(z)\,, \tag{4.74}$$

where $z = \left(\frac{3}{2}\zeta\right)^{2/3}$.
We see now that equation (4.70) has the very same structure as Eq. (24) in [36]:

$$\ell(\tilde{f}) = \left[\, 8\mathscr{B}(\tilde{f}) - 2\mathscr{A}(\tilde{f}) \,\right]^2 + C\,\left[\, \mathscr{A}(\tilde{f}) \,\right]^2 + D\,\left[\, \mathscr{A}(\tilde{f}) \,\right]^2 \tag{4.75}$$

where $\mathscr{A}(\tilde{f})$ and $\mathscr{B}(\tilde{f})$ are also in terms of modified Bessel functions of the second kind of order $\pm 1/3$, $\pm 2/3$. At this point with some cumbersome algebra one should find that also all the coefficients of (4.71) and (4.75) agree.

Chapter 5

Gravitational waves from spinning compact binaries in hyperbolic orbits

L. De Vittori, A. Gopakumar, A. Gupta, Ph. Jetzer

*Published in Physical Review D, Volume **90**, 124066 (2014)* [2]

Abstract

Compact binaries in hyperbolic orbits are plausible gravitational wave sources for the upcoming and planned GW observatories. We develop an efficient prescription to compute post-Newtonian (PN) accurate ready-to-use GW polarization states for spinning compact binaries, influenced by the dominant order spin-orbit interactions, in hyperbolic orbits. This is achieved by invoking the 1.5PN accurate quasi-Keplerian parameterization for the radial sector of the orbital dynamics. We probe the influences of spins and gravitational radiation reaction on h_+ and $h_\times$ during the hyperbolic passage. It turns out that both polarization states exhibit the memory effect for GWs from spinning compact binaries in hyperbolic orbits. In contrast, only cross polarization state exhibits the memory effect for GWs from non-spinning compact binaries. Additionally, we compute 1PN accurate amplitude corrected GW polarization states for hyperbolic non-spinning compact binaries in a fully parametric manner and perform initial comparisons with the existing waveforms.

5.1 Introduction

Compact binaries in unbound orbits are plausible GW sources for both the ground and space based GW observatories [24]. These rare events are expected to occur in dense stellar environments that are present in globular clusters and galactic nuclear clusters [45]. Interestingly, such close encounters can, in principle, create bound binaries having very high eccentricities [46, 47]. For the ground based detector like the advanced LIGO [30], the plausible detection rates for such eccentric binaries may become comparable to that for isolated compact

binary coalescences, estimated to be between few to thousands per year [48]. Very recently, it was pointed out that electro-magnetic flares may accompany close encounters associated with compact binaries in hyperbolic orbits, provided such binaries contain a neutron star [49]. These electro-magnetic flashes, termed as the resonant shattering flares, arise due to the possible crustal shattering of the neutron star during its hyperbolic passage. The shattering develops because of the excitation of certain interface modes due to the extraction of orbital kinetic energy through resonant tidal coupling. This astrophysically plausible scenario should be an interesting candidate for triggered GW burst searches as it involves certain electro-magnetic flares of estimated luminosity $\sim 10^{47}$erg/s [49].

The investigations dealing with compact binaries in hyperbolic orbits had a chequered history and we begin by listing papers that provided inputs required to construct the associated GW polarization states. The quadrupolar order gravitational radiation field associated with two non-spinning compact objects moving in Newtonian hyperbolic orbits was analyzed by Turner [37]. Its extension to the first post-Newtonian (1PN) order is available in Ref. [50] while invoking the quasi-Keplerian approach to describe 1PN accurate hyperbolic orbits [51]. Note that the 1PN accurate orbital dynamics include general relativity based corrections to compact binary dynamics that are accurate to $(v/c)^2$ order beyond the Newtonian description, where v and c are the orbital and light speeds, respectively. The explicit 1PN order amplitude corrected expressions for the two GW polarization states, h_+ and $h_\times$, are available in Ref. [52]. This paper employed certain generalized true anomaly parameterization, detailed in Ref. [53], to describe 1PN accurate hyperbolic orbits. Additionally, there exists a number of investigations that probed various theoretical and observational aspects of non-spinning compact binaries in hyperbolic orbits. This includes quadrupolar order energy and angular momentum losses during hyperbolic encounters and its 1PN extensions [42, 54]. Aspects of gravitational bremsstrahlung involving large eccentricities and impact parameters were investigated in Ref. [55]. Recently, Ref. [1] obtained a general analytic formula for the GW energy spectrum associated with compact binaries in unbound orbits that generalized the parabolic limit computed in Ref. [36]. The quadrupolar order GW strain amplitudes and certain crude estimates for the expected rates of close gravitational flybys for terrestrial GW interferometers were reported in Ref. [35]. It was argued in Ref. [56] that GW burst signals, associated with stellar mass compact objects in nearly parabolic orbits around massive black hole (BH), should be present in a LISA-type space based GW observatory data streams. More recently, event rates for such extreme-mass-ratio bursts and the associated GW measurement accuracies for the massive BH mass and spin were explored in Refs. [57–59].

In this paper, we obtain temporally evolving GW polarization states for spinning compact binaries in PN accurate hyperbolic orbits. The spin effects are due to the leading order spin-orbit interactions, as detailed in Ref. [60], and the conservative non-spinning orbital dynamics is 1PN accurate. This implies that our orbital dynamics is fully 1.5PN accurate while considering compact binaries containing maximally spinning BHs. This is because the spin-orbit contributions to the orbital dynamics manifest at 1.5PN order for maximally spinning BH binaries [61]. Additionally, we incorporate the quadrupolar order gravitational radiation reaction effects while computing $h_+(t)$ and $h_\times(t)$. The plots for GW polarization states having quadrupolar order amplitudes and PN accurate orbital evolution reveal that both polarization states exhibit the *memory effect* with the inclusion of spin effects. In contrast, only the plus polarization state exhibits the memory effect for non-spinning compact binaries [50, 62, 63]. Recall that Ref. [64] coined the non-vanishing difference between the wave amplitudes at $t = \pm\infty$ as the *memory effect* while dealing with non-spinning compact binaries. This is a *linear* memory effect in contrast to the non-linear memory effect present in GW polarization states for compact binaries

in bound orbits [63]. The influences of orbital eccentricity, mass ratio and initial dominant spin orientation on the observed memory effect are also probed. We observe that the memory amplitude approaches zero as orbital eccentricity tends to unity while time domain GW polarization states develop sharply varying features for low eccentricities. The GW memory amplitude is larger for the cross polarization compared to the plus polarization and weakly depends on the mass ratio. The amplitude of the memory effect slowly changes as we vary the initial orientation of the dominant spin. These changes are more visible for the plus polarization state for higher eccentricities. Additionally, we provide 1PN accurate amplitude corrected expressions for the two GW polarization states associated with hyperbolic spinning compact binaries in a fully parametric way. These expressions generalize the computations of Ref. [52] that dealt with non-spinning compact binaries in hyperbolic orbits. We observe that our approach to compute $h_+(t)$ and $h_\times(t)$ should be accurate and computationally cheaper than the one in [52]. This is because of invoking Mikkola's method [65] to solve the 1PN accurate Kepler Equation for hyperbolic orbits.

We provide an explanation for the presence of the linear memory effect in both the polarization states for spinning compact binaries in hyperbolic orbits. For this purpose, we follow the arguments that are used to explain the presence of this effect in certain components of the far-zone metric associated with non-spinning compact binaries in hyperbolic orbits. We show that these arguments ensure the presence of the linear memory effect in the quadrupolar order cross polarization state for non-spinning compact binaries in hyperbolic orbits. This is beneficial as we can pinpoint terms that cause the effect in the case of non-spinning compact binaries. In contrast, we argue that the memory effect arises from the combined influences of a number of terms that are present in both polarization states associated with spinning compact binaries. Invoking non-spinning compact binaries in PN accurate orbits also allow us to compare GW polarization states from our approach with those available in the literature. Influenced by Figs. 6 to 10 in Ref. [52], we plot Newtonian, 0.5PN and 1PN contributions to h_+ and $h_\times$ for non-spinning compact binaries in hyperbolic orbits. A visual comparison reveals substantial differences the way Newtonian and 0.5PN contributions to $h_\times$ evolve during the hyperbolic passage in our approach and the one detailed in Ref. [52]. However, the plots in Fig. 8 of Ref. [52] for their 1PN order multipolar corrections to h_+ and $h_\times$ look qualitatively similar to our plots for the 1PN order amplitude corrections to GW polarizations states. We provide a possible qualitative explanation for these differences. Our approach indeed reproduces the temporal evolution for the real and imaginary parts of the time derivatives of mass and current multipole moments and associated GW modes computed in Refs. [50, 63]. We have invoked Fig. 8 in [50] and Fig. 2 in [63] for such comparisons.

The paper is organized in the following way. In Sec. 5.2 we present our approach to obtain temporally evolving GW polarization states for spinning compact binaries in hyperbolic orbits during their close encounters. We focus on non-spinning compact binaries in Sec. 5.3 influenced by Ref. [52] and visually compare the evolution of $h_\times$ and h_+ in these two approaches. A brief summary, possible consequences and extensions are listed in Sec. 5.4.

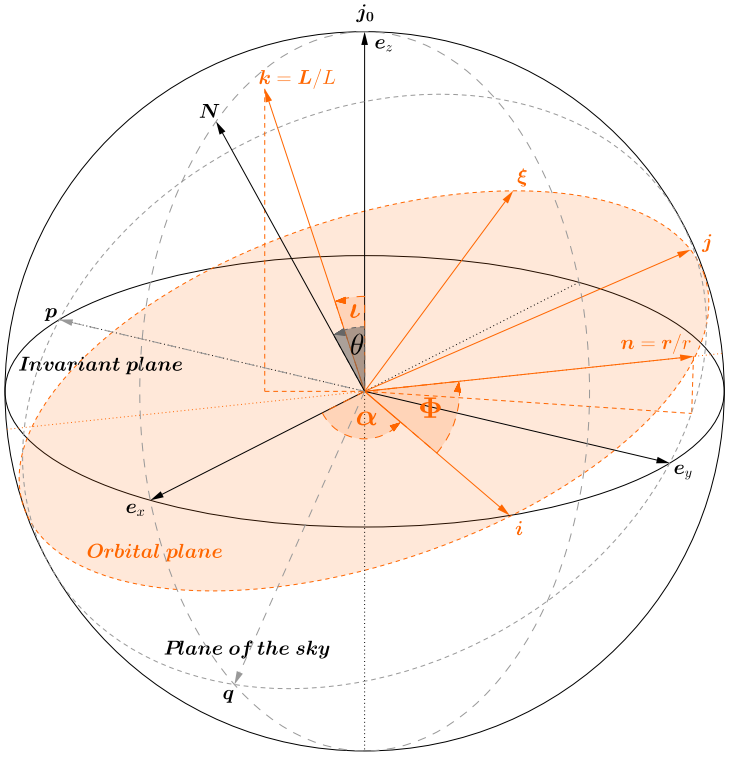

Figure 5.1: Various inertial and non-inertial coordinate systems that are useful to describe the dynamics of spinning compact binaries and associated GWs. The depicted vectors $(\boldsymbol{n}, \boldsymbol{\xi}, \boldsymbol{k})$ and $(\boldsymbol{i}, \boldsymbol{j}, \boldsymbol{k})$ define the two non-inertial frames, namely the co-moving and the orbital triads. The two inertial frames associated with $\boldsymbol{j}_0$ and $\boldsymbol{N}$ are also displayed, namely $(\boldsymbol{e}_x, \boldsymbol{e}_y, \boldsymbol{e}_z)$ and $(\boldsymbol{p}, \boldsymbol{q}, \boldsymbol{N})$. The orbital phase Φ of the binary requires us to invoke the two vectors $\boldsymbol{n}$ and $\boldsymbol{i}$ while the orientation of orbital angular momentum is specified by the two angles ι and α present in the $\boldsymbol{j}_0$ based inertial frame. The $(\boldsymbol{p}, \boldsymbol{q}, \boldsymbol{N})$ frame is essentially specified by the angle θ between $\boldsymbol{N}$ and $\boldsymbol{j}_0$. It should be noted that the orbital plane $(\boldsymbol{i}, \boldsymbol{j}, \boldsymbol{k})$ precesses around $\boldsymbol{j}_0$ due to spin-orbit coupling.

5.2 Waveforms for spinning compact binaries in hyperbolic orbits

We begin by listing the explicit expressions for the quadrupolar order GW polarization states for spinning compact binaries moving in non-circular orbits.

$$
\begin{aligned}
h_{+}|_{Q}(t) \;=\; & \frac{2\,G\,m\,\eta}{c^4\,R}\,\times \\
& \Big\{\big(\dot{r}^2-z\big)\Big[(\sin\alpha\cos\Phi+\cos\iota\cos\alpha\sin\Phi)^2-(C_\theta(\cos\Phi\cos\alpha-\sin\alpha\cos\iota\sin\Phi)-S_\theta\sin\iota\sin\Phi)^2\Big] \\
& +r^2\dot{\Phi}^2\Big[(\cos\alpha\cos\iota\cos\Phi-\sin\alpha\sin\Phi)^2-(C_\theta\sin\alpha\cos\iota\cos\Phi+C_\theta\cos\alpha\sin\Phi-S_\theta\sin\iota\cos\Phi)^2\Big] \\
& -r\dot{r}\dot{\Phi}\Big[\cos^2\alpha\cos\Phi\sin\Phi(\cos^2\iota+C_\theta^2)+\cos\alpha(\cos^2\Phi-\sin^2\Phi)\big(\cos\iota\sin\alpha(1+C_\theta^2)+C_\theta S_\theta\sin\iota\big) \\
& -\cos\Phi\sin\Phi\big((1+\cos^2\iota\,C_\theta^2)\sin^2\alpha+2C_\theta S_\theta\cos\iota\sin\alpha\sin\iota+\sin^2\iota S_\theta^2\big)\Big]\Big\}\,, \qquad (5.1)
\end{aligned}
$$

$$
\begin{aligned}
h_{\times}|_{Q}(t) \;=\; & \frac{4\,G\,m\,\eta}{c^4\,R}\,\times \\
& \Big\{\big(\dot{r}^2-z\big)\Big[(\sin\alpha\cos\Phi+\cos\iota\cos\alpha\sin\Phi)(C_\theta(\cos\Phi\cos\alpha-\sin\alpha\cos\iota\sin\Phi)-S_\theta\sin\iota\sin\Phi)\Big] \\
& -\;r^2\,\dot{\Phi}^2\Big[(\cos\iota\cos\Phi\cos\alpha-\sin\alpha\sin\Phi)(C_\theta(\cos\Phi\sin\alpha\cos\iota+\cos\alpha\sin\Phi)+S_\theta\sin\Phi\sin\iota)\Big] \\
& +\;r\,\dot{r}\,\dot{\Phi}\Big[\cos^2\alpha\cos\iota C_\theta(\sin^2\Phi-\cos^2\Phi)+\sin\alpha(\cos^2\Phi-\sin^2\Phi)(\cos\iota C_\theta\sin\alpha+\sin\iota S_\theta) \\
& +\;2\cos\alpha\cos\Phi\sin\Phi\,\big((1+\cos^2\iota)C_\theta\sin\alpha+\cos\iota\sin\iota S_\theta\big)\Big]\Big\}\,, \qquad (5.2)
\end{aligned}
$$

where R, S_θ and C_θ stand for the radial distance to the binary, $\sin\theta$ and $\cos\theta$, respectively, and $z = Gm/r$, where G denotes the gravitational constant. We would like to warn the reader that at few places the character z is also associated with the unit vector $\boldsymbol{z}$, the z-axis of our Cartesian coordinate system and the z-component of unit vectors like k_z, as commonly used in the literature. The angle θ provides the angle between the line of sight vector $\boldsymbol{N}$ and $\boldsymbol{j}_0$, the unit vector along the direction of the total angular momentum at the initial epoch (see Fig. 5.1). The above expressions are provided in an inertial frame where $\boldsymbol{j}_0$ points along the z-axis and where the dynamical angular variable Φ measures the orbital phase from the line of nodes that coincides with the unit vector $\boldsymbol{i}$ in a plane perpendicular to $\boldsymbol{L}$. Additionally, r and $\dot{r}$ denote the radial orbital separation and its time derivative, respectively, while $\dot{\Phi} = \mathrm{d}\Phi/\mathrm{d}t$. The angles ι and α specify the orientation of the orbital angular momentum $\boldsymbol{L}$ in the $\boldsymbol{j}_0$ based inertial frame. In particular, ι specifies the angle between the orbital angular momentum $\boldsymbol{L}$ and the z-axis of the inertial frame while α denotes the angle between the y axis and the projection of $\boldsymbol{L}$ onto the $x-y$ plane of the $\boldsymbol{j}_0$ based inertial frame. The notations m and η stand for $m = m_1 + m_2$ and $\eta = m_1 m_2/m^2$. In what follows, we sketch briefly how we obtained the above expressions for $h_{+}|_{Q}(t)$ and $h_{\times}|_{Q}(t)$.

It is customary to compute PN accurate expressions for GW polarization states from the fol-

lowing formulae that contain $h_{ij}^{\rm TT}$, the transverse–traceless part of the radiation field:

$$h_{+} = \frac{1}{2}\left(p_i p_j - q_i q_j\right) h_{ij}^{\rm TT}\,, \tag{5.3}$$

$$h_{\times} = \frac{1}{2}\left(p_i q_j + p_j q_i\right) h_{ij}^{\rm TT}\,, \tag{5.4}$$

where the vectors $\boldsymbol{p}$ and $\boldsymbol{q}$ form an orthonormal triad with the line–of–sight unit vector $\boldsymbol{N}$ such that $\boldsymbol{p} = \boldsymbol{N} \times \boldsymbol{j}_0$ and $\boldsymbol{q} = \boldsymbol{N} \times \boldsymbol{p}$ [66]. To compute the quadrupolar order GW polarization states, we require the expression for $h_{ij}^{\rm TT}$ that arises from the time varying Newtonian order quadrupole moment of the binary. The quadrupolar order contribution to $h_{ij}^{\rm TT}$ reads

$$h_{ij}^{\rm TT}\big|_{\rm Q} = \frac{4G\mu}{c^4 R}\mathscr{P}_{kmij}(\boldsymbol{N})\left(\mathrm{v}_{km} - \frac{Gm}{r}n_{km}\right)\,, \tag{5.5}$$

where $\mathscr{P}_{kmij}(\boldsymbol{N})$ is the transverse traceless projection operator projecting vectors onto the plane orthogonal to $\boldsymbol{N}$ and μ being the reduced mass ($\mu = m_1 m_2/m$). Additionally, v_{ij} and n_{ij} stand for $\mathrm{v}_i\mathrm{v}_j$ and $n_i n_j$, where n_i and v_i denote the components of $\boldsymbol{n} = \boldsymbol{r}/r$ and the velocity vector $\mathbf{v} = \mathrm{d}\boldsymbol{r}/\mathrm{d}t$. It should be noted that the dynamical variables appearing in Eqs. (5.1) and (5.2) follow 1.5PN-accurate orbital evolution though we use Newtonian order expression for h_{ij}^{TT}. This is influenced by the restricted PN waveforms for quasi-circular inspiral where the orbital frequency and phase follow PN-accurate evolution though the expressions for h_{+} and $h_{\times}$ arise from the quadrupolar order h_{ij}^{TT}. This leads to the following symbolic expressions for $h_{+}|_{Q}(t)$ and $h_{\times}|_{Q}(t)$

$$h_{+} = \frac{2G\mu}{c^4 R}\left\{(\boldsymbol{p}.\mathbf{v})^2 - (\boldsymbol{q}.\mathbf{v})^2 - z\left[(\boldsymbol{p}.\boldsymbol{n})^2 - (\boldsymbol{q}.\boldsymbol{n})^2\right]\right\}, \tag{5.6}$$

$$h_{\times} = \frac{4G\mu}{c^4 R}\left\{(\boldsymbol{p}.\mathbf{v})(\boldsymbol{q}.\mathbf{v}) - z\,(\boldsymbol{p}.\boldsymbol{n})(\boldsymbol{q}.\boldsymbol{n})\right\}\,. \tag{5.7}$$

It is convenient to evaluate the above dot products by expressing the vectors $\boldsymbol{n}, \mathbf{v}, \boldsymbol{p}, \boldsymbol{q}$ and $\boldsymbol{N}$ in a co-moving triad $(\boldsymbol{n}, \boldsymbol{\xi} = \boldsymbol{k} \times \boldsymbol{n}, \boldsymbol{k})$, where $\boldsymbol{k}$ is the unit vector along $\boldsymbol{L}$. It is easy to deduce that the components of these three unit vectors in the $\boldsymbol{j}_0$ based inertial frame are specified by the usual three Eulerian angles Φ, α and ι [67]. In our convention, the inertial frame components of $\boldsymbol{n}, \boldsymbol{\xi}$ and $\boldsymbol{k}$ are given by

$$\begin{aligned}\boldsymbol{n} = {} & (\cos\alpha\cos\Phi - \cos\iota\sin\alpha\sin\Phi)\,\boldsymbol{x} + \\ & (\sin\alpha\cos\Phi + \cos\iota\cos\alpha\sin\Phi)\,\boldsymbol{y} + (\sin\iota\sin\Phi)\,\boldsymbol{z}\,,\end{aligned} \tag{5.8}$$

$$\begin{aligned}\boldsymbol{\xi} = {} & (-\cos\alpha\sin\Phi - \sin\alpha\cos\iota\cos\Phi)\,\boldsymbol{x} + \\ & (\cos\iota\cos\Phi\cos\alpha - \sin\alpha\sin\Phi)\,\boldsymbol{y} + (\sin\iota\cos\Phi)\,\boldsymbol{z}\,,\end{aligned} \tag{5.9}$$

$$\boldsymbol{k} = \sin\alpha\sin\iota\,\boldsymbol{x} - \cos\alpha\sin\iota\,\boldsymbol{y} + \cos\iota\,\boldsymbol{z}\,. \tag{5.10}$$

Invoking three rotations that involve the above three Eulerian angles, it is straightforward to express the vectors that appear in Eqs. (5.6) and (5.7) in the $(\boldsymbol{n}, \boldsymbol{\xi}, \boldsymbol{k})$ co-moving triad. The

resulting expressions read

$$\boldsymbol{r} = r\boldsymbol{n} \,, \tag{5.11}$$

$$\mathbf{v} = \dot{r}\,\boldsymbol{n} + r\left(\frac{d\Phi}{dt} + \frac{d\alpha}{dt}\cos\iota\right)\boldsymbol{\xi} + r\left(\frac{d\iota}{dt}\sin\Phi - \sin\iota\cos\Phi\,\frac{d\alpha}{dt}\right)\boldsymbol{k} \,, \tag{5.12}$$

$$\begin{aligned}\boldsymbol{p} = {} & (-\sin\alpha\cos\Phi - \cos\iota\cos\alpha\sin\Phi)\,\boldsymbol{n} \\ & + (\sin\alpha\sin\Phi - \cos\iota\cos\alpha\cos\Phi)\,\boldsymbol{\xi} + \cos\alpha\sin\iota\,\boldsymbol{k} \,,\end{aligned} \tag{5.13}$$

$$\begin{aligned}\boldsymbol{q} = {} & (\cos\alpha\cos\Phi\cos\theta - \cos\iota\sin\alpha\sin\Phi\cos\theta - \sin\iota\sin\Phi\sin\theta)\,\boldsymbol{n} \\ & - (\cos\alpha\sin\Phi\cos\theta + \sin\alpha\cos\iota\cos\Phi\cos\theta + \sin\iota\cos\Phi\sin\theta)\,\boldsymbol{\xi} \\ & + (\sin\alpha\sin\iota\cos\theta - \cos\iota\sin\theta)\,\boldsymbol{k} \,,\end{aligned} \tag{5.14}$$

$$\begin{aligned}\boldsymbol{N} = {} & (\cos\alpha\cos\Phi\sin\theta - \cos\iota\sin\alpha\sin\Phi\sin\theta + \sin\iota\sin\Phi\cos\theta)\,\boldsymbol{n} \\ & - (\cos\alpha\sin\Phi\sin\theta + \sin\alpha\cos\iota\cos\Phi\sin\theta - \sin\iota\cos\Phi\cos\theta)\,\boldsymbol{\xi} \\ & + (\sin\alpha\sin\iota\sin\theta + \cos\iota\cos\theta)\,\boldsymbol{k} \,.\end{aligned} \tag{5.15}$$

To obtain the above expressions, we invoked the definitions for $\boldsymbol{p}$, $\boldsymbol{q}$ and let $\boldsymbol{j}_0$, $\boldsymbol{N}$ have the following components in the inertial frame: $\boldsymbol{j}_0 = (0,0,1)$ and $\boldsymbol{N} = (\sin\theta, 0, \cos\theta)$. It is not difficult to verify that an explicit evaluation of Eqs. (5.6) and (5.7) for $h_+|_Q(t)$ and $h_\times|_Q(t)$ while employing the above expressions for $\boldsymbol{n}, \mathbf{v}, \boldsymbol{p}, \boldsymbol{q}$ and $\boldsymbol{N}$ results in Eqs. (5.1) and (5.2).

We obtain temporally evolving $h_+|_Q(t)$ and $h_\times|_Q(t)$ for spinning compact binaries in hyperbolic orbits by specifying how $r, \dot{r}, \iota, \alpha, \Phi$ and $\dot{\Phi}$ evolve in time along PN accurate hyperbolic orbits. The radial part of the dynamics is tackled in a parametric manner invoking v, a real variable along the orbit, the time eccentricity $e_{\rm t}$ and the mean motion $\bar{n}$ associated with PN accurate hyperbolic orbits of Ref. [51]. The 1.5PN accurate parametric expressions for r and $\dot{r}$, adapted from Ref. [68], read

$$r = \frac{Gm}{c^2}\frac{1}{\bar{\xi}^{2/3}}\left\{e_{\rm t}\cosh v - 1 - \bar{\xi}^{2/3}\,\frac{e_{\rm t}\cosh v\,(6-7\eta) + 18 - 2\eta}{6} + \bar{\xi}\,\frac{\Sigma}{\sqrt{e_{\rm t}^2-1}}\right\}, \tag{5.16}$$

$$\dot{r} = \bar{\xi}^{1/3}\frac{c\,e_{\rm t}\sinh v}{e_{\rm t}\cosh v - 1}\left\{1 - \bar{\xi}^{2/3}\,\frac{6-7\eta}{6}\right\}, \tag{5.17}$$

where $\bar{\xi} = Gm\bar{n}/c^3$ and Σ terms are due to the spin-orbit interactions. The expression for Σ is defined as

$$\Sigma = \delta_1\chi_1 q\,(\boldsymbol{k}\cdot\boldsymbol{s}_1) + \frac{\delta_2\chi_2}{q}\,(\boldsymbol{k}\cdot\boldsymbol{s}_2) \,, \tag{5.18}$$

where $\delta_1 = \eta/2 + 3/4(1-\sqrt{1-4\eta})$, and $\delta_2 = \eta/2 + 3/4(1+\sqrt{1-4\eta})$ while $q = m_1/m_2$ with $m_1 \geq m_2$. The dot products define the misalignments between $\boldsymbol{L}$ and the two spins $\boldsymbol{S}_1$ and $\boldsymbol{S}_2$ while $\chi_{1,2}$ stand for the two Kerr parameters such that $\boldsymbol{S}_1 = G\,m_1^2\,\chi_1\,\boldsymbol{s}_1/c$ and $\boldsymbol{S}_2 = G\,m_2^2\,\chi_2\,\boldsymbol{s}_2/c$. The temporal evolution for r and $\dot{r}$ are obtained by solving the following hyperbolic version of the classical Kepler Equation

$$\bar{n}\,(t - t_0) = e_{\rm t}\sinh v - v \,, \tag{5.19}$$

where t_0 is certain initial epoch. In the present investigation, we invoke an accurate and efficient numerical procedure, namely Mikkola's approach [65], to obtain $v(t)$ from the above transcendental equation.

Let us note that the above three equations, namely Eqs. (5.16), (5.17) and (5.19), are adapted from Ref. [68] that obtained Keplerian type parametric solution to the radial sector of spinning compact binary dynamics in eccentric orbits. We begin by listing relevant equations that describe the above mentioned 1.5PN accurate Keplerian type parametric solution:

$$r = a_{\rm r}\,(1 - e_{\rm r}\cos u)\,, \tag{5.20}$$
$$l = n\,(t - t_0) = u - e_{\rm t}\sin u\,, \tag{5.21}$$

where u and l stand for the eccentric and mean anomalies. In what follows, we employ l to explore various aspects of our time domain GW polarization states as l essentially represents the scaled coordinate time. The orbital parameters $a_{\rm r}$ and n are the PN extensions of the semi-major axis and the mean motion associated with the Keplerian parametric solution to the Newtonian orbital dynamics. Additionally, the radial part of the PN accurate Keplerian type parameterization involves two eccentricities, namely $e_{\rm r}$ and $e_{\rm t}$ [51]. These orbital elements are explicit functions of the reduced orbital energy E, reduced angular momentum L, the symmetric mass ratio η, the two Kerr parameters and the spin-orbit misalignments. To 1.5PN order, these parameters are given by

$$a_{\rm r} = \frac{Gm}{-2E}\left\{1 - \frac{2E}{4c^2}(\eta - 7) - \frac{2E}{c^3}\frac{Gm\,\Sigma}{L}\right\}, \tag{5.22}$$
$$e_{\rm t}^2 = 1 + \frac{2EL^2}{G^2m^2} - \frac{2E}{c^2}\left(2\eta - 2 + \frac{2EL^2}{G^2m^2}\frac{7\eta - 17}{4}\right) + \frac{4E}{c^3}\frac{Gm\,\Sigma}{L}\,, \tag{5.23}$$
$$e_{\rm r}^2 = 1 + \frac{2EL^2}{G^2m^2} - \frac{2E}{c^2}\left(6 - \eta + \frac{2EL^2}{G^2m^2}\frac{15 - 5\eta}{4}\right) + \frac{8E}{c^3}\frac{Gm\,\Sigma}{L}\left(1 + \frac{EL^2}{G^2m^2}\right), \tag{5.24}$$
$$\xi = \left(\frac{-2E}{c^2}\right)^{3/2}\left\{1 - \frac{2E}{c^2}(\eta - 15)\frac{1}{8}\right\}\,, \tag{5.25}$$

where ξ stands for Gmn/c^3. The structure of the two eccentricities indicate that it should be possible to express $e_{\rm r}$ in terms of $e_{\rm t}$ as a PN series employing ξ and the spin parameters (this holds true for $a_{\rm r}$). The resulting expressions for $e_{\rm r}$ and $a_{\rm r}$ read

$$e_{\rm r} = e_{\rm t}\left\{1 + \xi^{2/3}\,\frac{8 - 3\eta}{2} - \xi\,\frac{\Sigma}{\sqrt{1 - e_{\rm t}^2}}\right\}, \tag{5.26}$$
$$a_{\rm r} = \frac{Gm}{c^2}\frac{1}{\xi^{2/3}}\left\{1 - \xi^{2/3}\frac{9 - \eta}{3} + \xi\frac{\Sigma}{\sqrt{1 - e_{\rm t}^2}}\right\}. \tag{5.27}$$

The 1.5PN accurate expressions for r and $\dot r$ in terms of $\bar n$, $e_{\rm t}$ and v are obtained with the help of the following steps. First, we obtain explicit 1.5PN accurate expression for $r = a_{\rm r}(1 - e_{\rm r}\cos u)$ in terms of n, $e_{\rm t}$ and u with the help of Eqs. (5.26) and (5.27). This leads to

$$r = \frac{Gm}{c^2}\frac{1}{\xi^{2/3}}\left\{1 - e_{\rm t}\cos u - \frac{\xi^{2/3}}{6}\left(18 - 2\eta + (6 - 7\eta)\,e_{\rm t}\cos u\right) + \xi\,\frac{\Sigma}{\sqrt{1 - e_{\rm t}^2}}\right\}. \tag{5.28}$$

To obtain its hyperbolic counterpart, we let $u = \imath\, v$ and $n = -\imath\,\bar n$, where $\imath = \sqrt{-1}$, by invoking the arguments in Ref. [51]. This analytic continuation in E from $E < 0$ to $E > 0$ essentially works as all orbital parameters that are analytic near $E = 0$. We employ similar arguments to obtain $\dot r(v, \bar n, e_{\rm t})$, given by Eq. (5.17), from its eccentric version computed in terms of u, n and $e_{\rm t}$.

With the help of the above arguments and Ref. [68], we extract the following 1.5PN accurate $\dot{\Phi}$ expression for spinning compact binaries in hyperbolic orbits

$$\dot{\Phi} = \frac{\bar{n}\sqrt{e_{\rm t}^2-1}}{(e_{\rm t}\cosh\nu-1)^2}\Bigg\{1+\bar{\xi}^{2/3}\left(\frac{4-\eta}{e_{\rm t}\cosh\nu-1}+\frac{\eta-1}{e_{\rm t}^2-1}\right) - \bar{\xi}\,\frac{\Sigma}{\sqrt{e_{\rm t}^2-1}}\left(\frac{1}{e_{\rm t}\cosh\nu-1}+\frac{1}{e_{\rm t}^2-1}\right)\Bigg\} - \cos\iota\,\dot{\alpha}\,, \tag{5.29}$$

where the differential equation for α arises from the precessional equation for $\boldsymbol{k}$. The above differential equation for Φ is also adapted from its eccentric counterpart, given by Eq. (B2) in Ref. [68]. To derive Eq. (B2) in [68], one starts from the expression for $\mathbf{v}$ in the co-moving triad $(\boldsymbol{n},\boldsymbol{\xi},\boldsymbol{k})$ as given by Eq. (5.12). This leads to the following 1.5PN accurate expression for $\mathbf{v}\cdot\mathbf{v}$, namely

$$\mathrm{v}^2 = \dot{r}^2 + r^2(\dot{\Phi}^2 + 2\dot{\Phi}\dot{\alpha}\cos\iota)\,, \tag{5.30}$$

where we have neglected the $\mathcal{O}(1/c^6)$ order $\dot{\alpha}^2$, i^2 and $\dot{\alpha}i$ terms. The next step is based on the fact that the square of the orbital velocity, extractable from the fully 1.5PN order Hamiltonian or orbital energy, does not contain any spin dependent terms. This is attributable to the employed gauge and the spin supplementary condition in Ref. [68]. This is why one obtains Newtonian order relation, namely $\mathrm{v}^2 = 2E + 2Gm/r$, while computing v^2 from a Hamiltonian that only contains Newtonian and 1.5PN order spin-orbit contributions. This statement may be verified by inspecting the Eqs. (1), (5), (10) and (39) of [68]. Therefore, the v^2 expression that arise from a fully 1.5PN accurate orbital energy for spinning binaries in general orbits will not explicitly contain any spin-orbit contributions similar to the parametric equation for $\dot{r}$, given by Eq. (5.17). The PN-accurate expression for v^2 is given by

$$\mathrm{v}^2 = 2E + 2\frac{Gm}{r} + \frac{1}{c^2}\left\{(9\,\eta-3)\,E^2 + \frac{Gm}{r}(14\eta-12)E + \frac{G^2m^2}{r^2}(5\eta-10) + \frac{Gm\eta}{r^3}L^2\right\}, \tag{5.31}$$

The expression for $\dot{\Phi}^2$ follows by equating the above two expressions for v^2. This leads to PN accurate expression for $\dot{\Phi}$, as given by Eq. (B2) in [68], where the spin-orbit contributions arise from the PN accurate expression for r. We obtain our Eq. (5.29) for $\dot{\Phi}$ with the help of earlier mentioned analytic continuation after expressing $(-2E)$ and L in terms of n, e_t and u. For easy visualization, it is convenient to characterize our hyperbolic binaries in terms of an impact parameter b such that $b\,\mathrm{v}_\infty = |\boldsymbol{r}\times\mathbf{v}|$ when $|\boldsymbol{r}|\to\infty$ and where v_∞ stands for the relative velocity at infinity. We characterize our hyperbolic binaries using the following 1PN accurate expression for b in terms of $\bar{\xi}$ and e_t

$$b = \frac{Gm}{c^2}\frac{\sqrt{e_{\rm t}^2-1}}{\bar{\xi}^{2/3}}\left\{1-\bar{\xi}^{2/3}\left(\frac{\eta-1}{e_{\rm t}^2-1}+\frac{7\eta-6}{6}\right)\right\}. \tag{5.32}$$

The temporal evolution for α and ι, as expected, requires us to solve the precessional equation for $\boldsymbol{k}$ in the $\boldsymbol{j_0}$ based inertial frame and this is clearly due to the Eq. (5.10) for $\boldsymbol{k}$. In practice, we numerically solve coupled precessional equations for $\boldsymbol{s_1}, \boldsymbol{s_2}$ and $\boldsymbol{k}$ as the differential equation for $\boldsymbol{k}$ arises from the relation $\dot{\boldsymbol{k}} = -(S_1\,\dot{\boldsymbol{s}}_1 + S_2\,\dot{\boldsymbol{s}}_2)/L$. This equation, as expected, arises from the conservation of the total angular momentum and the magnitude of the orbital angular momentum during the precessional timescale. The relevant equations that incorporate the

dominant order spin-orbit coupling for binaries in hyperbolic orbits are given by

$$\dot{\boldsymbol{s}_1} = \frac{c^3}{Gm}\frac{\bar{\xi}^{5/3}\sqrt{e_t^2-1}}{(e_t\cosh\nu-1)^3}\,\delta_1\,\boldsymbol{k}\times\boldsymbol{s}_1\,, \tag{5.33}$$

$$\dot{\boldsymbol{s}_2} = \frac{c^3}{Gm}\frac{\bar{\xi}^{5/3}\sqrt{e_t^2-1}}{(e_t\cosh\nu-1)^3}\,\delta_2\,\boldsymbol{k}\times\boldsymbol{s}_2\,, \tag{5.34}$$

$$\dot{\boldsymbol{k}} = \frac{c^3}{Gm}\frac{\bar{\xi}^{2}\,(\delta_1\chi_1 q\,\boldsymbol{s}_1+\delta_2\chi_2/q\,\boldsymbol{s}_2)\times\boldsymbol{k}}{(e_t\cosh\nu-1)^3}\,. \tag{5.35}$$

The expressions for $\dot{\boldsymbol{s}_1}$ and $\dot{\boldsymbol{s}_2}$ are adapted from Ref. [60] while invoking the Newtonian accurate L for hyperbolic orbits and the Newtonian version of our Eqs. (5.16) and (5.17) for r. Additionally, we employ the following expression for $\dot{\alpha}$ that appear in the differential equation for Φ. This equation arises from the Cartesian components of $\boldsymbol{k}$ in the $\boldsymbol{j_0}$ based inertial frame and Eq. (5.35) for $\dot{\boldsymbol{k}}$:

$$\dot{\alpha} = \frac{k_x\dot{k}_y - k_y\dot{k}_x}{k_x^2+k_y^2}\,. \tag{5.36}$$

It is possible to incorporate numerically the effects of GW emission during the hyperbolic encounter. This is achieved by solving the following 2.5PN order coupled differential equations for $\bar{n}$ and e_t:

$$\frac{d\bar{n}}{dt} = -\frac{c^6}{G^2m^2}\frac{\bar{\xi}^{11/3}\,8\,\eta}{5\,\beta^7}\left[-49\beta^2-32\beta^3+35(e_t^2-1)\beta-6\beta^4+9e_t^2\beta^2\right], \tag{5.37}$$

$$\frac{de_t}{dt} = -\frac{c^3}{Gm}\frac{\bar{\xi}^{8/3}\,8\,\eta\,(e_t^2-1)}{15\,\beta^7\,e_t}\left[-49\beta^2-17\beta^3+35(e_t^2-1)\beta-3\beta^4+9e_t^2\beta^2\right], \tag{5.38}$$

where, for simplicity, we write $\beta = e_t\cosh\nu - 1$. The derivation of the above two differential equations is adapted from Eqs. (63) in Ref. [69] and requires 2.5PN contributions to the relative acceleration.

We are now in a position to obtain $h_+|_Q(t)$ and $h_\times|_Q(t)$ for spinning compact binaries moving in hyperbolic orbits influenced by GW emission. The idea is to numerically obtain the temporal evolution for $r, \dot{r}, \Phi, \dot{\Phi}, \iota, \alpha, \bar{n}$ and e_t and impose these variations in the expression for $h_+|_Q(t)$ and $h_\times|_Q(t)$, given by Eqs. (5.1) and (5.2). We begin by specifying the initial binary configuration in terms of $m_1, m_2, \chi_1, \chi_2, \bar{n}$ and e_t. It is possible to specify the initial orientations of $\boldsymbol{s_1}, \boldsymbol{s_2}$ and $\boldsymbol{k}$ in the $\boldsymbol{j_0}$ based inertial frame by freely choosing four angles (θ_1^i, θ_2^i) and (ϕ_1^i, ϕ_2^i). These four angles provide the six Cartesian components of $\boldsymbol{s_1}$ and $\boldsymbol{s_2}$ at the initial epoch and, in general, these components are

$$\boldsymbol{s_1} = (\sin\theta_1\cos\phi_1, \sin\theta_1\sin\phi_1, \cos\theta_1)\,, \tag{5.39}$$

$$\boldsymbol{s_2} = (\sin\theta_2\cos\phi_2, \sin\theta_2\sin\phi_2, \cos\theta_2)\,. \tag{5.40}$$

The values of ι and α that specify the initial orientation of $\boldsymbol{k}$ are not freely chosen. These initial estimates are obtained by noting that the initial x and y components of $\boldsymbol{j}$ should be zero as we let $\boldsymbol{j}$ to point along the z-axis at the initial epoch. This leads to the following expressions

for k_x and k_y at $t = 0$

$$k_x|_{t=0} = \bar{\xi}_0^{1/3} \frac{X_1^2 \chi_1 \sin\theta_1^i \cos\phi_1^i + X_2^2 \chi_2 \sin\theta_2^i \cos\phi_2^i}{\eta \sqrt{e_{\rm t}^2 - 1}} \,, \tag{5.41}$$

$$k_y|_{t=0} = \bar{\xi}_0^{1/3} \frac{X_1^2 \chi_1 \sin\theta_1^i \sin\phi_1^i + X_2^2 \chi_2 \sin\theta_2^i \sin\phi_2^i}{\eta \sqrt{e_{\rm t}^2 - 1}} \,, \tag{5.42}$$

where $X_1 = m_1/m$ and $X_2 = m_2/m$ while $\bar{\xi}_0$ denotes the initial value for $\bar{\xi}$. The initial estimates for ι and α is obtained by equating the above expressions to $\sin\alpha \sin\iota$ and $-\cos\alpha \sin\iota$. However, we usually extract values of α and ι during the numerical interaction with the help of the three Cartesian components of $\boldsymbol{k}$, namely $\alpha = -\tan^{-1}(k_x/k_y)$ and $\iota = \cos^{-1}(k_z)$. We impose the phasing angle Φ to vanish at periastron time, i.e. $\Phi(0) = 0$.

We begin the numerical implementation of $h_+|_Q(t)$ and $h_\times|_Q(t)$ by obtaining $v(t)$ and this involves solving Eq. (5.19) via the Mikkola's method. The resulting $v(t)$ is imposed on Eqs. (5.16) and (5.17) for $r(v)$ and $\dot{r}(v)$ to obtain 1.5PN accurate $r(t)$ and $\dot{r}(t)$ for our hyperbolic binary configuration. The next step involves numerically integrating simultaneously the above listed differential equations for $\boldsymbol{s_1}, \boldsymbol{s_2}, \boldsymbol{k}, \Phi, \bar{n}$ and $e_{\rm t}$. This is achieved by invoking twelve differential equations that include differential equations for the nine Cartesian components of $\boldsymbol{s_1}, \boldsymbol{s_2}$ and $\boldsymbol{k}$ in the $\boldsymbol{j_0}$ based inertial frame. In practice, we use the mean anomaly l rather than the coordinate time t while numerically tackling these differential equations and the transcendental equation (5.19). The change of variable is performed by noting that $\mathrm{d}l = \bar{n}\,\mathrm{d}t$. In what follows, we display $h_+|_Q(l)$ and $h_\times|_Q(l)$ resulting from such an implementation and explore various features.

In Figs. 5.2 and 5.3, we display $h_+|_Q(l)$ and $h_\times|_Q(l)$ for $q = 1$ and $q = 4$ binaries having three different orbital eccentricities. We observe that both polarization states exhibit the memory effect. It is due to this 'linear' memory effect that GW amplitudes at $t = +\infty$ are different from their respective $t = -\infty$ values, depicted by the dashed lines. The amplitude of the effect decreases as the orbital eccentricity approaches unity. However, the time-domain waveforms develop sharply varying features compared to their higher orbital eccentricity counterparts. This feature is mass ratio dependent and clearly visible for comparable mass binaries. For a given $e_{\rm t}$ and $\bar{n}$, the amplitude of the memory effect is larger for $h_\times|_Q(l)$ compared to its 'plus' counterpart. Note that the memory effect is absent in $h_+|_Q(l)$ for non-spinning binaries as evident from figures in Ref. [50,63]. In Fig. 5.4, we probe the influence of the initial orientation of the dominant spin on the memory effect for $q = 4$ unequal mass binaries. The memory amplitude decreases as we vary the initial misalignment of $\boldsymbol{s}_1$ from $\boldsymbol{j}_0$ for $e_{\rm t}$ values closer to unity. The variations in the memory amplitude is more prominent for the $h_+|_Q(l)$ plots for higher $e_{\rm t}$ values. This may be attributed to the more pronounced orbital precession for higher θ_1^i values and the presence of non-negligible $\sqrt{e_{\rm t}^2 - 1}$ contribution in the differential equations for the two spins, as evident from Eqs. (5.33)-(5.35). It will be interesting to probe any possible data analysis implications of the varying memory amplitudes as depicted in Fig. 5.4. We have also verified that the memory effect persists even if we switch off the effects of GW damping. In fact, the plots for $h_+|_Q(l)$ and $h_\times|_Q(l)$ are essentially identical to those displayed in Figs. 5.2, 5.3 and 5.4 while neglecting the effects of GW damping, provided by Eqs. (5.37) and (5.38). In Appendix A, we provide formulae for computing 1PN order amplitude corrected GW polarization states for spinning binaries in a compact way. The expressions, given by Eqs. (5.75) and (5.76), are obtained with the help of Eqs. (5.2) while using fully 1PN accurate expression for the transverse–traceless part of the radiation field $h_{ij}^{\rm TT}$. The 1PN accurate expression for $h_{ij}^{\rm TT}$ incorporates contributions from appropriate time derivatives of various mass type and

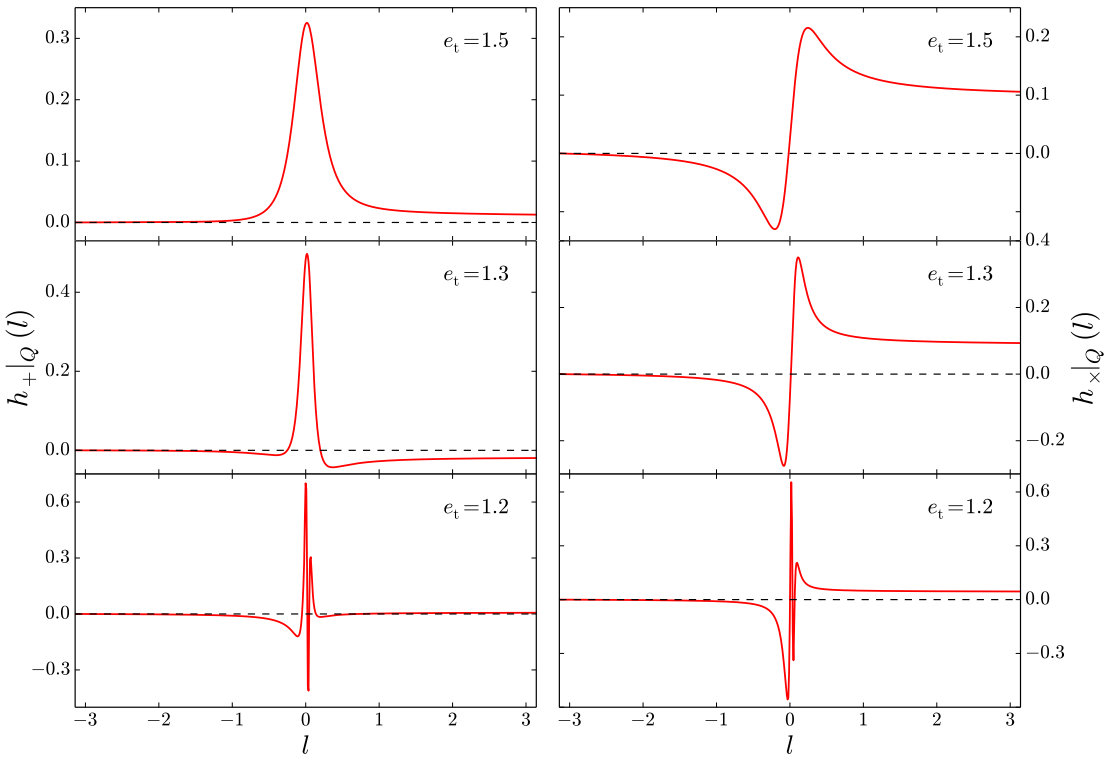

Figure 5.2: The scaled $h_+|_Q(l)$ and $h_\times|_Q(l)$ plots for $m = 20\,M_\odot, q = 1$ spinning compact binaries containing maximally spinning BHs. The employed scale factor in the present and the next two figures is Gm/c^2R. We let e_t take three values while choosing $b \sim 30\ Gm/c^2$. The initial spin orientations in the $\boldsymbol{j}_0$ based inertial frame are $\theta_1^i = 30°$, $\theta_2^i = 30°$, $\phi_1^i = 30°$, $\phi_2^i = 120°$ and we let $\theta = 45°$. The conservative orbital evolution is fully 1.5PN accurate and the influences of GW emission are taken into account at leading order. The linear memory effect causes the solid line waveform plots to depart from the dashed line after the hyperbolic passage.

current type multipole moments of the binary and are adapted from Eqs. (3.22) in Ref. [61]. Specifically, 1PN-accurate expression for $h_{ij}^{\rm TT}$ requires us to compute time derivatives of mass and current quadrupoles and octupoles of the binary and fourth time derivative of $\mathscr{I}^{ijkl}$ which is given by the symmetric and trace free part of $\mu(1-3\,\eta)\,x^{ijkl}$. We do not provide the explicit 1PN accurate amplitude contributions to $h_+(l)$ and $h_\times(l)$ in terms of $\dot{r}, z, r\,\dot{\Phi}$ and trigonometric functions of ι, α and Φ as done in Eqs. (5.1) and (5.2). The very lengthy nature of such expressions is the main reason why we did not expand the squares and products appearing in Eqs. (5.75) and (5.76) with the help of various dot products, given by Eqs. (5.77)-(5.82). It is fairly straightforward to obtain plots for the 0.5PN and 1PN contributions to $h_+(l)$ and $h_\times(l)$, similar to our plots for $h_+|_Q(l)$ and $h_\times|_Q(l)$. This is also not pursued as these PN contributions, as expected, are substantially smaller in magnitude compared to the quadrupolar order waveforms. Additionally, the plots for such PN contributions are qualitatively similar to plots for $h_+|_Q(l)$ and $h_\times|_Q(l)$ as these contributions also exhibit the linear memory effect.

In what follows, we provide an explanation for the presence of the linear memory effect in both the polarization states for spinning compact binaries in hyperbolic orbits. This explanation becomes clearer and easier while considering non-spinning compact binaries in hyperbolic orbits. In the next section, we consider temporally evolving GW polarization states associated with non-spinning compact binaries in 1PN accurate hyperbolic orbits invoking our Keplerian type parametric solution. This should also allow us to compare our 1PN accurate $h_+(l)$ and $h_\times(l)$

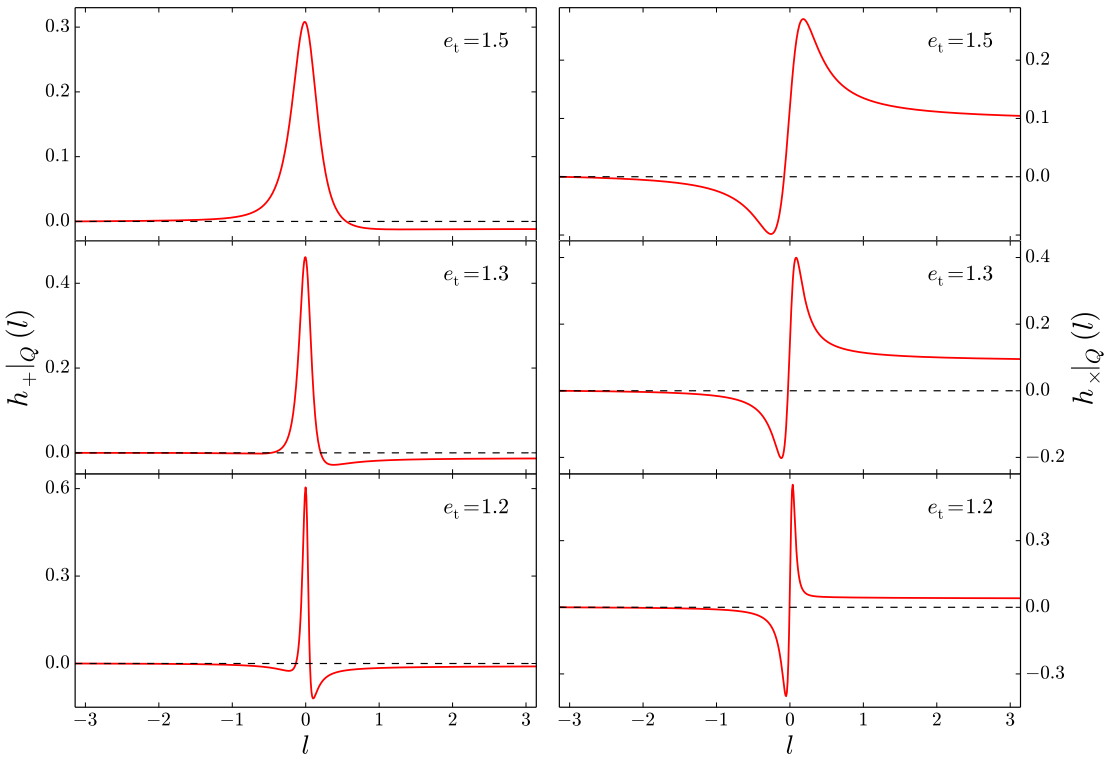

Figure 5.3: The scaled $h_+|_Q(l)$ and $h_\times|_Q(l)$ plots for $m = 20\,M_\odot, q = 4$ spinning compact binaries containing maximally spinning BHs. The other specifications are same as in Fig. 5.2. The amplitude of the memory effect is rather insensitive to the mass ratio. However, the sharply varying features with multiple peaks, present in $e_t = 1.2$ plots of Fig. 5.2, are not visible.

with those obtained via the generalized true anomaly parameterization, detailed in Ref. [52].

5.3 1PN accurate Gravitational wave phasing for non-spinning compact binaries in hyperbolic orbits

We begin by constructing quadrupolar order GW polarization states, namely $h_+|_Q(l)$ and $h_\times|_Q(l)$, associated with non-spinning compact binaries moving in 1PN accurate hyperbolic orbits. It is not very difficult to infer that Eqs. (5.6) and (5.7) that provide $h_+|_Q(l)$ and $h_\times|_Q(l)$ in terms of various dot products involving $\boldsymbol{p}, \boldsymbol{q}, \boldsymbol{n}, \mathbf{v}$ and z also apply for non-spinning compact binaries. Therefore, the explicit expressions for the quadrupolar order GW polarization states in terms of the relevant dynamical variables are again obtained by evaluating the dot products appearing in Eqs. (5.6) and (5.7). It is natural to invoke an inertial frame associated with $\boldsymbol{L}$ to describe the orbital dynamics of non-spinning compact binaries. This is because $\boldsymbol{L}$ is conserved both in magnitude and direction for non-spinning compact binaries. Furthermore, it is convenient to introduce polar coordinates (r, ϕ) in a plane perpendicular to $\boldsymbol{L}$ as the orbital motion takes place in such a plane. This allows us to describe $\boldsymbol{r}$ and $\mathbf{v}$ in terms of r, ϕ and their time derivatives in the $\boldsymbol{L}$ based inertial triad. However, it is customary to evaluate the dot products appearing in Eqs. (5.6) and (5.7) by expressing $\boldsymbol{r}$ and $\mathbf{v}$ in an $\boldsymbol{N}$ based inertial frame $(\boldsymbol{p}, \boldsymbol{q}, \boldsymbol{N})$. This is achieved by noting that the angle θ between $\boldsymbol{N}$ and $\boldsymbol{k}$, namely the orbital inclination, remains a constant for non-spinning compact binaries. This leads to the

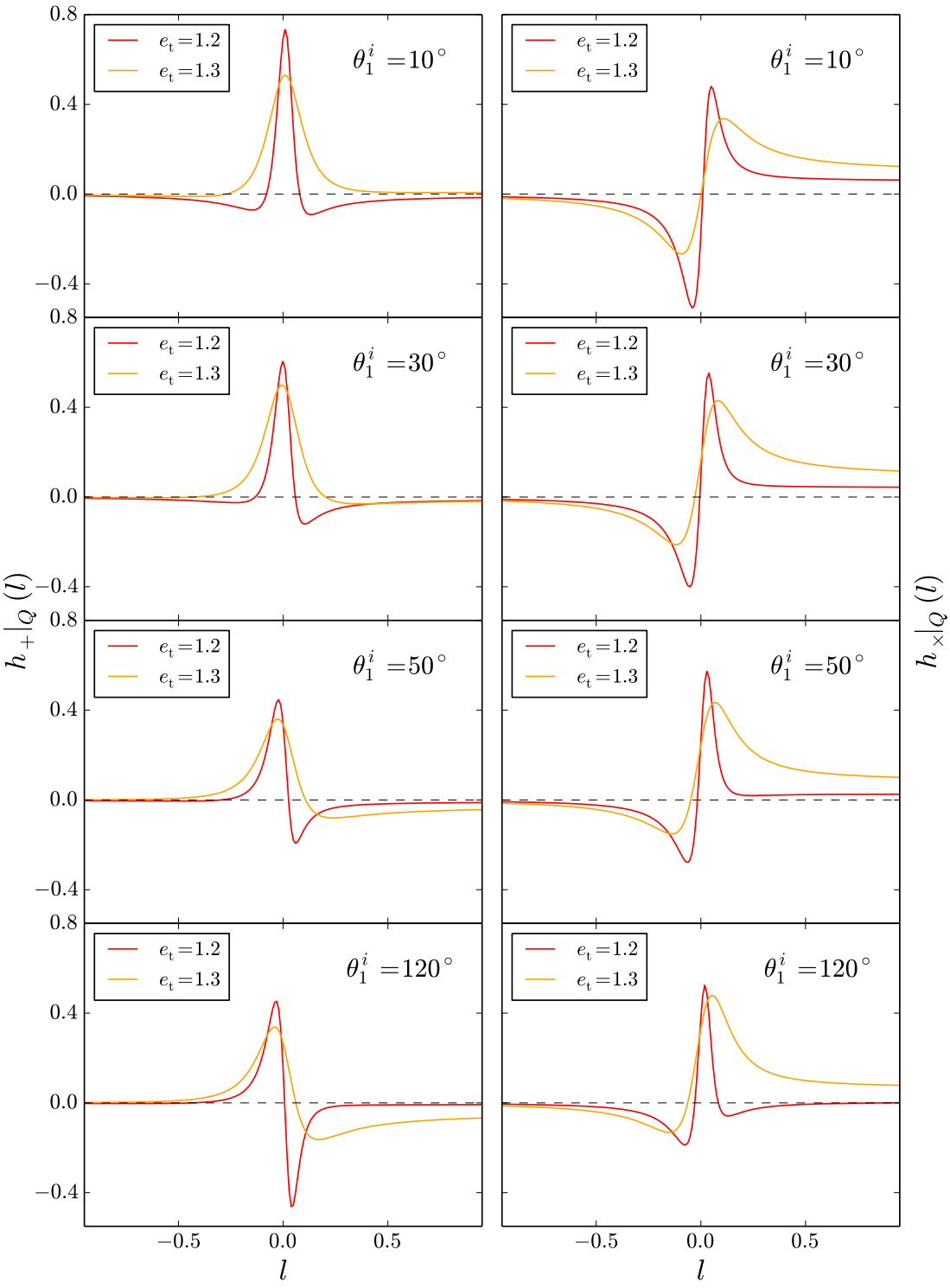

Figure 5.4: We plot the scaled $h_+|_Q(l)$ and $h_\times|_Q(l)$ for $m = 20\,M_\odot, q = 4$ spinning compact binaries containing maximally spinning BHs while varying the initial orientation of the dominant spin for two e_t values. The orbital dynamics is fully 1.5PN accurate while other parameters are similar to those used in Fig. 5.3. The impact of the initial misalignment between $\boldsymbol{s}_1$ and $\boldsymbol{j}_0$ on the memory is more prominent on $h_+|_Q(l)$ for higher e_t values.

following expressions for $\boldsymbol{r}$ and $\mathbf{v}$ in the $(\boldsymbol{p},\boldsymbol{q},\boldsymbol{N})$ frame.

$$\boldsymbol{n} = -\boldsymbol{p}\sin\phi + (\boldsymbol{q}\cos\theta + \boldsymbol{N}\sin\theta)\cos\phi \ , \tag{5.43}$$

$$\mathbf{v} = \boldsymbol{p}\left(-\dot{r}\sin\phi - r\dot{\phi}\cos\phi\right) + (\boldsymbol{q}\cos\theta + \boldsymbol{N}\sin\theta)\left(\dot{r}\cos\phi - r\dot{\phi}\sin\phi\right) \ . \tag{5.44}$$

The above expressions allow us to compute the dot products appearing in the Eqs. (5.6) and (5.7) for $h_+|_{\rm Q}(l)$ and $h_\times|_{\rm Q}(l)$, in a straightforward manner. The resulting GW polarization states read

$$h_+|_{\rm Q} = \frac{G\mu}{c^4 R} \times \left\{ \left(1+C_\theta^2\right)\left[\left(z + r^2\dot{\phi}^2 - \dot{r}^2\right)\cos 2\phi + 2r\dot{r}\dot{\phi}\sin 2\phi \right] - S_\theta^2\left(z - r^2\dot{\phi}^2 - \dot{r}^2\right) \right\} , \tag{5.45}$$

$$h_\times|_{\rm Q} = \frac{G\mu}{c^4 R} \times \left\{ 2C_\theta\left(z + r^2\dot{\phi}^2 - \dot{r}^2\right)\sin 2\phi - 2C_\theta 2r\dot{r}\dot{\phi}\cos 2\phi \right\} , \tag{5.46}$$

where $\dot{\phi} = {\rm d}\phi/{\rm d}t$.
It should be obvious that we need to describe how $r, \dot{r}, \phi$ and $\dot{\phi}$ evolve in time for non-spinning compact binaries moving in hyperbolic orbits to obtain the associated $h_+|_{\rm Q}(t)$ and $h_\times|_{\rm Q}(t)$. This is implemented in a parametric manner invoking the 1PN accurate quasi-Keplerian parameterization of Ref. [51]. The radial and angular parts of the orbital dynamics are parametrically given by

$$r = a_{\rm r}(e_{\rm r}\cosh v - 1) \ , \tag{5.47}$$

$$\phi - \phi_0 = 2K\arctan\left[\left(\frac{e_\phi+1}{e_\phi-1}\right)^{1/2}\tanh v/2\right] . \tag{5.48}$$

The temporal evolution for r and ϕ are provided numerically by tackling the 1PN accurate Kepler equation

$$l = \bar{n}(t-t_0) = e_{\rm t}\sinh v - v. \tag{5.49}$$

The additional orbital parameters K and e_ϕ that appear in the angular part of the parametric solution are the hyperbolic versions of the periastron advance constant and angular eccentricity associated with the eccentric orbits [51]. All the orbital elements, as expected, are PN accurate functions of conserved orbital energy and angular momentum. The 1PN accurate expressions for these orbital elements in terms of the conserved energy and angular momentum are provided by Eqs. (3.6) and (4.13) in Ref. [51]. These inputs allow us to compute 1PN accurate expressions for $r, \dot{r}, \phi$ and $\dot{\phi}$ in terms of $v, e_{\rm t}, \bar{n}, m$ and η. The explicit expressions of these dynamical variables are

$$r(v) = \frac{Gm}{c^2}\frac{1}{\bar{\xi}^{2/3}}(e_{\rm t}\cosh v - 1)\left\{1 + \bar{\xi}^{2/3}\,\frac{2\eta - 18 - (6-7\eta)e_{\rm t}\cosh v}{6\,(e_{\rm t}\cosh v - 1)}\right\} , \tag{5.50}$$

$$\dot{r}(v) = \bar{\xi}^{1/3}\frac{c\,e_{\rm t}\sinh v}{e_{\rm t}\cosh v - 1}\left\{1 - \bar{\xi}^{2/3}\frac{6-7\eta}{6}\right\} , \tag{5.51}$$

$$\phi(v) - \phi_0 = 2\arctan\left[\left(\frac{e_\phi+1}{e_\phi-1}\right)^{1/2}\tanh v/2\right]\left\{1 + \bar{\xi}^{2/3}\frac{3}{e_{\rm t}^2-1}\right\} , \tag{5.52}$$

$$\dot{\phi}(v) = \frac{\bar{n}\sqrt{e_{\rm t}^2-1}}{(e_{\rm t}\cosh v - 1)^2}\left\{1 - \bar{\xi}^{2/3}\,\frac{\left[3 - (4-\eta)\,e_{\rm t}^2 + (1-\eta)\,e_{\rm t}\cosh v\right]}{\left(e_{\rm t}^2-1\right)(e_{\rm t}\cosh v - 1)}\right\} . \tag{5.53}$$

To obtain Eqs. (5.50)-(5.53), we have used PN accurate relations connecting $e_{\rm r}$ and e_ϕ to $e_{\rm t}$, namely $e_{\rm r} = e_{\rm t}\{1-\bar{\xi}^{2/3}(8-3\eta)/2\}$ and $e_\phi = e_{\rm t}\{1-\bar{\xi}^{2/3}(4-\eta)\}$. The fact that we have invoked $e_{\rm t}$ to characterize the dynamics allows us to invoke Mikkola's approach to numerically solve the classical Kepler equation for hyperbolic orbits as detailed in Sec. 4 in Ref. [65]. We use the resulting $v(l)$ in Eqs. (5.50)-(5.53) to obtain 1PN accurate l evolution for $r, \dot{r}, \phi$ and $\dot{\phi}$ for a non-spinning compact binary characterized by $m, \eta, \bar{n}$ and $e_{\rm t}$. These evolutions are implemented in Eqs. (5.45)-(5.46) to obtain $h_+|_Q(t)$ and $h_\times|_Q(t)$ associated with compact binaries moving in 1PN accurate hyperbolic orbits.

We move on to compute explicit expressions for h_+ and $h_\times$ that are also 1PN accurate in their amplitudes. This requires us to implement Eqs. (5.2) for h_+ and $h_\times$ while using the 1PN accurate expression for $h_{ij}^{\rm TT}$ for general orbits that are available in Refs. [70, 71]. The resulting 1PN accurate amplitude corrected expressions for h_+ and $h_\times$ can be written as

$$h_+ = \frac{G\mu}{c^4 R}\left(h_+^N + \frac{1}{c}h_+^{0.5} + \frac{1}{c^2}h_+^1\right), \tag{5.54}$$

$$h_\times = \frac{G\mu}{c^4 R}\left(h_\times^N + \frac{1}{c}h_\times^{0.5} + \frac{1}{c^2}h_\times^1\right), \tag{5.55}$$

where $h_{+,\times}^N, h_{+,\times}^{0.5}$ and $h_{+,\times}^1$ are given by

$$h_+^N = 2r\dot{r}\dot{\phi}(1+C_\theta^2)\sin 2\phi + (1+C_\theta^2)\left(z + r^2\dot{\phi}^2 - \dot{r}^2\right)\cos 2\phi + S_\theta^2\left(\dot{r}^2 + r^2\dot{\phi}^2 - z\right), \tag{5.56}$$

$$h_\times^N = 2C_\theta\left(z + r^2\dot{\phi}^2 - \dot{r}^2\right)\sin 2\phi - 2C_\theta 2r\dot{r}\dot{\phi}\cos 2\phi, \tag{5.57}$$

$$\begin{aligned} h_+^{0.5PN} = \frac{S_\theta}{2}(X_1 - X_2) \times \Bigg[& (3C_\theta^2 - 1)\left(\dot{r}^2 + r^2\dot{\phi}^2 - 2z\right)\dot{r}\cos\phi \\ & + (1+C_\theta^2)\left(\dot{r}^2 - 3r^2\dot{\phi}^2 - 2z\right)\dot{r}\cos 3\phi - \Bigg((\dot{r}^2 + r^2\dot{\phi}^2 - z)(3C_\theta^2 - 1) \\ & - z\,(C_\theta^2 + 5)\,\frac{1}{2}\Bigg) r\dot{\phi}\sin\phi + (1+C_\theta^2)\left(3\dot{r}^2 - r^2\dot{\phi}^2 - \frac{7}{2}z\right) r\dot{\phi}\sin 3\phi \Bigg], \end{aligned} \tag{5.58}$$

$$\begin{aligned} h_\times^{0.5PN} = \frac{C_\theta S_\theta}{2}(X_1 - X_2) \times \Big[& \left(2\dot{r}^2 + 2r^2\dot{\phi}^2 - 5z\right) r\dot{\phi}\cos\phi + \left(6\dot{r}^2 - 2r^2\dot{\phi}^2 - 7z\right) r\dot{\phi}\cos 3\phi \\ & + 2\left(\dot{r}^2 + r^2\dot{\phi}^2 - 2z\right)\dot{r}\sin\phi + 2\left(\dot{r}^2 - 3r^2\dot{\phi}^2 - 2z\right)\dot{r}\sin 3\phi \Big], \end{aligned} \tag{5.59}$$

$$
\begin{aligned}
h_{+}^{1PN} = & \frac{1}{24}\Bigg[z^2 S_\theta^2\,\left(116+7(1-3\eta)(1-3C_\theta^2)\right)+r^2\dot{\phi}^2 z\,S_\theta^2\,\left(51\eta-69+C_\theta^2 39(1-3\eta)\right)\\
&+18S_\theta^4\left(\dot{r}^4+r^4\dot{\phi}^4\right)(1-3\eta)-36\dot{r}^2S_\theta^4 r^2\dot{\phi}^2(3\eta-1)+6\dot{r}^2 z S_\theta^2\left(9C_\theta^2(1-3\eta)+3+13\eta\right)\Bigg]\\
&+\cos 2\phi\,\frac{1}{2}\Bigg[(\dot{r}^4-r^4\dot{\phi}^4)(1+C_\theta^2(1+2S_\theta^2))(3\eta-1)+r^2\dot{\phi}^2 z\Bigg(S_\theta^2(3\eta-1)(4+C_\theta^2)+(2+3\eta)\\
&\times(1+C_\theta^2)\Bigg)-\dot{r}^2 z\Bigg((3+2\eta)(1+C_\theta^2)+6C_\theta^2S_\theta^2(3\eta-1)\Bigg)+\frac{z^2}{3}\Bigg(7C_\theta^2S_\theta^2(3\eta-1)-29(1+C_\theta^2)\Bigg)\Bigg]\\
&+\cos 4\phi\,\frac{(1+C_\theta^2)S_\theta^2}{24}(3\eta-1)\Bigg[6(\dot{r}^4+r^4\dot{\phi}^4)+51r^2\dot{\phi}^2 z+7z^2-18\dot{r}^2(2r^2\dot{\phi}^2+z)\Bigg]\\
&-\sin 2\phi\,r\dot{r}\dot{\phi}\Bigg[(1+C_\theta^2(1+2S_\theta^2))(\dot{r}^2+r^2\dot{\phi}^2)(3\eta-1)\;-\;z\,\Bigg((2+4\eta)\,(1+C_\theta^2)\\
&+\frac{S_\theta^2}{2}(3\eta-1)(1+9C_\theta^2)\Bigg)\Bigg]\;-\;\sin 4\phi\;r\dot{r}\dot{\phi}\,(3\eta-1)(1+C_\theta^2)S_\theta^2\left(\dot{r}^2-r^2\dot{\phi}^2-\frac{9}{4}z\right)\,, \qquad (5.60)
\end{aligned}
$$

$$
\begin{aligned}
h_{\times}^{1PN} = & \;z r\dot{r}\dot{\phi}\;(1-3\eta)\,\frac{C_\theta S_\theta^2}{2}\;+\;\cos 2\phi\;r\dot{r}\dot{\phi}\,C_\theta\,\Bigg[2(1+S_\theta^2)\,(3\eta-1)\,\left(\dot{r}^2+r^2\dot{\phi}^2\right)\\
&-z\Bigg(4+8\eta+5S_\theta^2(3\eta-1)\Bigg)\Bigg]+\cos 4\phi\;r\dot{r}\dot{\phi}(3\eta-1)\,C_\theta S_\theta^2\left[2\dot{r}^2-2r^2\dot{\phi}^2-\frac{9}{2}z\right]\\
&+\sin 2\phi\;C_\theta\,\Bigg[\left(\dot{r}^4-r^4\dot{\phi}^4\right)\,(1+S_\theta^2)\,(3\eta-1)+z\frac{r^2\dot{\phi}^2}{2}\,\left(4+6\eta+5S_\theta^2(3\eta-1)\right)\\
&+z^2\,\frac{1}{6}\,\left(7S_\theta^2\,(3\eta-1)-58\right)\;-\;\dot{r}^2 z\,\left(3+2\eta+S_\theta^2\,(9\eta-3)\right)\Bigg]\\
&+\sin 4\phi\;(3\eta-1)\frac{C_\theta S_\theta^2}{12}\Bigg[6\dot{r}^4+6r^4\dot{\phi}^4+51r^2\dot{\phi}^2 z+7z^2-18\dot{r}^2\Bigg(2r^2\dot{\phi}^2+z\Bigg)\Bigg]\,. \qquad (5.61)
\end{aligned}
$$

We have verified that in the circular limit the above expressions reduce to Eqs. (3) and (4) in Ref. [66]. This requires us to equate $\dot{r}$ and $\dot{\phi}$ to zero and v/r, respectively, while replacing ϕ by $\phi+\pi/2$. This is done to make sure that the orbital phase is measured from the same axis as in [66]. Afterwards, we need to connect v and z by the 1PN-accurate relation $v=z^{1/2}+z^{3/2}\,(\eta-3)\,/(2\,c^2)$ and express z to the variable $x=(G\,m\,\dot{\phi}/c^3)^{2/3}$ of Ref. [66] through the 1PN-accurate relation $z=c^2\,x\,(1+(3-\eta)\,x/3)$.

We are now in a position to plot the Newtonian, 0.5PN and 1PN contributions to GW polarization states for non-spinning compact binaries moving in 1PN accurate hyperbolic orbits. This is pursued in Fig. 5.5 for a binary having $m_1=8M_\odot, m_2=13M_\odot$ to compare with Figs. 6-10 in Ref. [52] while choosing $e_{\rm t}$ to be 1.3 and 2. The first three rows display the Newtonian, 0.5PN and 1PN contributions to h_+ and $h_\times$ for binaries having fully 1PN accurate orbital evolution while the amplitude contributions are fully 1PN accurate for the fourth row plots. Apart from the change in their amplitudes, there are no changes in the way various contributions temporally evolve as we vary the orbital eccentricity. To make sure of the correctness of our approach, we have reproduced temporal evolution for the real and imaginary parts of the time derivatives of mass and current multipole moments that are displayed in Fig. 8 of [50]. Additionally, we are also able to reproduce temporal evolution for the real and imaginary parts of the $(2,2)$ GW mode depicted in Fig. 2 of [63] by our approach.

However, a visual comparison of our $e_{\rm t} = 2$ plots that appear in the first three rows of Fig. 5.5 with similar plots in Figs. 6,7 and 10 of Ref. [52] reveals substantial differences. The differences are clearly noticeable for the cross polarization states. Interestingly, plots in Figs. 8 of Ref. [52] that display what they describe as the multipolar 1PN corrections to GW polarization states are qualitatively in agreement with $e_{\rm t} = 2$ plots in the third row of our Fig. 5.5. The nature of the memory effect exhibited by the Newtonian contribution to $h_{\times}$, as shown in Fig. 6 of Ref. [52], is also qualitatively different from our plots and those available in the literature. We suspect that the observed differences may be due to the way temporal evolution is implemented in Ref. [52]. Note that this is implemented analytically as a PN series in terms of the coordinate time as evident from the PN accurate expression for their angular variable [52]. However, we describe orbital dynamics in a parametric way and invoke numerical solution of the PN accurate Kepler equation to obtain the time evolution. It will be interesting to probe why these approaches differ for hyperbolic orbits.

We turn to explain the presence of *linear memory effect* in both the quadrupolar order polarization states of spinning compact binaries in hyperbolic orbits. We begin by explaining, in detail, why only the cross polarization state exhibits the effect in the case of non-spinning compact binaries during hyperbolic encounters with the help of Refs. [62, 63]. This diversion is desirable as we can pinpoint the terms that explicitly cause the memory effect for such binaries. Unfortunately, this is rather impossible in the case of spinning compact binaries in hyperbolic orbits as several dynamical variables, present in the Eqs. (5.1) and (5.2) for $h_{+}|_{\rm Q}$ and $h_{\times}|_{\rm Q}$, can contribute to this effect. We begin by noting that an ideal GW detector will return to its original configuration after the passage of an incident GW, if the signal does not exhibit any memory effect. In contrast, transient GW signals that possess memory effects force the detector not to relapse to the initial configuration even after the passage of the GW. This is essentially due to a net change in the amplitude of the local metric induced by the passage of such a GW. This leads to the linear memory effect that we observe in Fig. 5.5.

Influenced by Ref. [62] and with the help of Eq. (5.5), we write the net change in the quadrupolar order far-zone radiation field as

$$\Delta h^{TT}_{ij}|_{\rm Q} = \frac{G}{c^4}\frac{2}{R}\Delta(\ddot{\mathscr{I}}^{TT}_{ij})\,, \tag{5.62}$$

where $\mathscr{I}_{ij}$ is the mass-quadrupole moment of the binary, given by $\mathscr{I}_{ij} = \mu\, x_i\, x_j$ at the Newtonian order. It is fairly straightforward to compute the second time derivative of the transverse-traceless part of $\mathscr{I}_{ij}$ using Newtonian equations of motion: $\ddot{x}_i = -G\,m\,x_i/r^3$. The resulting expression reads

$$\ddot{\mathscr{I}}^{TT}_{ij} = 2\mu\big(\dot{x}_i\,\dot{x}_j - \frac{G\,m}{r^3}x_i\,x_j\big) \tag{5.63}$$

The second term in Eq. (5.63) vanishes for $t \to \pm\infty$ as it falls off like $1/r$. This is because $v \to \pm\infty$ as $t \to \pm\infty$ due to Eq. (5.49) and $r(v)$ is proportional to $(e_t\,\cosh v - 1)$ as evident from Eqs. (5.50)-(5.53). However, the magnitude of the relative velocity approaches a finite value, namely $\mathrm{v}_\infty = \sqrt{2E}$ (note that E stands for the orbital energy scaled by μ). This results in the following expression for the Newtonian order linear memory effect associated with hyperbolic passages

$$\Delta h_{ij} = 4\frac{G\mu}{c^4 R}\Delta(\dot{x}_i\,\dot{x}_j)\,. \tag{5.64}$$

Clearly, the differences in the components of the orbital velocity as $t \to \pm\infty$ contribute substantially to the magnitude of memory effect.

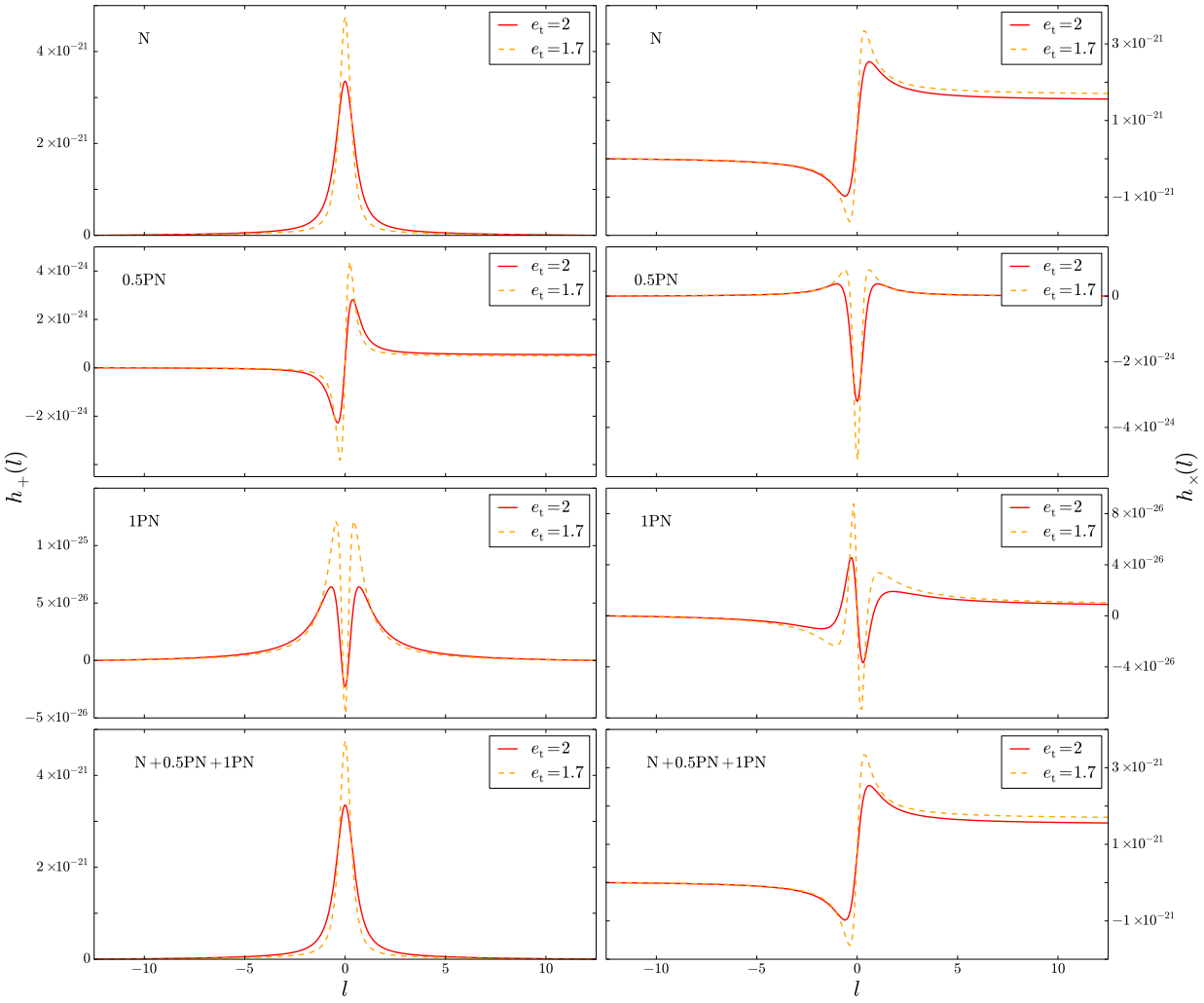

Figure 5.5: Polarization states at Newtonian, 0.5PN and 1PN order, as well as their sum, respectively, as functions of l for non-spinning compact binaries in hyperbolic orbits. The solid line shows the case where $e_t = 2$ and the dashed line shows the waveform for $e_t = 1.7$. The masses are $m_1 = 8\,M_\odot$ and $m_2 = 13\,M_\odot$, while the minimal distance is chosen to be $r_{\rm min} \sim 1.9 \times 10^9 m$, as in Ref. [52]. The waveform for the h_+ polarization is shown on the left and $h_\times$ appears on the right.

To demonstrate explicitly the memory effect, let us consider the following scenario where the observer is perpendicular to the orbital plane ($\theta = 0$ orientation). We infer that the non-zero components of $\mathscr{I}_{ij}$ are $\mathscr{I}_{11}, \mathscr{I}_{22}$ and $\mathscr{I}_{12} = \mathscr{I}_{21}$, where indices 1 and 2 stand for the x and y components in the $\boldsymbol{j}_0$-based inertial frame. Additionally, x and y components of the orbital velocity as $t \to \pm\infty$ are given by

$$\lim_{t\to\pm\infty} \dot{x}_1 = \pm \mathrm{v}_\infty \cos\pm\phi_\infty \,, \tag{5.65}$$

$$\lim_{t\to\pm\infty} \dot{x}_2 = \pm \mathrm{v}_\infty \sin\pm\phi_\infty \,, \tag{5.66}$$

where ϕ_∞ stands for the asymptotic value for the orbital phase as $t \to \pm\infty$, which can be deduced from Eqs. (5.47)-(5.48) and (5.49). With these inputs and some trigonometric manipulations, we obtain the following expressions for the linear memory amplitudes associated

with different components of h_{ij}

$$\Delta h_{ii} = 0 \,, \qquad i = 1,2 \,, \tag{5.67}$$

$$\Delta h_{ij} = -8\frac{G\mu}{c^4}\frac{E}{R}\sin 2\phi_\infty \,, \qquad i \neq j \,. \tag{5.68}$$

In what follows we show that our expressions for the quadrupolar order h_+ and $h_\times$, given by Eqs. (5.45)-(5.46), are indeed consistent with the above estimates.
To make contact with the above discussions, we consider again the binary configuration having $\theta = 0$. It is fairly straightforward to obtain $t \to \pm\infty$ limits of our quadrupolar order expressions for $h_+|_Q(t)$ and $h_\times|_Q(t)$, given by Eqs. (5.45) and (5.46). It may be recalled that v also approaches $\pm\infty$ as $t \to \pm\infty$ due to Eq. (5.49). This ensures that the dynamical variables $z(v) = Gm/r(v), \dot{\phi}(v)$ and the product $r(v)\dot{\phi}(v)$, displayed in Eqs. (5.50)-(5.53), go to zero in the limit $v \to \pm\infty$. This is of course due to the presence of $(e_t \cosh v - 1)$ and its powers in the denominators of these parametric expressions. However, the expression for $\dot{r}(v)$ does not vanish as $t \to \pm\infty$, but rather tends to the finite value, namely v_∞. This forces the expressions for $h_+|_Q(t)$ and $h_\times|_Q(t)$, given by Eqs. (5.45) and (5.46), at $t \to +\infty$ to be

$$h_+|_Q = -2\frac{G\mu}{c^4 R}\mathrm{v}_\infty^2 \cos 2\phi_\infty \,, \tag{5.69}$$

$$h_\times|_Q = -2\frac{G\mu}{c^4 R}\mathrm{v}_\infty^2 \sin 2\phi_\infty \,. \tag{5.70}$$

Note that the right hand side of Eq. (5.69) is an even function of ϕ due to the presence of $\cos 2\phi$. However, the right hand side of Eq. (5.70) is an odd function of ϕ. This implies that

$$\lim_{t\to+\infty} h_+|_Q(t) = \lim_{t\to-\infty} h_+|_Q(t) \,, \tag{5.71}$$

$$\lim_{t\to+\infty} h_\times|_Q(t) = -\lim_{t\to-\infty} h_\times|_Q(t) \,. \tag{5.72}$$

Therefore, the amplitude differences in the above two polarization states between the early and late times during hyperbolic encounters are

$$\Delta h_+ = 0 \,, \tag{5.73}$$

$$\Delta h_\times = -8\frac{G\mu}{c^4}\frac{E}{R}\sin 2\phi_\infty \,, \tag{5.74}$$

where we used the relation $\mathrm{v}_\infty^2 = 2E$. Clearly, the above two expressions are identical to Eqs. (5.67) and (5.68) that we derived using the detailed discussions of Ref. [62]. This also explains the linear memory effect exhibited by the first row plots in Fig. 5.5.
It is possible to employ similar arguments to show that 0.5PN contributions to h_+, given by Eq. (5.58),and 1PN contributions to $h_\times$, given by Eq. (5.61), should exhibit the linear memory effects during the hyperbolic encounters. This is essentially due to the presence of non-vanishing odd functions $\dot{r}^3\cos\phi$ and $\dot{r}^3\cos 3\,\phi$, as well as $\dot{r}^4\sin 2\,\phi$ and $\dot{r}^4\sin 4\,\phi$ in the above expressions. Terms like $\dot{r}^3\sin\phi$ or $\dot{r}^3\sin 3\,\phi$ appearing in the expression for $h_\times$ at 0.5PN order will not contribute to the memory, since both the $\dot{r}^3$ and the $\sin\phi$ factors are odd functions of time and yield therefore an even term. The second and third row plots in Fig. 5.5 clearly support the above inference. In contrast, both 0.5PN order GW polarization states, depicted in Fig. 7 in [52], show the memory effect as evident from their dashed line plots. This is also applicable to 1PN order corrections to $h_\times$ and h_+, as displayed by the dashed line plots in Fig. 9

in [52], that arise from perturbative description of their orbital elements. Clearly, such plots are inconsistent with plots in our Fig. 5.5.

When we include the spin effects, it is rather difficult to obtain similar analytic estimates to demonstrate why both polarization states should exhibit the linear memory effect. However, note that the expressions for both $h_+|_Q(t)$ and $h_\times|_Q(t)$ contain terms like $\dot{r}^2 \sin 2\Phi(t)$ as evident from our Eqs. (5.1) and (5.2). Additionally, the phasing angle $\Phi(t)$ does not have the same value at $t = \pm\infty$ anymore due to the spin-orbit coupling induced precession of the orbital plane. These effects force the plots of $h_+|_Q(t)$ and $h_\times|_Q(t)$ to exhibit the linear memory effect as displayed in the previous section.

Finally, let us comment about the impact of orbital eccentricity on the amplitude of the memory effect. This should be easily extractable with the help of Eqs. (5.73) and (5.74) and the fact that the angle at infinite times ϕ_∞ is related to e_t through the relation $\cos\phi_\infty = -1/e_t$. This relation is also equivalent to $\sin 2\phi_\infty = -2\sqrt{e_t^2-1}/e_t^2$. Therefore, the memory goes to 0 when $e_t \to 1$ and we have $\Delta h_\times \propto 1/e_t$ for $e_t \gg 1$. Moreover, the amplitude of the effect peaks at eccentricity $e_t = \sqrt{2}$ and this is consistent with our results of the present and previous sections. Let us also comment about the plausibility of observing the influences of memory effect. Unfortunately, laser interferometric GW observatories are not the ideal instruments to probe the implications of both linear and non-liner memory effects as explained in Ref. [62]. This is essentially because the internal forces present in such instruments are expected to bring the test masses back to their original (or initial) configurations. However, it may be possible to detect the implications of non-linear memory effects associated with the merger of supermassive black hole binaries with the help of the ongoing and planned pulsar timing arrays (PTAs) [72]. This is despite the fact that characteristic merger frequencies of such binaries are far higher than the nano-Hertz regime, relevant for PTAs.

5.4 Conclusions

We provided an efficient prescription to compute GW polarizations that are PN accurate both in amplitude and phase evolution for spinning compact binaries in hyperbolic orbits. The incorporated spin effects are due to the dominant order spin-orbit interactions while the non-spinning orbital dynamics is 1PN accurate. The radial part of the conservative 1.5PN accurate orbital dynamics is treated in a parametric way by adapting the Keplerian type parametric solution for eccentric orbits, available in Ref. [68]. We invoked Mikkola's accurate and efficient method to numerically solve the hyperbolic version of the Kepler Equation to obtain temporal evolution for r and $\dot{r}$. In contrast, the 1.5PN accurate angular sector of the dynamics is tackled numerically by solving differential equations that describe the orbital phase evolution and the precessional dynamics of $\boldsymbol{s}_1, \boldsymbol{s}_2$ and $\boldsymbol{k}$. We also incorporated the influence of GW emission on this 1.5PN accurate orbital dynamics. Afterwards, we numerically inserted the variables that describe the radial, angular and precessional aspects of the orbital dynamics into PN accurate expressions for the two GW polarization states for compact binaries in general orbits. This is how we constructed ready-to-use waveforms for spinning compact binaries in hyperbolic orbits.

We observed the presence of linear GW memory effect in both the polarization states. In contrast, only the cross polarization state exhibits the memory effect for non-spinning compact binaries in hyperbolic orbits and we provided an explanation for these observations. We explored the influence of orbital eccentricity, mass ratio and dominant spin orientation on the evolution of the two polarization states and the amplitude of the memory effect. Invoking

the non-spinning version of our approach, we have reproduced the temporal evolution for the real and imaginary parts of the time derivatives of mass and current multipole moments and associated GW modes, detailed in Refs. [50, 63]. However, various temporally evolving PN contributions to h_+ and $h_\times$ associated with non-spinning compact binaries, displayed in Figs. 6, 7, 9 and 10 of Ref. [52], are visually different from what we obtained. We provided a possible qualitative explanation for these differences.

It will be interesting to incorporate the 2PN order non-spinning contributions to our 1.5PN accurate orbital dynamics. This is rather tricky due to the appearance of 2PN order $f - u \equiv 2\tan^{-1}\left(\beta_\phi \sin u/(1-\beta_\phi \cos u)\right)$ term in the PN accurate Kepler Equation for eccentric binaries, where $\beta_\phi = (1-\sqrt{1-e_\phi^2})/e_\phi$ and f is the true anomaly [73, 74]. The presence of the above $f-u$ term leads to certain imaginary terms in the 2PN accurate Kepler Equation while adapting the usual argument of analytic continuation, namely $u \to \imath v$, to obtain its hyperbolic version. An interesting extension will be to incorporate the effects of dominant order spin-spin interactions. Another challenging direction will be to adapt Refs. [75, 76] to describe GW burst signals while employing the framework of effective-one-body formalism. It will be also desirable to pursue possible data analysis implications of these templates. A possible direction may involve probing the ability of GW search algorithms like in Ref. [77], constructed to capture unmodelled gravitational-wave bursts, to detect and distinguish our accurately modeled GW bursts.

5.5 Acknowledgements

We would like to thank Simone Balmelli and Cédric Huwyler for useful discussions, and the SNF for hosting AG at the Physik-Institut in Zürich during the initial stages of this work. We thank C. Berry for his detailed review of this article and the referee for many helpful suggestions. This is a LIGO document, LIGO-P1400065.

5.6 Appendix

5.6.1 1PN accurate polarization states expressions for spinning binaries

We list below the 1PN accurate expressions for h_+ and $h_\times$ for spinning binaries on general orbits in a compact form that incorporate 1PN accurate non-spinning and 1PN order spin-

orbit contributions.

$$
\begin{aligned}
h_+ = {} & 2\,\frac{G\,\mu}{c^4\,R}\times \qquad (5.75)\\
&\Big\{\Big[\left((\boldsymbol{q}\cdot\boldsymbol{n})^2-(\boldsymbol{p}\cdot\boldsymbol{n})^2\right)z+(\boldsymbol{p}\cdot\mathbf{v})^2-(\boldsymbol{q}\cdot\mathbf{v})^2\Big]-\frac{X_1-X_2}{2\,c}\Big[\big((\boldsymbol{N}\cdot\boldsymbol{n})\,\dot r-(\boldsymbol{N}\cdot\mathbf{v})\big)(\boldsymbol{p}\cdot\boldsymbol{n})^2 z\\
&-6z\,(\boldsymbol{N}\cdot\boldsymbol{n})(\boldsymbol{p}\cdot\boldsymbol{n})(\boldsymbol{p}\cdot\mathbf{v})\;+\;\Big(\big(\boldsymbol{N}\cdot\mathbf{v}-3\,(\boldsymbol{N}\cdot\boldsymbol{n})\,\dot r\big)\Big)(\boldsymbol{q}\cdot\boldsymbol{n})^2 z+6z\,(\boldsymbol{N}\cdot\boldsymbol{n})(\boldsymbol{q}\cdot\boldsymbol{n})(\boldsymbol{q}\cdot\mathbf{v})\\
&+2\big((\boldsymbol{p}\cdot\mathbf{v})^2-(\boldsymbol{q}\cdot\mathbf{v})^2\big)\;(\boldsymbol{N}\cdot\mathbf{v})\Big]\;+\;\frac{1}{6\,c^2}\;\Big[6\,(\boldsymbol{N}\cdot\mathbf{v})^2\;\big((\boldsymbol{p}\cdot\mathbf{v})^2-(\boldsymbol{q}\cdot\mathbf{v})^2\big)\;(1-3\,\eta)\\
&+\Big((6\,\eta-2)(\boldsymbol{N}\cdot\mathbf{v})^2\big((\boldsymbol{p}\cdot\boldsymbol{n})^2-(\boldsymbol{q}\cdot\boldsymbol{n})^2\big)+(96\,\eta-32)\;(\boldsymbol{N}\cdot\mathbf{v})(\boldsymbol{N}\cdot\boldsymbol{n})(\boldsymbol{p}\cdot\mathbf{v})(\boldsymbol{p}\cdot\boldsymbol{n})\\
&-(96\,\eta-32)(\boldsymbol{N}\cdot\mathbf{v})(\boldsymbol{N}\cdot\boldsymbol{n})(\boldsymbol{q}\cdot\mathbf{v})(\boldsymbol{q}\cdot\boldsymbol{n})+\big((42\,\eta-14)(\boldsymbol{N}\cdot\boldsymbol{n})^2-4+6\,\eta\big)(\boldsymbol{p}\cdot\mathbf{v})^2\\
&+\big((14-42\;\eta)(\boldsymbol{N}\cdot\boldsymbol{n})^2+4-6\;\eta\big)(\boldsymbol{q}\cdot\mathbf{v})^2\Big)\,z+\big((3-9\;\eta)(\boldsymbol{p}\cdot\mathbf{v})^2+(9\;\eta-3)(\boldsymbol{q}\cdot\mathbf{v})^2\big)\,\nu^2\\
&+\Big(\big(29+(7-21\,\eta)(\boldsymbol{N}\cdot\boldsymbol{n})^2\big)(\boldsymbol{p}\cdot\boldsymbol{n})^2+\big(-29+(21\,\eta-7)(\boldsymbol{N}\cdot\boldsymbol{n})^2\big)\;(\boldsymbol{q}\cdot\boldsymbol{n})^2\Big)z^2\\
&+\Big(\big((3-9\,\eta)(\boldsymbol{N}\cdot\boldsymbol{n})^2-10-3\,\eta\big)(\boldsymbol{p}\cdot\boldsymbol{n})^2+\big((9\,\eta-3)(\boldsymbol{N}\cdot\boldsymbol{n})^2+10+3\,\eta\big)(\boldsymbol{q}\cdot\boldsymbol{n})^2\Big)\,z\,\nu^2\\
&+\Big((12-36\,\eta)(\boldsymbol{N}\cdot\mathbf{v})(\boldsymbol{N}\cdot\boldsymbol{n})(\boldsymbol{p}\cdot\boldsymbol{n})^2+\big((30-90\,\eta)(\boldsymbol{N}\cdot\boldsymbol{n})^2+20+12\,\eta\big)(\boldsymbol{p}\cdot\mathbf{v})(\boldsymbol{p}\cdot\boldsymbol{n})\\
&+(36\,\eta-12)(\boldsymbol{N}\cdot\mathbf{v})(\boldsymbol{N}\cdot\boldsymbol{n})(\boldsymbol{q}\cdot\boldsymbol{n})^2+\big((90\,\eta-30)(\boldsymbol{N}\cdot\boldsymbol{n})^2-12\,\eta-20\big)(\boldsymbol{q}\cdot\mathbf{v})(\boldsymbol{q}\cdot\boldsymbol{n})\Big)\,z\,\dot r\\
&+\Big(\;\big((45\,\eta-15)(\boldsymbol{N}\cdot\boldsymbol{n})^2-9\,\eta+3\big)\;(\boldsymbol{p}\cdot\boldsymbol{n})^2+\big((15-45\,\eta)(\boldsymbol{N}\cdot\boldsymbol{n})^2-3+9\,\eta\big)(\boldsymbol{q}\cdot\boldsymbol{n})^2\Big)\;\Big]\\
&+\frac{z^2}{c^2}\Big[(\boldsymbol{p}\cdot\boldsymbol{n})\,(X_2\chi_2\boldsymbol{p}\cdot(\boldsymbol{s}_2\times\boldsymbol{N})-X_1\chi_1\boldsymbol{p}\cdot(\boldsymbol{s}_1\times\boldsymbol{N}))+(\boldsymbol{q}\cdot\boldsymbol{n})\,(X_1\chi_1\boldsymbol{q}\cdot(\boldsymbol{s}_1\times\boldsymbol{N})-X_2\chi_2\boldsymbol{q}\cdot(\boldsymbol{s}_2\times\boldsymbol{N}))\Big]\Big\}\,,
\end{aligned}
$$

$$
\begin{aligned}
h_\times = {} & 4\,\frac{G\,\mu}{c^4\,R}\times \qquad (5.76)\\
&\Big\{\Big[(\boldsymbol{p}\cdot\mathbf{v})(\boldsymbol{q}\cdot\mathbf{v})-(\boldsymbol{p}\cdot\boldsymbol{n})(\boldsymbol{q}\cdot\boldsymbol{n})z\Big]-\frac{X_1-X_2}{c}\Big[\Big(\Big([3\,(\boldsymbol{N}\cdot\boldsymbol{n})\,\dot r-(\boldsymbol{N}\cdot\mathbf{v})](\boldsymbol{q}\cdot\boldsymbol{n})-3\,(\boldsymbol{N}\cdot\boldsymbol{n})(\boldsymbol{q}\cdot\mathbf{v})\Big)\\
&\times(\boldsymbol{p}\cdot\boldsymbol{n})-3\,(\boldsymbol{N}\cdot\boldsymbol{n})(\boldsymbol{q}\cdot\boldsymbol{n})(\boldsymbol{p}\cdot\mathbf{v})\Big)z+2\,(\boldsymbol{p}\cdot\mathbf{v})(\boldsymbol{q}\cdot\mathbf{v})(\boldsymbol{N}\cdot\mathbf{v})\Big]+\frac{1}{6\,c^2}\Big[6\,(1-3\,\eta)(\boldsymbol{N}\cdot\mathbf{v})^2\\
&\times(\boldsymbol{p}\cdot\mathbf{v})(\boldsymbol{q}\cdot\mathbf{v})+\Big(\;\big((6\,\eta-2)(\boldsymbol{N}\cdot\mathbf{v})^2(\boldsymbol{q}\cdot\boldsymbol{n})+(48\,\eta-16)(\boldsymbol{N}\cdot\mathbf{v})(\boldsymbol{N}\cdot\boldsymbol{n})(\boldsymbol{q}\cdot\mathbf{v})\big)\;(\boldsymbol{p}\cdot\boldsymbol{n})\\
&+(48\,\eta-16)(\boldsymbol{N}\cdot\mathbf{v})(\boldsymbol{N}\cdot\boldsymbol{n})(\boldsymbol{p}\cdot\mathbf{v})(\boldsymbol{q}\cdot\boldsymbol{n})+\big((42\,\eta-14)(\boldsymbol{N}\cdot\boldsymbol{n})^2-4+6\,\eta\big)(\boldsymbol{q}\cdot\mathbf{v})(\boldsymbol{p}\cdot\mathbf{v})\Big)\,z\\
&+(3-9\,\eta)\;(\boldsymbol{q}\cdot\mathbf{v})(\boldsymbol{p}\cdot\mathbf{v})\,\nu^2+\big(29+(7-21\,\eta)(\boldsymbol{N}\cdot\boldsymbol{n})^2\big)\;(\boldsymbol{q}\cdot\boldsymbol{n})(\boldsymbol{p}\cdot\boldsymbol{n})\,z^2\;+\big((3-9\,\eta)(\boldsymbol{N}\cdot\boldsymbol{n})^2\\
&-10-3\,\eta\big)(\boldsymbol{q}\cdot\boldsymbol{n})(\boldsymbol{p}\cdot\boldsymbol{n})\,z\,\nu^2+\Big(\big((-36\,\eta+12)(\boldsymbol{N}\cdot\mathbf{v})(\boldsymbol{N}\cdot\boldsymbol{n})(\boldsymbol{q}\cdot\boldsymbol{n})+\big((15-45\,\eta)(\boldsymbol{N}\cdot\boldsymbol{n})^2\\
&+10+6\,\eta\big)(\boldsymbol{q}\cdot\mathbf{v})\big)(\boldsymbol{p}\cdot\boldsymbol{n})+\big((15-45\,\eta)(\boldsymbol{N}\cdot\boldsymbol{n})^2+10+6\,\eta\big)(\boldsymbol{p}\cdot\mathbf{v})(\boldsymbol{q}\cdot\boldsymbol{n})\Big)\,\dot r\,z+((45\,\eta-15)\\
&\times(\boldsymbol{N}\cdot\boldsymbol{n})^2-9\,\eta+3)(\boldsymbol{q}\cdot\boldsymbol{n})(\boldsymbol{p}\cdot\boldsymbol{n})\,\dot r^2\,z\Big]+\frac{z^2}{c^2}\,(\boldsymbol{q}\cdot\boldsymbol{n})\Big[X_2\chi_2(\boldsymbol{p}\cdot(\boldsymbol{s}_2\times\boldsymbol{N}))-X_1\chi_1(\boldsymbol{p}\cdot(\boldsymbol{s}_1\times\boldsymbol{N}))\Big]\Big\}\,.
\end{aligned}
$$

The dot products that appear in the above equations, as expected, are evaluated in the $(\boldsymbol{p},\boldsymbol{q},\boldsymbol{N})$ frame. These dot products can be written in terms of the Eulerian angles $\Phi(t)$, $\alpha(t)$, $\iota(t)$, and the constant angle θ and are given by

$$\boldsymbol{p}\cdot\boldsymbol{n} = -\cos\Phi\sin\alpha - \sin\Phi\cos\alpha\cos\iota\ , \tag{5.77}$$

$$\boldsymbol{q}\cdot\boldsymbol{n} = C_\theta(\cos\Phi\cos\alpha - \sin\Phi\sin\alpha\cos\iota) - S_\theta\sin\iota\sin\Phi\ , \tag{5.78}$$

$$\boldsymbol{p}\cdot\mathbf{v} = r\dot{\Phi}\ (\sin\Phi\sin\alpha - \cos\Phi\cos\alpha\cos\iota) - \dot{r}\ (\cos\Phi\sin\alpha + \sin\Phi\cos\alpha\cos\iota)\ , \tag{5.79}$$

$$\begin{aligned}\boldsymbol{q}\cdot\mathbf{v} = {}& \dot{r}\ (C_\theta(\cos\Phi\cos\alpha - \sin\Phi\sin\alpha\cos\iota) - S_\theta\sin\Phi\sin\iota)\\ & - r\dot{\Phi}\ (C_\theta(\sin\Phi\cos\alpha + \cos\Phi\sin\alpha\cos\iota) + S_\theta\cos\Phi\sin\iota)\ ,\end{aligned} \tag{5.80}$$

$$\boldsymbol{N}\cdot\boldsymbol{n} = C_\theta\sin\Phi\sin\iota + S_\theta(\cos\Phi\cos\alpha - \sin\Phi\sin\alpha\cos\iota)\ , \tag{5.81}$$

$$\begin{aligned}\boldsymbol{N}\cdot\mathbf{v} = {}& \dot{r}\ (S_\theta(\cos\Phi\cos\alpha - \sin\Phi\sin\alpha\cos\iota) + C_\theta\sin\Phi\sin\iota)\\ & - r\dot{\Phi}\ (S_\theta(\sin\Phi\cos\alpha + \cos\Phi\sin\alpha\cos\iota) - C_\theta\sin\Phi\sin\iota)\ .\end{aligned} \tag{5.82}$$

The explicit evaluation of Eqs. (5.75) and (5.76) with the help of the above dot products leads to amplitude corrected GW polarization states for spinning compact binaries on general orbits. We can numerically impose the evolution of various variables for the hyperbolic orbits to obtain the amplitude corrected polarization states for spinning binaries on hyperbolic orbits.

Chapter 6

The linear memory effect in gravitational waves from hyperbolic binaries

Y. Boetzel, L. De Vittori, Ph. Jetzer

Submitted to Physical Review D, 2015 [3]

Abstract

We study the linear memory effect in gravitational waves from non-spinning compact binaries in hyperbolic orbits. We give explicit expressions for the memory in the polarization states up to first post-Newtonian order and relate it to the general Liénard-Wiechert solution to the linearized field equations of unbound systems, first derived in [78]. We find that the linear memory will be difficult to measure for hyperbolic binaries. For usual encounters of stars in globular clusters the expected strain lies below the sensitivities of planed space-based detectors such as eLISA. High velocity encounters between massive objects produce substantial memory within the sensitivity range of eLISA, although the rate of such events is difficult to estimate.

6.1 Introduction

The most promising sources for ground- and space-based detectors are inspiralling compact binaries, two-body systems composed of neutron stars and black holes in the late stage of their orbital evolution. Compact binaries in unbound orbits are another plausible source of gravitational waves. They occur in dense stellar environment present in globular clusters and galactic nuclei. The waveform of such an encounter has a "burst" signature, with the maximum amplitude at periapsis. An interesting effect of unbound orbits is the occurrence of linear memory. It refers to a permanent displacement of an ideal detector after the passing of the wave. By ideal detector we mean one that is only subjected to gravitational forces, e.g. a

ring of freely falling testmasses. After the passing of a wave with memory, the final state of the detector is different from its initial state, i.e. the gravitational wave leaves an imprint on the displacement of the testmasses. This corresponds to an observed difference in the metric perturbation

$$\Delta h_{+,\times} = \lim_{t\to+\infty} h_{+,\times} - \lim_{t\to-\infty} h_{+,\times}\,, \tag{6.1}$$

where the $h_{+,\times}$ are the usual plus and cross polarization. Note that ground-based detectors will not measure any memory effect, as the mirrors used in the interferometers are not truly freely falling. After the passing of the wave they will return to their initial state and any information about memory will be lost. Space-based detectors are truly free falling and thus ideal detectors. As such they will be able to measure differences between initial and final state.
There are two types of gravitational wave memory, linear and non-linear. The linear memory effect was first described in the 1970s [78–80] and is due to sources that produce a change in one of their multipole moments, the most evident example being hyperbolic binaries. The non-linear or Christodoulou memory [81] is a hereditary effect, sourced by the energy flux of the gravitational waves. It depends on the entire past history of the source, and thus for hyperbolic binaries contributions from the non-linear memory only enter the waveform at relative 2.5PN order [63]. In this work we concentrate on the linear memory effect and may also refer to it simply as memory or memory effect.
Explicit expressions for the linear memory of hyperbolic binaries have so far only been given to leading Newtonian order, see e.g. [2, 63]. Here we give expressions for the 0.5PN and 1PN corrections to the wave polarizations from the memory effect in the case of non-spinning compact binaries in hyperbolic orbits. We also give an explicit derivation of the general formula for the linear memory, first presented in [78], and show how it reduces to the same expressions in a low-velocity limit. Finally, we discuss the dependence of the memory on the initial parameters of the binary system, such as mass-ratio, eccentricity and initial velocity.

6.2 Linear memory effect

6.2.1 Reference frames

In order to describe the dynamics of a hyperbolic binary we introduce two important inertial systems: The frame of the observer and the center-of-mass frame of the orbital motion. Expressions for gravitational radiation are easily calculated in the center-of-mass frame, but in the end we are interested in what the observer (e.g. eLISA) measures. We additionally assume that the center-of-mass of the binary system is stationary with respect to the frame of the observer.
We follow the conventions from [2]. The orthonormal frame $(\boldsymbol{e}_1, \boldsymbol{e}_2, \boldsymbol{e}_3)$ is such that its origin coincides with the center-of-mass of the binary system and such that $\boldsymbol{e}_3$ is parallel to the orbital angular momentum $\boldsymbol{J}$. We denote by $\boldsymbol{n}$ the unit vector in direction of the observer, and $\boldsymbol{e}_1$ is such that it is parallel to the projection of $\boldsymbol{n}$ onto the orbital plane. Further, $\boldsymbol{p}$ is chosen to be antiparallel to $\boldsymbol{e}_2$, and $\boldsymbol{q}$ is such that the frame $(\boldsymbol{n}, \boldsymbol{p}, \boldsymbol{q})$ is orthonormal. We denote by θ the angle between the angular momentum $\boldsymbol{J}$ and the line-of-sight vector $\boldsymbol{n}$. The angle between the $\boldsymbol{e}_1$-axis and the periapsis of the orbital motion is denoted by ϕ_0. Thus in the center-of-mass frame the vectors $\boldsymbol{n}$, $\boldsymbol{p}$ and $\boldsymbol{q}$ are given by $\boldsymbol{n} = (\sin\theta, 0, \cos\theta)$, $\boldsymbol{p} = (0, -1, 0)$ and $\boldsymbol{q} = (\cos\theta, 0, -\sin\theta)$. We note that the center-of-mass frame is an inertial one, i.e. there is no precession of the orbital plane since we are only considering non-spinning systems.

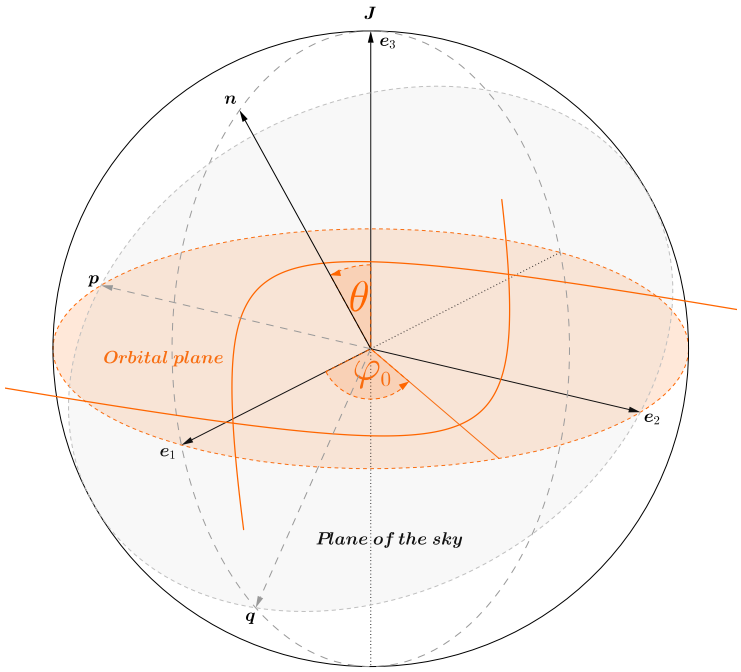

Figure 6.1: Orientation of the orbital plane and the plane of the sky. $(\boldsymbol{n},\boldsymbol{p},\boldsymbol{q})$ is the frame of the observer, $(\boldsymbol{e}_1,\boldsymbol{e}_2,\boldsymbol{e}_3)$ is a frame in the orbital plane. The two hyperbola in the orbital plane show a possible trajectory of a binary system.

6.2.2 Multipole expansion

We assume that at early and late times the particles move without interacting, so the gravitational fields are weak and we can work within the framework of linear gravity. Starting from the linearized field equations

$$\Box\bar{h}_{\mu\nu} = -\frac{16\pi G}{c^4}T_{\mu\nu}, \tag{6.2}$$

the solution for the metric perturbation $h_{\mu\nu} = g_{\mu\nu} - \eta_{\mu\nu}$ far away from the source in the transverse-traceless gauge is given by

$$h_{ij}^{TT} = \frac{4G}{c^4R}\mathscr{P}_{ij,ab}(\boldsymbol{n})\sum_{l=0}^{\infty}\frac{1}{c^l l!}n_L(\partial_t^l S^{ab,L})\Big|_{t_r}. \tag{6.3}$$

We use multiindices $n_L = n_{i_1}\dots n_{i_l}$, $\mathscr{P}_{ij,kl}(\boldsymbol{n})$ is the projection tensor to the transverse-traceless gauge, $t_r = t - r/c$ is the retarded time and the moments of the stress tensor T^{ij} are defined as

$$S^{ij,L}(t) = \int d^3x\; x^L T^{ij}(t,\boldsymbol{x}). \tag{6.4}$$

This is the basis for the multipole expansion of the field at null infinity. The tensors $S^{ij,L}$ are symmetric under exchange of i and j, and also under the exchange of any of the multiindices L, though not under the exchange of i or j and any of the indices L. They can be related to the symmetric trace-free radiative mass- and current-multipole moments U_L and V_L via

$$h_{ij}^{TT} = \frac{4G}{c^2R}\mathscr{P}_{ij,ab}(\boldsymbol{n})\sum_{l=2}^{\infty}\frac{1}{c^l l!}\Big\{n_{L-2}U_{abL-2} - \frac{2l}{c(l+1)}n_{cL-2}\epsilon_{cd(a}V_{b)dL-2}\Big\}\Big|_{t_r}. \tag{6.5}$$

The radiative moments can be related to a set of intermediate moments M_L and S_L, which in turn then can be related to the source moments $(I_L, J_L, W_L, X_L, Y_L, Z_L)$. These allow for closed form expressions as integrals over the source (See [82] for a detailed treatment). E.g. to lowest order we find, that $S^{ij} = 1/2U_{ij} = 1/2\ddot{M}_{ij}$, with M_{ij} given by the quadrupole moment of the source

$$M_{ij}(t) = \frac{1}{c^2}\int d^3x(x_{ij} - (1/3)\delta_{ij}|\boldsymbol{x}|^2)T^{00}(t,\boldsymbol{x})\,. \tag{6.6}$$

For our calculations it is though easier to work with the moments of the stress tensor.

6.2.3 Memory to next-to-leading order

The energy-momentum tensor for noninteracting particles is given by

$$T^{\mu\nu}(t,\boldsymbol{x}) = \sum_{a=1,2} m_i\gamma_a v_a^\mu v_a^\nu \delta^{(3)}(\boldsymbol{x} - \boldsymbol{x}_a(t))\,. \tag{6.7}$$

The tensors $S^{ij,L}$ are now easily found to be

$$S^{ij,L} = \sum_{a=1,2} m_a\gamma_a v_a^i v_a^j x_a^L\,. \tag{6.8}$$

To get expressions correct to first post-Newtonian order it is sufficient to work in a Newtonion center-of-mass frame. We thus have $\boldsymbol{r} = \boldsymbol{r}_1 - \boldsymbol{r}_2$, $\boldsymbol{r}_1 = (\mu/m_1)\boldsymbol{r}$ and $\boldsymbol{r}_2 = -(\mu/m_2)\boldsymbol{r}$. Note that $\ddot{r}^i = -(Gm/r^3)r^i(1 + \mathcal{O}(c^{-2}))$, which goes to zero as r approaches infinity. Expanding γ_a to next-to-leading order we get

$$\partial_t^l S^{ij,L} = \mu\left(s_{l+2} + \frac{1}{2}s_{l+4}\boldsymbol{\beta}^2 + \mathcal{O}(c^{-4})\right)l!v^{ijL}\,, \tag{6.9}$$

where $s_l = X_2^{l-1} + (-1)^l X_1^{l-1}$ and we define $X_1 = m_1/m$ and $X_2 = m_2/m$. We have $s_2 = 1$, $s_3 = \delta m/m$ and $s_4 = 1 - 3\eta$. We define the polarization projection tensors as

$$P_+^{ij} = \frac{1}{2}(p_i p_j - q_i q_j)\,, \tag{6.10}$$

$$P_\times^{ij} = \frac{1}{2}(p_i q_j + q_i p_j)\,. \tag{6.11}$$

Inserting all of this into (6.3) and only keeping terms to the desired order we get

$$\Delta h_{+,\times} = \frac{4G\mu}{c^4 R}\Delta\left(\left[1 + \frac{\delta m}{m}\boldsymbol{\beta}\cdot\boldsymbol{n} + (1-3\eta)\left(\frac{1}{2}\boldsymbol{\beta}^2 + (\boldsymbol{\beta}\cdot\boldsymbol{n})^2\right) + \mathcal{O}\left(\frac{1}{c^3}\right)\right]P_{+,\times}^{ij}v^i v^j\right)\,. \tag{6.12}$$

At early and late times we have $\boldsymbol{v} = \pm v_\infty(\cos(\pm\phi_\infty + \phi_0), \sin(\pm\phi_\infty + \phi_0), 0)$, where v_∞ is the velocity at infinity, ϕ_∞ is the angular difference between periapsis and initial direction and ϕ_0 is the angle between $\boldsymbol{e}_1$ and periapsis. Inserting this into (6.12) we get the following expressions for the linear memory:

$$\Delta h_{+,\times} = \frac{2G\mu}{c^2 R}\left(\frac{v_\infty}{c}\right)^2\left[\Delta h^0_{+,\times} + \frac{v_\infty}{c}\Delta h^1_{+,\times} + \frac{v_\infty^2}{c^2}\Delta h^2_{+,\times} + \mathcal{O}\left(\frac{1}{c^3}\right)\right]\,, \tag{6.13}$$

where the $\Delta h^i_{+,\times}$ are given by

$$\Delta h^0_+ = (1+C_\theta^2)\sin 2\phi_\infty \sin 2\phi_0\,, \tag{6.14}$$
$$\Delta h^0_\times = -2C_\theta \sin 2\phi_\infty \cos 2\phi_0\,, \tag{6.15}$$
$$\Delta h^1_+ = -\frac{\delta m}{m}\frac{S_\theta}{2}\Big\{(3C_\theta^2-1)\cos\phi_\infty\cos\phi_0 + (1+C_\theta^2)\cos 3\phi_\infty \cos 3\phi_0\Big\}\,, \tag{6.16}$$
$$\Delta h^1_\times = -\frac{\delta m}{m}S_\theta C_\theta\Big\{\cos\phi_\infty\sin\phi_0 + \cos 3\phi_\infty \sin 3\phi_0\Big\}\,, \tag{6.17}$$
$$\Delta h^2_+ = \frac{(1-3\eta)}{4}\Big\{2(1+C_\theta^2(1+2S_\theta^2))\sin 2\phi_\infty\sin 2\phi_0 + (1+C_\theta^2)S_\theta^2\sin 4\phi_\infty\sin 4\phi_0\Big\}\,, \tag{6.18}$$
$$\Delta h^2_\times = -\frac{(1-3\eta)}{2}C_\theta\Big\{2(1+S_\theta^2)\sin 2\phi_\infty\cos 2\phi_0 + S_\theta^2\sin 4\phi_\infty\cos 4\phi_0\Big\}\,. \tag{6.19}$$

6.2.4 The Liénard-Wiechert solution

We now give the general Liénard-Wiechert solution to the linearized Einstein equations (6.2) for a system of unbound particles. The energy-momentum tensor for such a system is similar to (6.7)

$$T^{\mu\nu}(t,\boldsymbol{x}) = \sum_A m_A\gamma_A v_A^\mu v_A^\nu \delta^{(3)}(\boldsymbol{x}-\boldsymbol{x}_A(t))\,. \tag{6.20}$$

The linear field equations can then be solved by the method of Green's function:

$$\bar h_{\mu\nu}(t,\boldsymbol{x}) = \frac{4G}{c^4}\int d^3x' \sum_A m_A\gamma_A v_A^\mu v_A^\nu \frac{\delta^{(3)}(\boldsymbol{x}'-\boldsymbol{x}_A(t'_r))}{|\boldsymbol{x}-\boldsymbol{x}'|}\,, \tag{6.21}$$

with the retarded time $t'_r(\boldsymbol{x}') = t - |\boldsymbol{x}-\boldsymbol{x}'|/c$. We evaluate the integral by multiplying with another delta function picking out the retarded time:

$$\bar h_{\mu\nu}(t,\boldsymbol{x}) = \frac{4G}{c^4}\int d^3x' \int d\tau \sum_A m_A\gamma_A v_A^\mu v_A^\nu \frac{\delta^{(3)}(\boldsymbol{x}'-\boldsymbol{x}_A(\tau))}{|\boldsymbol{x}-\boldsymbol{x}'|}\,\delta(\tau - t'_r(\boldsymbol{x}'))\,. \tag{6.22}$$

Changing the order of the integrals and integrating over d^3x' gives

$$\bar h_{\mu\nu}(t,\boldsymbol{x}) = \frac{4G}{c^4}\int d\tau \sum_A m_A\gamma_A v_A^\mu v_A^\nu \frac{\delta(\tau - t'_r(\boldsymbol{x}_A(\tau)))}{|\boldsymbol{x}-\boldsymbol{x}_A(\tau)|}\,. \tag{6.23}$$

This fixes the retarded time to $t'_r(\boldsymbol{x}_A(\tau)) = t - |\boldsymbol{x}-\boldsymbol{x}_A(\tau)|/c$. We integrate over $d\tau$ using the relation

$$\delta(\tau - t'_r(\boldsymbol{x}_A(\tau))) = \frac{\delta(\tau - t_r^A)}{1-\boldsymbol{\beta}_A\cdot\boldsymbol{n}}\,, \tag{6.24}$$

where t_r^A is the unique solution to the light cone equation $t_r^A = t - |\boldsymbol{x}-\boldsymbol{x}_A(t_r^A)|/c$. The general solution of (6.2) for a set of independently moving particles is then

$$\bar h_{\mu\nu}(t,\boldsymbol{x}) = \frac{4G}{c^4}\sum_A m_A\gamma_A v_A^\mu v_A^\nu \frac{1}{|\boldsymbol{x}-\boldsymbol{x}_A|}\frac{1}{1-\boldsymbol{\beta}_A\cdot\boldsymbol{n}}\Big|_{t_r^A}\,. \tag{6.25}$$

For the memory effect we are only interested in the field far away, so we set $1/|\boldsymbol{x}-\boldsymbol{x}_A| = 1/R + \mathcal{O}(1/R^2)$ and go to the transverse-traceless gauge. We get the general formula for the memory effect of unbound systems, found by Braginsky and Thorne in [78]:

$$\Delta h_{ij}^{TT} = \frac{4G}{c^4 R}\Delta\left(\sum_A \frac{m_A}{\sqrt{1-\boldsymbol{\beta}_A^2}}\left[\frac{v_A^i v_A^j}{1-\boldsymbol{\beta}_A\cdot\boldsymbol{n}}\right]^{TT}\right). \tag{6.26}$$

Expanding this equation for a binary system in orders of $\mathcal{O}(c^{-1})$ and using center-of-mass coordinates we get the low-velocity limit agreeing with (6.12).

6.3 Discussion

We now give some examples of the dependence of the memory effect on the parameter space of a binary system. We consider an hyperbolic encounter of a hypervelocity object with a supermassive black hole at a distance comparable to the distance to the galactic centre. Figure 6.2 shows the memory effect for $m_1 = 8M_\odot$, $m_2 = 4\times10^6 M_\odot$ and $v_\infty = 0.1c$ as a function of eccentricity e_ϕ.

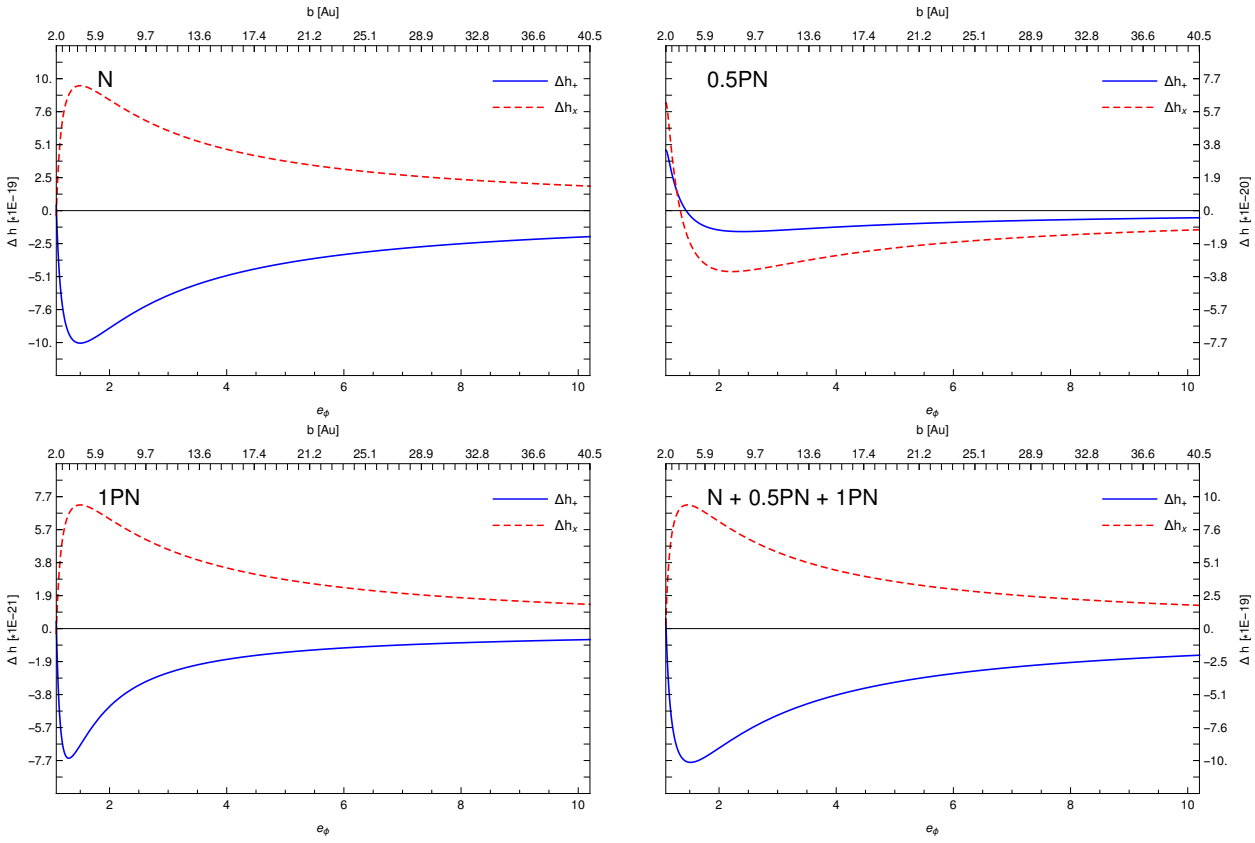

Figure 6.2: The linear memory in the polarization states at Newtonian, 0.5PN and 1PN order, as well as their sum, as a function of eccentricity e_ϕ, for $v_\infty = 0.1c$, $\theta = \pi/4$, $\phi_0 = \pi/8$, $m_1 = 8M_\odot$, $m_2 = 4\times10^6 M_\odot$ and $R = 8$kpc. The maximum at leading order corresponds to an angle of deflection of $\Delta\phi = \pi/2$, the zero point to $\Delta\phi = \pi$. For high eccentricities the memory tends to zero at all orders. As expected, the order of magnitude decreases by a factor of $v_\infty/c = 0.1$ per half post-Newtonian correction.

Our expressions for the memory effect (6.13 - 6.19) are correct up to first post-Newtonian order. The linear memory does not depend on the exact interactions between the two bodies during the encounter, but only on the initial and final state. Up to order $\mathcal{O}(c^{-2})$ these can be described by the velocity at infinity v_∞ and the angle between initial direction and periapsis ϕ_∞, related to the deflection angle by $\Delta\phi = 2\phi_\infty - \pi$. We relate the angle ϕ_∞ to the eccentricity e_ϕ and impact parameter b by use of the relations

$$\phi_\infty = \left(1 + \left(\frac{v_\infty}{c}\right)^2 \frac{3}{e_\phi^2 - 1} + \mathcal{O}(c^{-3})\right) \arccos\left(-\frac{1}{e_\phi}\right), \tag{6.27}$$

and

$$b = \frac{Gm}{v_\infty^2}\sqrt{e_\phi^2 - 1}\left(1 + \frac{v_\infty^2}{2c^2}\frac{1}{e_\phi^2 - 1}\left\{(e_\phi^2 - 1)(2 + 5\eta) + 6\right\} + \mathcal{O}(c^{-3})\right). \tag{6.28}$$

With $v_\infty = 0.1c$ these relations are starting to diverge for $e_\phi < 2$ and will not be exact for eccentricities close to 1. Because we are in a relativistic regime and the closest approach is only several Schwarzschild radii ($r_0 \sim 30 r_s$ at $b = 5\text{AU}$), there will be some small error even at higher eccentricities, but the general form of the memory as a function of e_ϕ is visible in Figure 6.2. To more accurately map ϕ_∞ to e_ϕ and b in this regime, we would have to include higher post-Newtonian corrections in (6.27) and (6.28). We see that we get a memory effect of order up to $\Delta h \sim 10^{-18}$ at a frequency of $v_0/r_0 \sim 10^{-4}$Hz, lying in the eLISA sensitivity range. Such a gravitational wave burst would in principle be observable, but the likelihood of a high velocity object encountering a supermassive black hole with small impact parameter might be very low. However even at high eccentricities of $e_\phi \sim 1000$ the memory effect is of order $\Delta h \sim 10^{-21}$, so we do not need high deflection angles to observe memory in such events.

Figure 6.3 shows the dependence of the leading-order term of the memory effect on the orientation of the orbital plane and the direction of periapsis.
We see that at leading order the memory has a maximum independent of the orientation of the system. With equations (6.14 - 6.15) we conclude that the strain is of order

$$\Delta h = \sqrt{\Delta h_+^2 + \Delta h_\times^2} \sim \frac{4G\mu}{c^2 R}\left(\frac{v_\infty}{c}\right)^2 \sin 2\phi_\infty\,. \tag{6.29}$$

For fixed initial velocity v_∞ there is a maximum in the memory effect at an angle $\phi_\infty = 3\pi/4$, corresponding to an angle of deflection of $\Delta\phi = \pi/2$ or an eccentricity of $e_\phi = \sqrt{2}$. This stems from the fact that the leading order term of the memory effect is proportional to the change in the second time derivative of the source quadrupole moment, which in a binary system is maximal at an angle of deflection of $\pi/2$. From equation (6.29) we also see that the magnitude of the memory effect scales with reduced mass, velocity and, given those, will be maximal if we have a deflection of $\pi/2$. To observe large memory we thus need high velocity encounters of massive objects with a strong deflection. For this to happen, the two object must approach each other up to a distance comparable to some orders of their Schwarzschild radius.
Note that the linear memory effect corresponds to a change in one of the multipole moment derivatives. By (6.9) those are given as $\partial_t^l S^{ij_L} \propto v^{ijL}$. In the case of parabolic motion we have $E = v_\infty = 0$ and all the terms in the multipole expansion (6.3) will be zero. The memory effect thus vanishes for parabolic orbits.

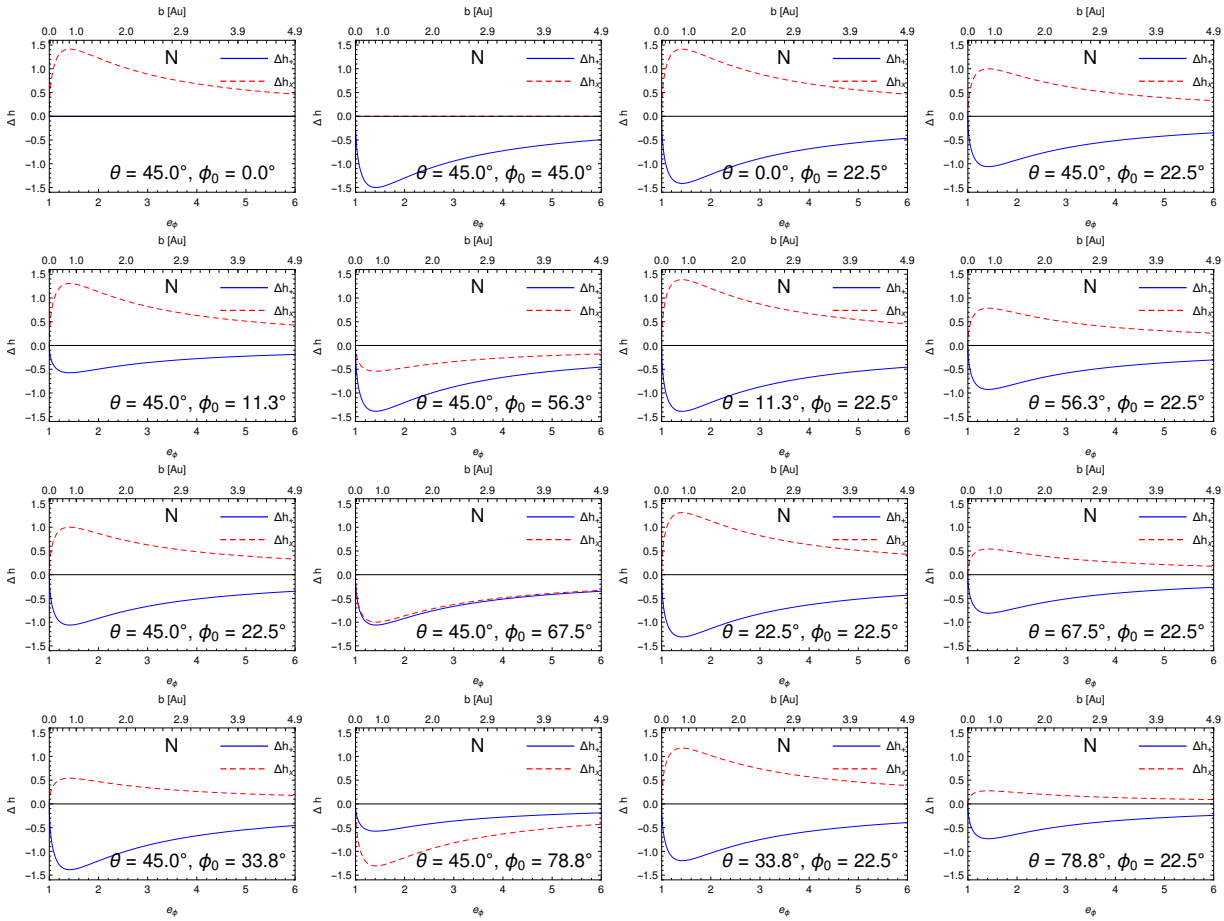

Figure 6.3: Dependence of the leading-order memory effect on the line-of-sight angle θ and periapsis angle ϕ_0. The employed scale factor is $G\mu/(c^2R)(v_\infty/c)^2 \sim 10^{-23}$ with $v_\infty = 150$km/s, $m_1 = 8M_\odot$, $m_2 = 13M_\odot$ and $R = 8$kpc. The orientation of the periapsis changes the amplitude of the different polarizations, while the line-of-sight angle changes the overall amplitude.

6.4 Conclusions

Linear memory is a measurable difference in the metric after the passing of a gravitational wave. It corresponds to a change in the time derivatives of the source multipole moments. For a hyperbolic binary system, these only depend on the velocity at infinity and the angle of deflection. Previously the contributions to the memory effect have only been explicitly calculated to leading order. Here we give expressions (6.13 - 6.19) correct up to first post-Newtonian order.

Observing linear memory from hyperbolic binaries will be very difficult. Stellar encounters in globular clusters might be frequent enough, however they produce memory below the range of sensitivity of eLISA. High velocity encounters between massive objects emitting gravitational Bremsstrahlung produce measurable linear memory even at high eccentricities, though the likelihood of such events is hard to estimate.

It is straightforward to give higher-order corrections to the memory effect. The expansion in (6.12) can easily be extended to orders beyond $\mathcal{O}(c^{-2})$, though one would have to be careful when using center-of-mass coordinates. In most physical systems the linear memory is already a minor effect and thus well described by leading order terms, so the usefulness of extending to higher orders is questionable. Additionally, we could extend our description of

the post-Newtonian motion of hyperbolic binaries to higher orders. This would allow for a more accurate mapping between ϕ_∞, e_ϕ and b at relativistic velocities. However, it does not change the expressions (6.13 - 6.19), as they are independent from the exact interaction during the encounter and only depend on the initial and final state. A qualitative treatment of the memory including spin-orbit coupling can be found in [2]. In this case however, the order of magnitude of the effect would be below the achieved observable threshold, as the spin contributions only enter at 1.5PN order.
Pulsar timing arrays measure gravitational waves on timescales of months to years and as such are sensitive to the long term changes in the metric from the memory effect, see e.g. [32]. Future advances of such surveys could be very interesting and may be the first way of observing the memory, though the most likely sources are mergers of supermassive black holes (SMBH) producing non-linear memory.

Acknowledgments

Y. Boetzel is supported by the Swiss National Science Foundation.

Chapter 7

Gravitational waveform for precessing eccentric comparable-mass binaries

A. Klein, L. De Vittori, Ph. Jetzer

This article is in preparation and yet to be published [4]

Abstract

We construct an inspiral gravitational waveform for spinnig eccentric comparable-mass binaries at the second post-Newtonian order. To do so, we use eccentricity as an expansion parameter. Our prescription is especially suitable for binaries moving along elliptic orbits with small eccentricities. Available waveform results are extended here with the addition of the quadrupole-monopole term as part of the spin-spin contribution to the phasing of the gravitational wave.

7.1 Introduction

In the study of gravitational waves and their sources we are approaching a new era. We expect that detections might start happening several times a year within the end of this decade. While of the detector side everything seems to be almost ready, we still have enough work in modelling gravitational waveforms, in order to be able to perform an accurate analysis of the detector output signal and a parameter estimation of the emitting sources. Most studies concerning gravitational wave radiation from binaries have focused on the case where the orbit is assumed to be circular. There is however evidence that orbits could be eccentric, as suggested by numerical simulations of the formation of binaries [83, 84]. Hence, to improve the accuracy of the waveform prediction, taking into account the effect of eccentricity is relevant. The same can be said of spins, playing an important role in the evolution of the dynamics of the source. In particular, spin-induced precession of the orbital plane can cause important variations in the wave amplitude and frequency, which shouldn't be neglected when constructing the waveform at higher post-Newtonian orders.

The evolution of a binary is commonly described in three phases: the inspiral part, the merger, and the ringdown. The merger and the ringdown phases are very difficult to model and, for the moment being, can only be described by numerical simulations. The inspiral part, however, a post-Newtonian description of the dynamics seems to be highly accurate comparison with Numerical Relativity are very satisfactory.

The post-Newtonian (PN) approximation [51, 85] consists of an expansion of the dynamics of the binary in v/c, and can be used while describing a system where the relative distance between the components is sufficiently large. Usually, the limit of its validity is considered to be the innermost stable circular orbit (ISCO), given by $r_{ISCO} = 6GM/c^2$. At least for circular orbits, comparison of the post-Newtonian waveforms with results from Numerical Relativity [86] seem to be very confident of the validity of this approximation until the end of the inspiral phase, just before merger of the components.

For the case under study in this work, where eccentricity is non-zero but is taken as an expansion parameter and thus assumed to be small, we can trust the validity of the same limit as in the circular case.

Previous works on the effect of spin in the evolution of binaries moving on eccentric orbits are available. In [87] the spin-orbit and spin-spin coupling correction terms were computed and added to previously available results, such as [61, 88]. In this work, as a further step in this task, we derive the evolution equations for the orbital parameters, in particular the eccentricity and the mean motion, up to full second post-Newtonian order in the phasing of the gravitational waves radiated from a binary source with comparable-mass components, including also the quadrupole-monopole term shown in [89].

We will only consider spin effects in the phasing of the wave, and will therefore need to take spin correction terms into account while computing the time derivative of the mean motion dn/dt , of the eccentricity de^2/dt , and consequently the periastron precession rate k.

Similarly to what has been done in [87], we also show a quasi-Keplerian parametrization of the eccentric orbit at full second post-Newtonian order, in such a way that it is divergence-free in the circular limit, where the eccentricity approaches zero.

7.2 Equations of motion

We can describe the orbit of a binary system in eccentric orbit using a post-Keplerian description of the dynamics. As starting point we use the 2PN description available in [87], with the addition of the monopole-quadrupole term present in [89–91]. We describe below how we derive the latter.

The reduced Lagrangian can be written as $\mathscr{L} = \mathscr{L}_N + \mathscr{L}_{SO} + \mathscr{L}_{SS} + \mathscr{L}_{QM}$, where the subscript N stays for Newtonian order, SO for the spin-orbit contributions to the Lagrangian, and where

$\mathscr{L}_{SS}$ contains the 2PN terms given in [87], while $\mathscr{L}_{QM}$ contains the quadrupole-monopole term.

$$\mathscr{L}_N = \frac{\dot{\boldsymbol{r}}^2}{2} + \frac{1}{r}\,, \tag{7.1}$$

$$\mathscr{L}_{SO} = \frac{1}{2}(\dot{\boldsymbol{r}} \times \boldsymbol{a}) \cdot \boldsymbol{\xi} - \frac{2}{r^3}(\boldsymbol{r} \times \dot{\boldsymbol{r}}) \cdot (\boldsymbol{\zeta} + \boldsymbol{\xi})\,, \tag{7.2}$$

$$\mathscr{L}_{SS} = \frac{1}{r^3}\boldsymbol{s}_1 \cdot \boldsymbol{s}_2 - \frac{3}{r^5}(\boldsymbol{r} \cdot \boldsymbol{s}_1)(\boldsymbol{r} \cdot \boldsymbol{s}_2)\,, \tag{7.3}$$

$$\mathscr{L}_{QM} = -\frac{1}{2r^3}\sum_i p_i \left[\boldsymbol{s}_i^2 - 3\,(\hat{\boldsymbol{r}} \cdot \boldsymbol{s}_i)^2\right]\,, \tag{7.4}$$

where $\boldsymbol{r}$ is the relative separation between the two compact masses m_1 and m_2, $\dot{\boldsymbol{r}}$ the velocity, $\boldsymbol{a}$ the acceleration, and $r = |\boldsymbol{r}|$ the distance. $\boldsymbol{s}_i = \boldsymbol{S}_i/m_i$ are the reduced spins, $\mu = m_1 m_2$ the reduced mass, $\boldsymbol{\zeta} = \boldsymbol{s}_1 + \boldsymbol{s}_2$, and $\boldsymbol{\xi} = \boldsymbol{s}_1 m_2/m_1 + \boldsymbol{s}_2 m_1/m_2$. Finally, p_i are quadrupole parameters defined so that $p_i = -1$ for a black hole. For simplicity, in this Chapter we will use a system of units where $G = c = m = 1$, where m denotes the total mass of the binary.

We consider here only the latter term in the Lagrangian, along with the Newtonian contribution, and can thus write it simply as [89, 90]

$$\mathscr{L} = \frac{\dot{\boldsymbol{r}}^2}{2} + \frac{1}{r} - \frac{1}{2r^3}\sum_i p_i \left[\boldsymbol{s}_i^2 - 3\,(\hat{\boldsymbol{r}} \cdot \boldsymbol{s}_i)^2\right]\,, \tag{7.5}$$

From this, we can deduce the reduced orbital energy and angular momentum:

$$\boldsymbol{L} = \boldsymbol{r} \times \boldsymbol{p} = \boldsymbol{r} \times \frac{\partial \mathscr{L}}{\partial \dot{\boldsymbol{r}}}\,, \tag{7.6}$$

$$E = \boldsymbol{p} \times \dot{\boldsymbol{r}} - \mathscr{L} = \frac{\partial \mathscr{L}}{\partial \dot{\boldsymbol{r}}} \times \dot{\boldsymbol{r}}\,, \tag{7.7}$$

and have therefore

$$\boldsymbol{L} = \boldsymbol{r} \times \dot{\boldsymbol{r}}\,, \tag{7.8}$$

$$E = \frac{\dot{\boldsymbol{r}}^2}{2} - \frac{1}{r} + \frac{1}{2r^3}\sum_i p_i \left[\boldsymbol{s}_i^2 - 3\,(\hat{\boldsymbol{r}} \cdot \boldsymbol{s}_i)^2\right]. \tag{7.9}$$

From the equations of precession [91], we get that the norm of the orbital angular momentum varies along an orbit as [92]

$$\begin{aligned} L(v) = \bar{L} + \frac{\mu}{4\bar{L}^3}\sum_i p_i \left|\hat{\boldsymbol{L}} \times \boldsymbol{s}_i\right|^2 [3e\cos(v - 2\psi_i) \\ + 3\cos(2v - 2\psi_i) + e\cos(3v - 2\psi_i)], \end{aligned} \tag{7.10}$$

where v is the true anomaly, $\bar{L}$ is the average norm of $\boldsymbol{L}$ with respect to v, e is the eccentricity, and ψ_i is the angle subtended by the periastron line and the projection of $\boldsymbol{s}_i$ in the orbital plane.

We can then write the following quasi-Keplerian parametrization of the orbit:

$$\boldsymbol{r} = r(\cos\phi, \sin\phi, 0)\,, \tag{7.11}$$
$$r = a(1 - e_r \cos u) + \sum_i f_r^i \cos(2v - 2\psi_i)\,, \tag{7.12}$$
$$l = n(t - t_0) = u - e_t \sin u\,, \tag{7.13}$$
$$\phi = (1+k)v + \sum_i \left[f_{\phi,1}^i \sin(v - 2\psi_i) + f_{\phi,2}^i \sin(2v - 2\psi_i) \right]\,, \tag{7.14}$$
$$v = 2\arctan\left(\sqrt{\frac{1+e_\phi}{1-e_\phi}} \tan\frac{u}{2} \right)\,, \tag{7.15}$$

where a is the semimajor axis, u is the eccentric anomaly, l is the mean anomaly, n is the mean motion, k is the periastron precession rate per orbit, e_t, e_r, and e_ϕ are eccentricity parameters, and the f_r^i and $f_{\phi,j}^i$ are coupling constants.

In terms of the post-Newtonian parameter ζ and the eccentricity parameter e, the constants in the above quasi-Keplerian parametrization are given by

$$n = \zeta^3\,, \tag{7.16}$$
$$e_t = e\,, \tag{7.17}$$
$$a = \zeta^{-2}\left(1 + \frac{\gamma_1}{4(1-e^2)}\zeta^4 \right)\,, \tag{7.18}$$
$$k = -\frac{3\gamma_1}{4(1-e^2)^2}\zeta^4\,, \tag{7.19}$$
$$e_r = e\left(1 - \frac{\gamma_1}{4(1-e^2)}\zeta^4 \right)\,, \tag{7.20}$$
$$e_\phi = e\left(1 - \frac{\gamma_1}{2(1-e^2)}\zeta^4 \right)\,, \tag{7.21}$$
$$f_r^i = -\frac{\gamma_2^i}{4}\zeta^2\,, \tag{7.22}$$
$$f_{\phi,1} = -\frac{e\gamma_2^i}{2(1-e^2)^2}\zeta^4\,, \tag{7.23}$$
$$f_{\phi,2} = -\frac{\gamma_2^i}{8(1-e^2)^2}\zeta^4\,, \tag{7.24}$$
$$E = -\frac{\zeta^2}{2}\,, \tag{7.25}$$
$$\bar{L} = \frac{\sqrt{1-e^2}}{\zeta}\left(1 - \frac{\gamma_1}{4(1-e^2)^2}\zeta^4 \right)\,, \tag{7.26}$$
$$\gamma_1 = -\sum_i p_i \left[\boldsymbol{s}_i^2 - 3\left(\hat{\boldsymbol{L}} \cdot \boldsymbol{s}_i \right)^2 \right]\,, \tag{7.27}$$
$$\gamma_2^i = -p_i \left| \hat{\boldsymbol{L}} \times \boldsymbol{s}_i \right|^2\,. \tag{7.28}$$

The evolution of of ζ and e under radiation reaction can be determined from [89]. We find

$$\frac{d\zeta}{dt} = \frac{96+292\,e^2+37\,e^4}{15\,(1-e^2)^{7/2}}\,\nu\,\zeta^9 + \frac{\nu\,\zeta^{13}}{60\,(1-e^2)^{11/2}}\,\times\,\Big[\big(1344+7768\,e^2 \\ +4368\,e^4+177\,e^6\big)\big(\sigma_7+3\sigma_8\big)+2e^2\big(4104+3994e^2+237e^4\big)\sigma_9\Big]\,, \tag{7.29}$$

$$\frac{de^2}{dt} = \frac{-\,2e^2\big(304+121\,e^2\big)}{15\,(1-e^2)^{5/2}}\,\nu\,\zeta^8 - \frac{\nu\,e^2\,\zeta^{12}}{30\,(1-e^2)^{9/2}}\,\times\,\Big[\big(6184+6918\,e^2 \\ +555\,e^4\big)\big(\sigma_7+3\sigma_8\big)+2\big(2763+5056\,e^2+516\,e^4\big)\sigma_9\Big]\,, \tag{7.30}$$

where the σ_i coefficients in the quadrupole-monopole correction term are given by

$$\sigma_7 = \sum_i p_i \boldsymbol{s}_i^2\,, \tag{7.31}$$

$$\sigma_8 = \sum_i -p_i\left(\hat{\boldsymbol{L}}\cdot\boldsymbol{s}_i\right)^2\,, \tag{7.32}$$

$$\sigma_9 = \sum_i p_i\left|\hat{\boldsymbol{L}}\times\boldsymbol{s}_i\right|^2\cos 2\psi_i\,. \tag{7.33}$$

From (7.29) and (7.30) one could also derive the energy and angular momentum loss of the binary. For further analysis of the behaviour of the eccentricity all along the interaction, as well as for the full derivation of the waveform, with use of the stationary phase approximation, we refer to the complete paper [4], which at the time of writing is yet to be published.

7.3 Full post-Keplerian parametrization

We decide to express the waveform in terms of the PN parameter

$$z = \frac{\zeta}{\sqrt{1-e^2}}(1+k)^{1/3}\,. \tag{7.34}$$

This choice satisfies $\lim_{e\to 0} z = \omega^{1/3}$, where ω is the orbital frequency in the circular limit. This makes it a generalization to eccentric systems of the TaylorT4 phasing, while a parametrization based upon ζ is not. In addition, the factor $\sqrt{1-e^2}$ simplifies in many expressions.

The result in (7.29) and (7.30) can be combined with the result of [87] to yield the 2PN spin-spin radiation reaction effects for eccentric orbits. In the following we show the orbital parametrization and radiation reaction at full second post-Newtonian order.

In terms of the parameter z, the reduced orbital energy E and angular momentum L are given

by

$$
\begin{aligned}
E = &-\frac{\left(1-e^2\right)}{2}\,z^2\left\{1+\left[-\frac{3}{4}-\frac{\nu}{12}+\left(-\frac{5}{4}+\frac{\nu}{12}\right)e^2\right]z^2+\left[-\frac{67}{8}+\frac{35\,\nu}{8}-\frac{\nu^2}{24}\right.\right.\\
&+\left(-\frac{19}{4}+\frac{21\,\nu}{4}+\frac{\nu^2}{12}\right)e^2+\left(\frac{5}{8}-\frac{5\,\nu}{8}-\frac{\nu^2}{24}\right)e^4+\left(1-e^2\right)^{3/2}(5-2\,\nu)\Big]z^4\\
&+\left\{-\frac{835}{64}+\left(\frac{18319}{192}-\frac{41\pi^2}{16}\right)\nu-\frac{169\,\nu^2}{32}-\frac{35\,\nu^3}{5184}+\left[-\frac{3703}{64}+\left(\frac{21235}{192}-\frac{41\pi^2}{64}\right)\nu\right.\right.\\
&\left.-\frac{7733\;\nu^2}{288}+\frac{35\;\nu^3}{1728}\right]e^2+\left(\frac{103}{64}-\frac{547\;\nu}{192}-\frac{1355\;\nu^2}{288}-\frac{35\;\nu^3}{1728}\right)e^4\\
&+\left(\frac{185}{192}+\frac{75\;\nu}{64}+\frac{25\;\nu^2}{288}+\frac{35\;\nu^3}{5184}\right)e^6+\sqrt{1-e^2}\left\{\frac{5}{2}+\left(-\frac{641}{18}+\frac{41\pi^2}{96}\right)\nu\right.\\
&\left.\left.\left.+\left[-35+\left(\frac{394}{9}-\frac{41\pi^2}{96}\right)\nu-\frac{\nu^2}{3}\right]e^2+\left(\frac{5}{2}+\frac{23\,\nu}{6}-\frac{10\,\nu^2}{3}\right)e^4\right\}\right\}z^6\right\}, \qquad (7.35)
\end{aligned}
$$

$$
\begin{aligned}
L = &\;z^{-1}\left\{1+\left[\frac{3}{2}+\frac{\nu}{6}+\left(-\frac{3}{2}+\frac{5\,\nu}{6}\right)e^2\right]z^2+\left[\frac{47}{8}-\frac{27\,\nu}{8}+\frac{\nu^2}{24}+\left(\frac{21}{4}-\frac{5\,\nu}{6}-\frac{3\,\nu^2}{4}\right)e^2\right.\right.\\
&+\left(\frac{11}{8}-\frac{73\,\nu}{24}+\frac{5\,\nu^2}{24}\right)e^4-\sqrt{1-e^2}\left(1+2e^2\right)(5-2\,\nu)\Big]z^4+\left\{\frac{155}{16}+\left(-\frac{3151}{48}\right.\right.\\
&\left.+\frac{123\pi^2}{64}\right)\nu+\frac{25\,\nu^2}{8}+\frac{7\,\nu^3}{1296}+\left[\frac{1227}{16}+\left(-\frac{265}{2}+\frac{119\pi^2}{128}\right)\nu+\frac{787\,\nu^2}{36}+\frac{95\,\nu^3}{432}\right]e^2\\
&+\left(\frac{169}{16}-\frac{115\,\nu}{6}+\frac{109\,\nu^2}{9}+\frac{127\,\nu^3}{432}\right)e^4+\left(\frac{13}{48}+\frac{283\,\nu}{48}-\frac{71\,\nu^2}{36}-\frac{25\,\nu^3}{1296}\right)e^6\\
&+\sqrt{1-e^2}\left\{-\frac{5}{4}+\left(\frac{641}{36}-\frac{41\;\pi^2}{192}\right)\nu-\frac{11\;\nu^2}{6}\right.\\
&\left.\left.\left.+\left[-\frac{135}{4}+\left(\frac{2359}{36}-\frac{41\pi^2}{96}\right)\nu-\frac{34\;\nu^2}{3}\right]e^2+\left(5-\frac{14\,\nu}{3}-\frac{\nu^2}{3}\right)e^4\right\}\right\}z^6\right\}. \qquad (7.36)
\end{aligned}
$$

The quasi-Keplerian parametrization of the orbit at full 2PN order is then given by

$$\boldsymbol{r} = r(\cos\phi, \sin\phi, 0)\,, \qquad (7.37)$$

$$r = a(1-e_r\cos u) + \sum_i f_r^i \cos(2v - 2\psi_i)\,, \qquad (7.38)$$

$$l = n(t-t_0) = u - e_t\sin u + g_t(v-u) + h_{t,1}\sin v + h_{t,2}\sin 2v + h_{t,3}\sin 3v\,, \qquad (7.39)$$

$$
\begin{aligned}
\phi = &\,(1+k)\,v + \sum_i \left[\, f^i_{\phi,1}\,\sin(v-2\psi_i) \,+\, f^i_{\phi,2}\,\sin(2v-2\psi_i)\,\right]\\
&+\, h_{\phi,2}\,\sin 2v \,+\, h_{\phi,3}\,\sin 3v \,+\, h_{\phi,4}\,\sin 4v \,+\, h_{\phi,5}\,\sin 5v\,, \qquad (7.40)
\end{aligned}
$$

$$v = 2\arctan\left(\sqrt{\frac{1+e_\phi}{1-e_\phi}}\tan\frac{u}{2}\right), \qquad (7.41)$$

where the coefficients in terms of the eccentricity e and the parameter z read

$$
\begin{aligned}
a = \; & \frac{z^{-2}}{(1-e^2)}\Bigg\{1+\left[-1+\frac{\nu}{3}+\left(3-\frac{\nu}{3}\right)e^2\right]z^2 \; +\left[\frac{19}{4}-\frac{7\nu}{8}+\frac{\nu^2}{8}+\left(\frac{43}{4}-\frac{55\nu}{6}-\frac{2\nu^2}{9}\right)e^2\right. \\
& \left.+\left(1+\frac{25\nu}{24}+\frac{\nu^2}{9}\right)e^4-\left(1-e^2\right)^{3/2}(5-2\nu)\right]z^4+\left\{\frac{39}{4}+\left(-\frac{785}{16}+\frac{83\pi^2}{64}\right)\nu+\frac{11\nu^2}{6}\right. \\
& +\frac{2\nu^3}{81}+\left[87+\left(\frac{1853}{12}+\frac{123\pi^2}{64}\right)\nu+\frac{205\nu^2}{9}-\frac{2\nu^3}{27}\right]e^2 \; +\left[\frac{121}{4}+\left(-\frac{1739}{48}-\frac{\pi^2}{64}\right)\nu\right. \\
& \left.+\frac{439\nu^2}{36}+\frac{2\nu^3}{27}\right]e^4+\left(-\frac{2}{3}-\frac{5\nu}{8}-\frac{\nu^2}{18}-\frac{2\nu^3}{81}\right)e^6+\sqrt{1-e^2}\left\{-10+\left(\frac{340}{9}-\frac{41\pi^2}{96}\right)\nu\right. \\
& \left.\left.-\frac{10\nu^2}{3}+\left[30+\left(-\frac{361}{9}+\frac{41\pi^2}{96}\right)\nu-\frac{\nu^2}{3}\right]e^2+\left(10-\frac{29\nu}{3}+\frac{11\nu^2}{3}\right)e^4\right\}\right\}z^6\Bigg\}\,, \qquad (7.42)
\end{aligned}
$$

$$
e_t^2 = \; e^2\,, \qquad (7.43)
$$

$$
\begin{aligned}
e_r^2 = \; & e^2 \; + \; e^2\left(1-e^2\right)\Bigg\{(8-3\nu)\;z^2+\left[\frac{65}{2}-\frac{95\nu}{3}+4\nu^2+\left(-40+\frac{193\nu}{6}-4\nu^2\right)e^2\right. \\
& \left.+\sqrt{1-e^2}\;(15-6\nu)\right]z^4 \; +\left\{\;77+\left(-\frac{825}{4}+\frac{81\pi^2}{32}\right)\nu+\frac{613\;\nu^2}{12}-3\;\nu^3\right. \\
& +\left[-287+\left(\frac{2975}{8}-\frac{\pi^2}{32}\right)\nu-\frac{233\nu^2}{2}+6\nu^3\right]e^2+\left(160-\frac{1621\nu}{8}+\frac{689\nu^2}{12}-3\nu^3\right)e^4 \\
& \left.+\sqrt{1-e^2}\left[190+\left(-\frac{712}{3}+\frac{41\pi^2}{32}\right)\nu+34\nu^2-\left(130-95\nu+13\nu^2\right)e^2\right]\right\}z^6\Bigg\}\,, \qquad (7.44)
\end{aligned}
$$

$$
\begin{aligned}
e_\phi^2 = \; & e^2 \; + \; e^2\left(1-e^2\right)\Bigg\{(8-2\nu)\;z^2+\left[41-\frac{80\nu}{3}+\frac{11\nu^2}{12}-\left(40-\frac{65\nu}{3}+\frac{89\nu^2}{48}\right)e^2\right. \\
& \left.+\sqrt{1-e^2}(15-6\nu)\right]z^4 \; +\left\{202+\left(-\frac{3369}{8}+\frac{251\pi^2}{32}\right)\nu+\frac{79\nu^2}{2}+\frac{\nu^3}{12}\right. \\
& -\left[346-\left(\frac{8581}{32}+\frac{\pi^2}{128}\right)\nu+46\nu^2-\frac{209\nu^3}{96}\right]e^2+\left(160-\frac{547\nu}{4}+\frac{109\nu^2}{4}-\frac{179\nu^3}{192}\right)e^4 \\
& \left.+\sqrt{1-e^2}\left[190+\left(-\frac{652}{3}+\frac{41\pi^2}{32}\right)\nu+26\nu^2-\left(130-75\nu+5\nu^2\right)\;e^2\right]\right\}z^6\Bigg\}\,, \qquad (7.45)
\end{aligned}
$$

$$
\begin{aligned}
n = \; & \left(1-e^2\right)^{3/2}\;z^3\Bigg\{\;1-\;3\;z^2\;+\left[-\frac{9}{2}+7\nu+\left(-\frac{51}{4}+\frac{13\nu}{2}\right)\;e^2\;\right]z^4 \\
& +\left\{\;\frac{3}{2}+\left(\frac{457}{4}-\frac{123\pi^2}{32}\right)\nu-7\nu^2+\left[-\frac{261}{4}+\left(165-\frac{123\pi^2}{128}\right)\nu-40\nu^2\right]e^2\right. \\
& \left.+\left(-\frac{39}{2}+\frac{55\nu}{4}-\frac{65\nu^2}{8}\right)\;e^4\;-\;3\sqrt{1-e^2}\;\left(1+2e^2\right)(5-2\nu)\right\}z^6\Bigg\}\,, \qquad (7.46)
\end{aligned}
$$

$$
\begin{aligned}
k = \; & 3\;z^2+\left[\frac{27}{2}-7\nu+\left(\frac{51}{4}-\frac{13\nu}{2}\right)\;e^2\;\right]z^4 \; +\left\{\frac{105}{2}+\left(-\frac{625}{4}+\frac{123\pi^2}{32}\right)\nu\right. \\
& +7\;\nu^2+\;\left[\;\frac{567}{4}+\left(-204+\frac{123\;\pi^2}{128}\right)\;\nu+40\;\nu^2\;\right]e^2 \\
& \left.+\left(\frac{39}{2}-\frac{55\nu}{4}+\frac{65\nu^2}{8}\right)\;e^4\;+\;3\sqrt{1-e^2}\;\left(1+2e^2\right)(5-2\nu)\right\}z^6\,, \qquad (7.47)
\end{aligned}
$$

$$g_t = \left(1-e^2\right)^{3/2}\left\{\left(\frac{15}{2}-3\nu\right)z^4 + \left[15+\left(-\frac{170}{3}+\frac{41\pi^2}{64}\right)\nu+5\nu^2+\left(15-\frac{29\nu}{2}+\frac{11\nu^2}{2}\right)\right]z^6\right\}, \tag{7.48}$$

$$h_{t,1} = e\left(1-e^2\right)^{3/2}\left\{\left(-\frac{\nu}{2}-\frac{\nu^2}{8}\right)z^4 + \left[9+\left(\frac{977}{48}+\frac{\pi^2}{64}\right)\nu+\frac{23\nu^2}{6}-\frac{\nu^3}{24}+\left(\frac{\nu}{4}+\frac{\nu^2}{6}+\frac{65\nu^3}{192}\right)e^2\right]z^6\right\}, \tag{7.49}$$

$$h_{t,2} = e^2\left(1-e^2\right)^{3/2}\left(\frac{23\nu}{32}+\frac{3\nu^2}{8}+\frac{3\nu^3}{16}\right)z^6, \tag{7.50}$$

$$h_{t,3} = e^3\left(1-e^2\right)^{3/2}\frac{13\nu^3}{6}z^6, \tag{7.51}$$

$$h_{\phi,2} = e^2\left\{\left(\frac{\nu}{8}-\frac{3\nu^2}{8}\right)z^4 + \left[1-\left(\frac{31}{8}+\frac{49\pi^2}{256}\right)\nu-\frac{79\nu^2}{48}+\frac{3\nu^3}{8}+\left(\frac{3\nu}{64}-\frac{71\nu^2}{48}+\frac{31\nu^3}{32}\right)e^2\right]z^6\right\}, \tag{7.52}$$

$$h_{\phi,3} = e^3\left\{-\frac{3\nu^2}{32}z^4 + \left[\frac{55\nu}{192}+\left(-\frac{5}{32}+\frac{\pi^2}{256}\right)\nu^2+\frac{17\nu^3}{64}+\frac{43\nu^3}{256}e^2\right]z^6\right\}, \tag{7.53}$$

$$h_{\phi,4} = e^4\left(\frac{5\nu}{128}+\frac{7\nu^2}{32}+\frac{5\nu^3}{64}\right)z^6, \tag{7.54}$$

$$h_{\phi,5} = e^5\frac{5\nu^3}{256}z^6. \tag{7.55}$$

7.4 Conclusions

In this paper we reach the full second post-Newtonian order description of a spinning binary on eccentric orbits with comparable-mass components. We add to previously available results of spin-orbit and spin-spin coupling the quadrupole-monopole correction term, at the same PN order as the spin-spin term and therefore relevant for generating accurate waveform templates. Our parametrization is valid for arbitrary spins, and being free of divergencies in the circular limit, where $e \to 0$, can be compared to the several works on quasi-circular binaries, such as [93, 94], where one can see the difference between waveforms where spin was neglected or taken into account, respectively.

Since we base our calculations on an expansion in terms of the eccentricity, our prescription is especially suitable for binaries orbiting on elliptic trajectories with small eccentricities.

Acknowledgments

A. Klein is supported by NSF Career Grant No. PHY-1055103. L. De Vittori was supported by the Swiss National Science Foundation during his stay at the University of Mississippi at an important stage in the development of this work.

Chapter 8

Conclusions

"Gravitational wave detectors will soon bring us observational maps of black holes colliding. Supercomputer simulations will attempt to replicate the symphonies and tell us what they mean, and black holes thereby will become the objects of detailed scrutiny. What will that scrutiny teach us?
There will be surprises."

Kip S. Thorne

At the time this work is being written, much progress towards first detections of gravitational waves is under way. Advanced LIGO [30] just went for the first time in observation mode (O1) in these weeks, starting its first science run, with a range of about 70 Mpc, covering a frequency band from 10 to 1000 Hz, after a 7 year long major upgrade. Within a year time, advanced LIGO – by then also joined by a smaller franco-italian detector near Pisa, called Virgo (see [24]), currently undergoing an own upgrade – will reach an average observation range of 120 Mpc, which corresponds to 326 million light years, a volume around 1000 times bigger than in initial LIGO.
Detection rate estimates are very difficult by now. The LIGO Science Collaboration expects to reach design sensitivity within the next five years. Some predictions talk about tens of binary neutron stars a year, but this number could easily increase from one science run to the next while the fine tuning of the detector gets better and better.

At the same time, LISA [31] is taking its first important steps into space preparing the launch of a test satellite, the LISA Pathfinder, aiming to test the technology of LISA-like detectors. Launch is expected to occur in late autumn 2015 in Kourou, French Guiana. Positive results from the LISA Pathfinder mission would be the definitive green light for the eLISA gravitational wave observer.

Having both ground and space based detectors working – and with the addition of Pulsar Time Array surveys, such as NANOGrav, or new ground-based detectors such as KAGRA, in Japan or the futuristic third generation European proposed detector Einstein Telescope – would mean being able to perform true gravitational wave astronomy on a regular basis, capturing signals at different frequencies and luminosities, and to make very accurate parameter estimation of the radiating sources. The universe we have only been looking at with the eyes of electromagnetic waves, will be visible through new eyes, not only allowing to understand the physics of complex systems and strong gravitational fields, but also unveiling new kind of sources that

we might don't expect and remain unpredictable and unknown so far.

Building detectors and running them properly, however, isn't enough for real gravitational wave astronomy to be carried on. A key role in this process is a right understanding of the physics inside the source and in particular an accurate knowledge of the expected wave signal emitted from any possible source. In order to be able to extract a gravitational wave signal from the noisy detector output, where the signal–to–noise is estimated to be pretty low, requires therefore a very complete database of waveform templates. Numerical methods, such as matched filtering, can then be applied when comparing the output signal with possible waveforms and looking for high correlation between them, finalizing thus the long process of detection.

In this work we devoted our attention especially to this task: improving available waveforms, as well as prescriptions to generate them. We focused on two particular cases of radiating sources: unbound collisions between compact bodies, such as black holes or neutron stars, and binary systems moving along elliptic orbits. In the latter, as a further step with respect to the numerous available results, we improved the precision of the waveform templates by adding a new correction term in the dynamics of the spin-precessing binary at the second post-Newtonian order and using a more suitable quasi-Keplerian parametrization allowing comparison with the circular limit, being free of divergence for eccentricities approaching zero.

In the case of unbound collision, commonly referred to as hyperbolic encounters, we provided a new prescription in order to generate waveforms for arbitrarily spinning compact binaries up to 1.5 post-Newtonian order, but including higher order radiation reaction effects. In the very interesting and not well-known hyperbolic case, we study the presence and behaviour of the memory effect, predicted by Zel'dovich, Polnarev, Braginsky, Grishchuk and Thorne [64, 78, 79]. The memory arises from a change in the second time derivative of the source's quadrupole moment. It is a linear effect, and refers to the fact that the strain amplitude $h_{ij}(t)$ does not vanish at infinity but rather stays constant at a non-zero value for all times. Gravitational waves usually don't show this asymmetry, and once the interaction or the inspiral, merger and ringdown of a binary has ended, the perturbation disappears and the metric gets back to its initial state. In the normal case then physical distances between test masses are the same before and after the passage of the gravitational wave. However, if there is some asymmetry during the interaction (in particular if the second derivative of the quadrupole moment varies), the physical distance between test masses can be different after the perturbation has passed. We speak therefore of a "memory", because the imprint of the gravitational wave remains as a mark on the metric.
We notice here that a description in the TT frame would give a vanishing *coordinate difference*, since masses initially at rest stay at rest even during the passage of the wave. Instead, looking at the invariant length element ds^2 one can understand that *physical distances* must change in the presence of memory. We recall from (3.43) that the length element in the case of an incoming gravitational wave travelling along the z direction is given by

$$ds^2 \;=\; -c^2dt^2 \;+\; [1+h_+(t)]\;dx^2 \;+\; [1-h_+(t)]\;dy^2 \;+\; dz^2\,. \tag{8.1}$$

Now it is straightforward to see that a non-vanishing h_+ or $h_\times$ at late times means that the physical distance has to be different than before the interaction had occurred. Hence, in the proper detector frame one would also see a change in coordinate distance.
Notice that, according to equation (2.41), in the proper detector frame one can describe the

action of a gravitational wave as a Newtonian force acting on a test mass

$$F^i = \frac{m}{2} \ddot{h}^{TT}_{ij} \xi^j \ . \tag{8.2}$$

The strength of the force depends on the *second* derivative of the strain h. Thus, a non-zero but constant value for h at infinity means that the test masses cannot have a residual velocity, even in presence of the memory effect.

In Figure 8.1 we sketch how a gravitational wave with memory would act onto two test masses initially at rest.

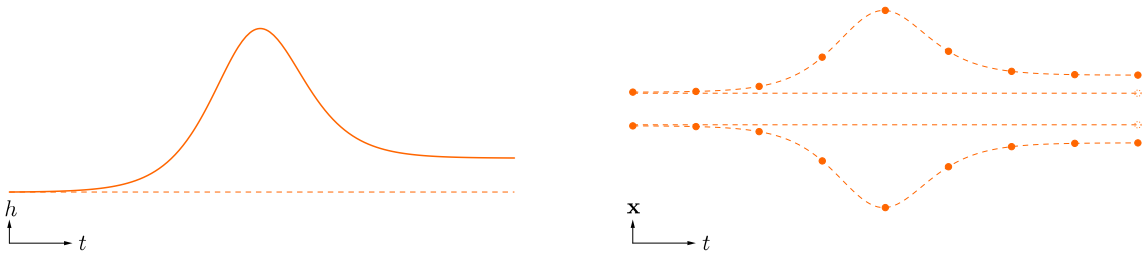

Figure 8.1: On the left we plot a possible signal of an incoming gravitational wave. On the right we sketch how two test masses would behave through the interaction with the perturbation. If the signal presents some memory the test masses do not turn back to their original distance.

As the authors in [95] review, this effect was believed to be very small and almost negligible. Later in 1991, Christodoulou discovered the presence of a non-linear memory effect [81], which increases during a closed interaction and builds up quickly at every orbit reaching significant size to be detected even in ground-based interferometers. However, while in the linear memory the fields do not reach null infinity, the non-linear contribution do and thus don't last after the end of the interaction.
It is very difficult to predict how detectable gravitational memory is. According to the study in [62] and [95], it seems reasonable to think that the size of memory itself shouldn't be weaker than other aspects of gravitational waves (recall that in Chapter 5 we noticed that memory already appears at leading order in the waveform). However, due to the present techniques of waveform extraction, through matched filtering, and because of the seismic noise at low frequencies in ground-based detectors, first direct observations of the memory effect are likely to happen in Pulsar Timing Arrays [96], where the sensitivity at low frequencies is much higher than LIGO and even proposed LISA-like space-born detectors.

Throughout this work there is a recurring aspect arising anytime we consider a prescription for generating waveforms: the importance of taking into account as many parameters as possible affecting the dynamics and making the motion different than the standard non-spinning, equal-mass, circular case. Those parameters, such as eccentricity, spin or mass ratio, generate non-negligible correction terms, which can change dramatically the shape of the waveform.
It is therefore desirable to continue this common effort, going to higher post-Newtonian order in the dynamics and raising the order of the multipole expansion while computing the polarization states. All these side effects increase the structure of the waveform, allowing a much better parameter estimation of the source. It is only by carrying on this task that real gravitational wave astronomy will be possible in the near future.

It is through the joint effort of running improved high precision detectors and studying with an enhanced theoretical framework the sources, their dynamics, and the radiated waveforms that we will soon be able to decode the symphonies being played all over the universe.

Appendices

Appendix A

Waveform comparison

In this Appendix we briefly show some sets of waveform templates for the case of an unbound compact binary collision, for both the spinning and the non-spinning case. The wave signals are generated with the prescription described extensively in Chapter 5.
By comparing them to each other one may appreciate the impact on some of the encounter parameters on the gravitational wave, as well as the sensible difference between spinning and non-spinning binaries, mostly due to the precession of the orbital plane. From this plots one can also notice the presence of a remarkable memory effect in some special situations.

In Figures A.1 and A.2 we display the waveform for a hyperbolic encounter with minimal radius of about $r_{min} = 1.9 \times 10^9$ m, for comparison with results in [48] and [52], considering non-spinning and spinning binary components, respectively. The waveform is plotted for different eccentricities, so that one can appreciate how the interaction gets weaker while increasing e_t, and therefore the amplitude decreases significantly. Also, one can see the influence of the mass ratio on the waveform. In the non-spinning case, the mass only appears as a total scaling factor, and doesn't really contribute to the shape of the phasing. However, in the case where the binary is spinning, the mass distribution plays a key role in the precession of the orbital plane and of the spins themselves. As a result, the structure of the signal varies consistently.

In Figures A.3 and A.4 we show a few waveform templates for binaries with fixed mass ratio $q = 4$, again for both the non-spinning and the spinning case, respectively. The varying parameter is here the inclination angle θ of the orbital plane with respect to the observer line–of–sight. We show the signal for three different values of e_t. Since the structure and the phasing of the gravitational wave remains the same for any angle, the observer doesn't loose any information about the source, except in the case where he sees the interaction edge-on. On the other hand, this behaviour reveals a non-obvious degeneracy while decoding a hypothetical signal from a detector, since a change in the amplitude of the wave could also mean a different position in sky of the source. In order to break this degeneracy one would need a detector network able to point out the source. This is currently being done for Earth-based detectors, with the LIGO-Virgo collaboration, and we expect other detectors soon to be able to joint this common effort.

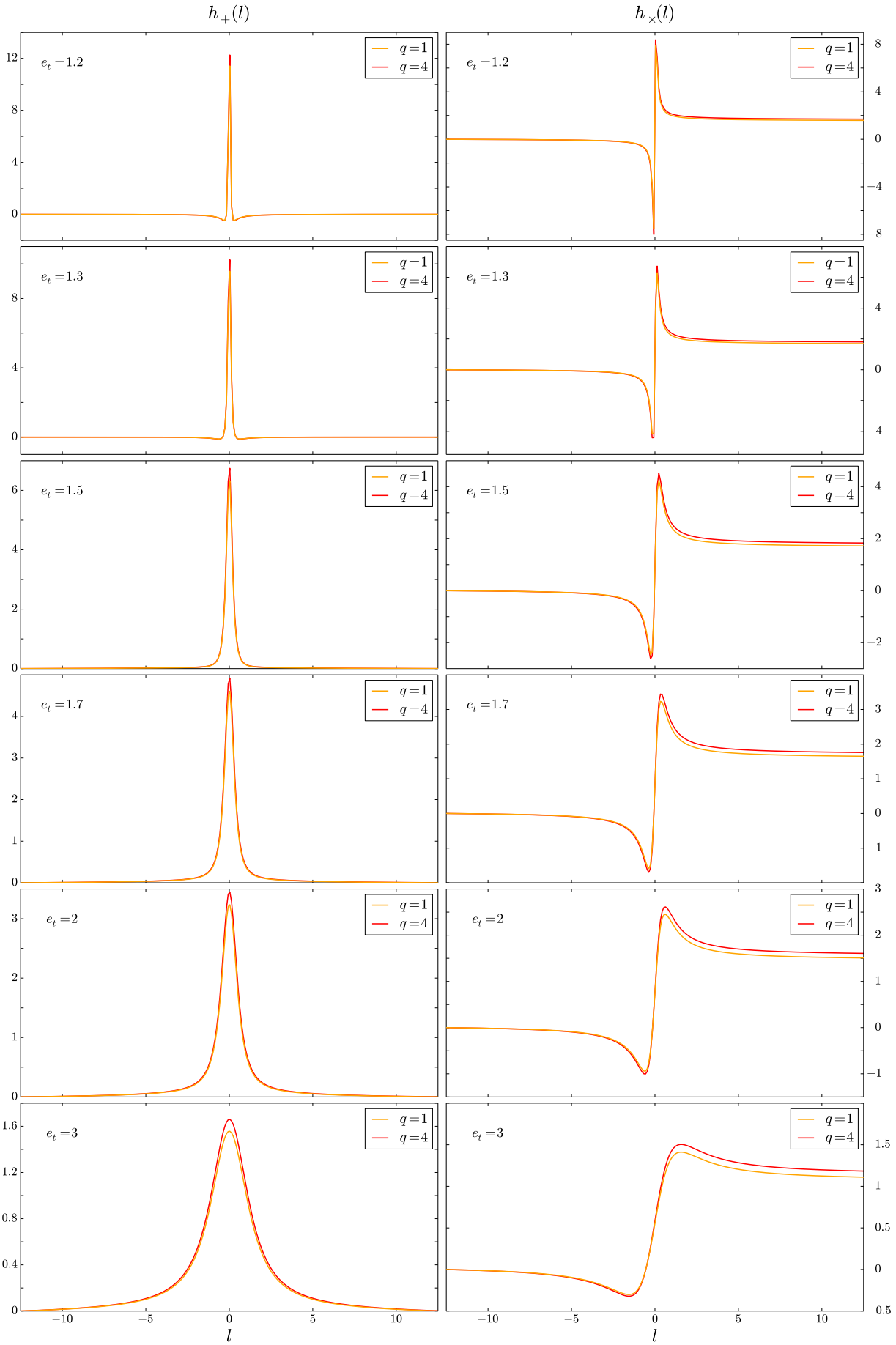

Figure A.1: Non-spinning waveform with both dynamics and polarization states at 1PN order, with $r_{min} \sim 1.9 \times 10^9$ m, $\phi_0 = 0°$, $\theta = 45°$, for $q = 1, 4$ and e_t ranging from 1.2 to 3.

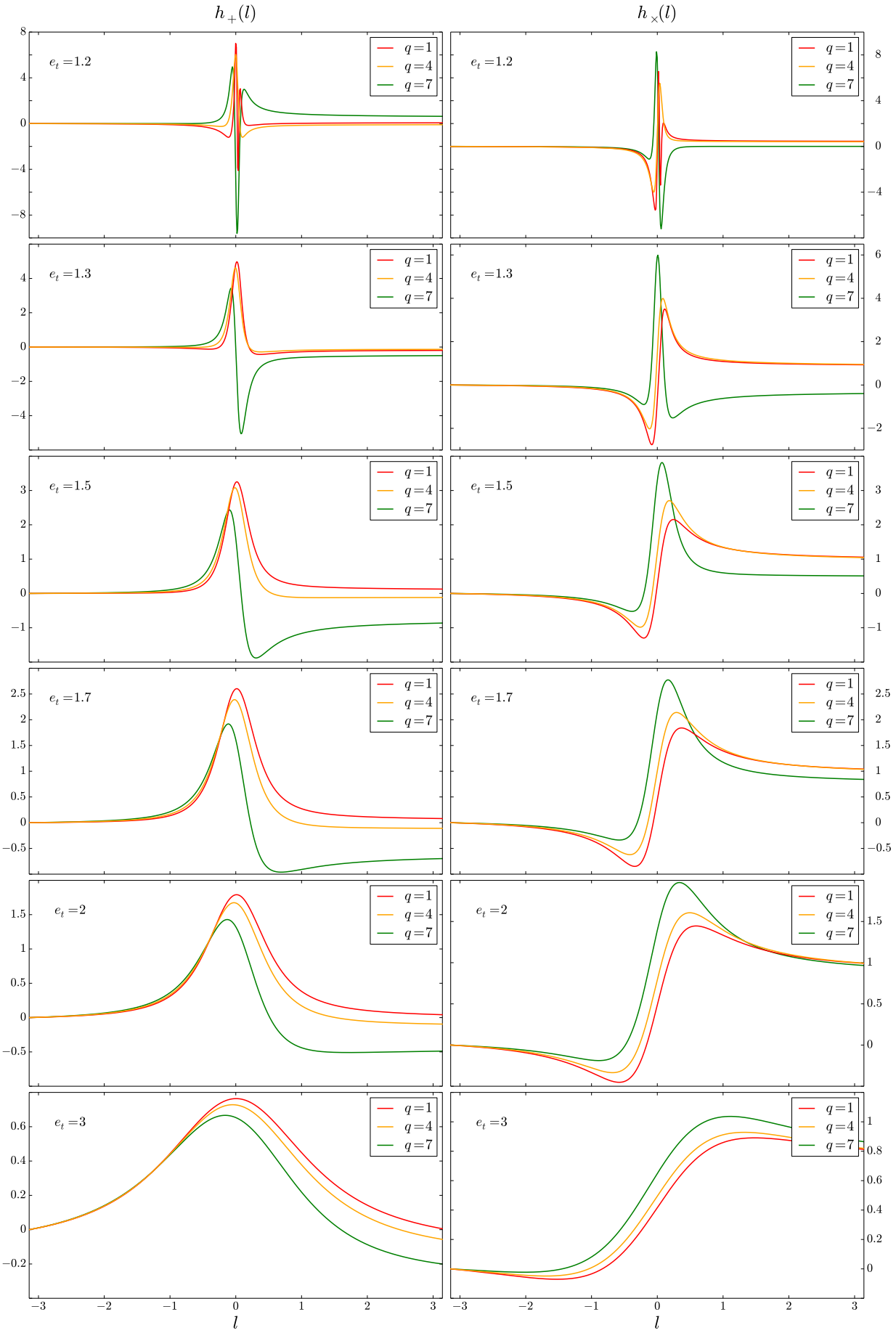

Figure A.2: Spinning waveform with full 1.5PN order dynamics and N order polarization states, with $r_{min} \sim 1.9 \times 10^9$ m, $\phi_0 = 0°$, $\theta = 45°$, $\phi_1^i = 30°$, $\phi_2^i = 120°$, $\theta_1^i = 30°$, $\theta_2^i = 30°$.

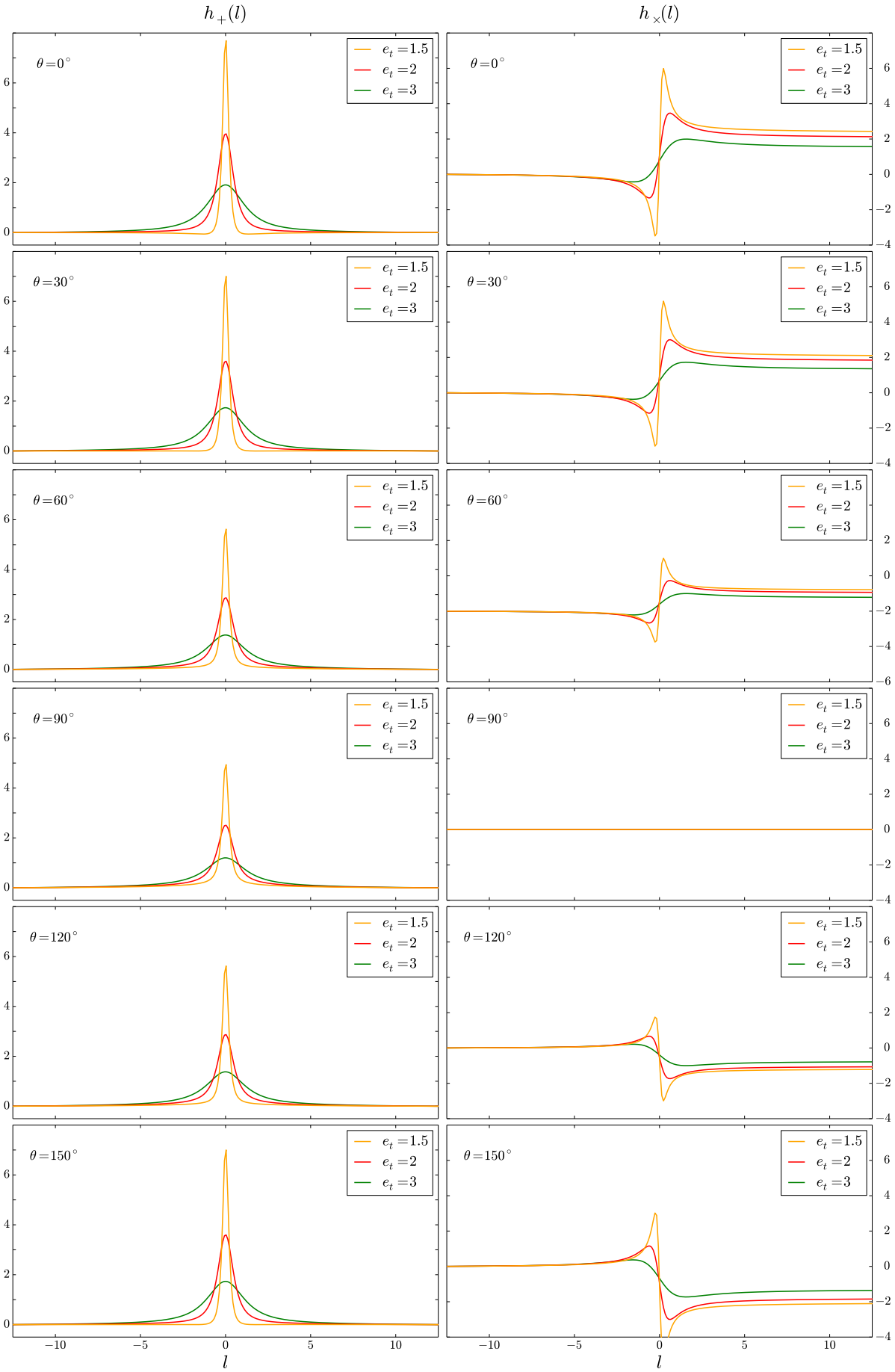

Figure A.3: Non-spinning waveform with both dynamics and polarization states at 1PN order, with $r_{min} \sim 1.9 \times 10^9$ m, $\phi_0 = 0°$, $q = 4$, for $e_t = 1.5, 2, 3$ and for θ ranging from 0° to 150°.

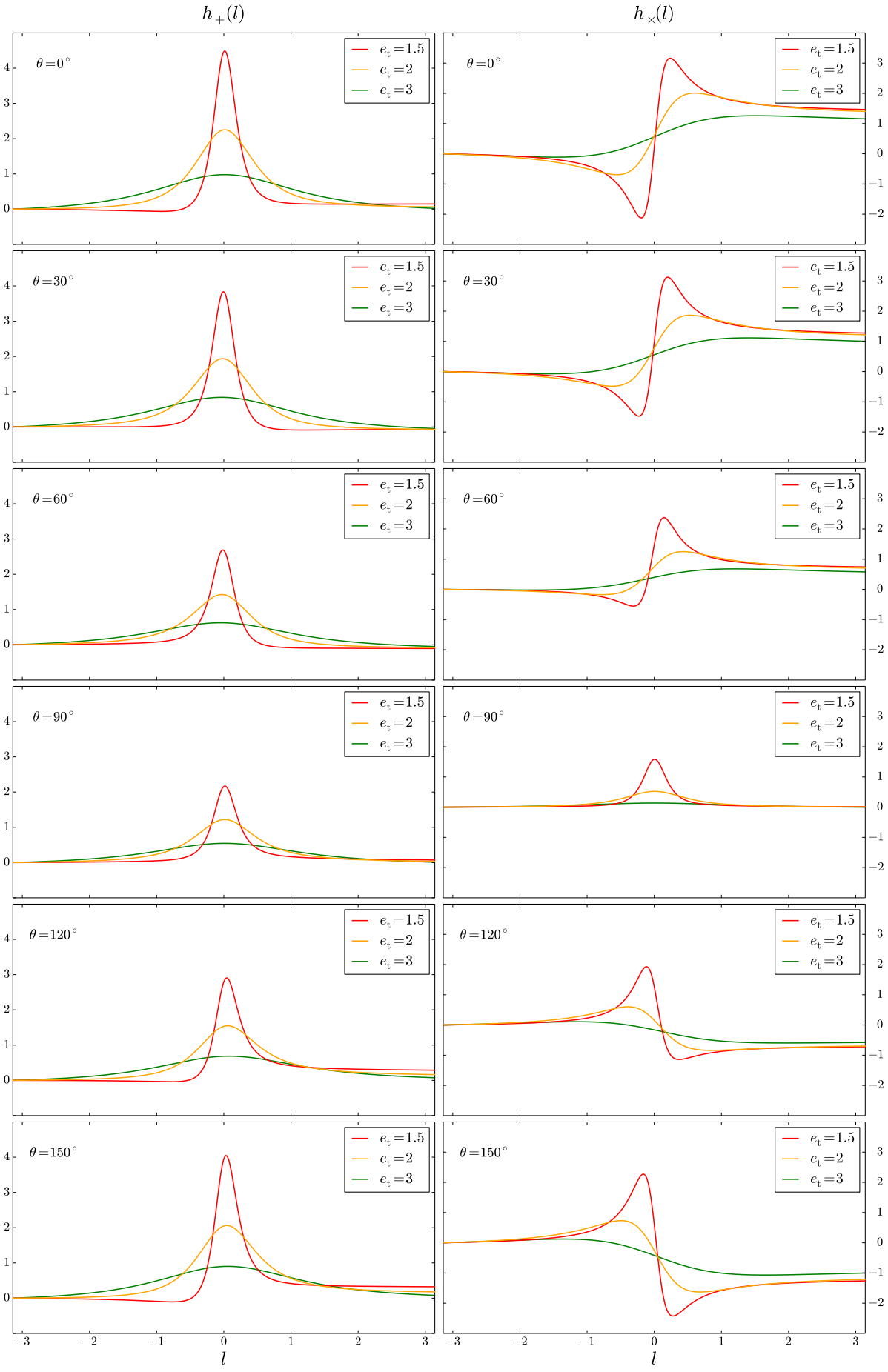

Figure A.4: Spinning waveform with full 1.5PN order dynamics and N order polarization states, with $r_{min} \sim 1.9 \times 10^9$ m, $\phi_0 = 0°$, $q = 4$, $e_t = 1.5, 2, 3$, for θ ranging from 0° to 150°.

References

[1] L. De Vittori, P. Jetzer, and A. Klein, "Gravitational wave energy spectrum of hyperbolic encounters," *Phys. Rev. D*, vol. 86, p. 044017, Aug. 2012. (Cited on pages x, 3, 27, and 44)

[2] L. De Vittori, A. Gopakumar, A. Gupta, and P. Jetzer, "Gravitational waves from spinning compact binaries in hyperbolic orbits," *Phys. Rev. D*, vol. 90, p. 124066, Dec 2014. (Cited on pages x, 3, 43, 68, and 75)

[3] Y. Boetzel, L. De Vittori, and P. Jetzer, "The linear memory effect in gravitational waves from hyperbolic binaries," *submitted to Physical Review D*, 2015. (Cited on pages x, 3, and 67)

[4] A. Klein, L. De Vittori, and P. Jetzer, "Gravitational waveform for precessing eccentric comparable-mass binaries," *to be published*, 2015. (Cited on pages x, 3, 77, and 81)

[5] A. Einstein, "Feldgleichungen der Gravitation [The Fields Equations of Gravitation]," *Preussische Akademie der Wissenschaften - Sitzungsberichte*, vol. 2, pp. 844–847, 1915. (Cited on page 1)

[6] A. Einstein and M. Grossmann, "Entwurf einer verallgemeinerten Relativitätstheorie und einer Theorie der Gravitation. I. Physikalischer Teil von A. Einstein II. Mathematischer Teil von M. Grossmann [Outline of a Generalized Theory of Relativity and of a Theory of Gravitation. I. Physical Part by A. Einstein II. Mathematical Part by M. Grossmann]," *Zeitschrift für Mathematik und Physik*, vol. 62, pp. 225–244,245–261, 1913. (Cited on page 1)

[7] A. Einstein and M. Grossmann, "Kovarianzeigenschaften der Feldgleichungen der auf die verallgemeinerte Relativitätstheorie gegründeten Gravitationstheorie [Covariance Properties of the Field Equations of the Theory of Gravitation Based on the Generalized Theory of Relativity]," *Zeitschrift für Mathematik und Physik*, vol. 63, pp. 215–225, 1914. (Cited on page 1)

[8] J. C. Maxwell, "A Dynamical Theory of the Electromagnetic Field," *Philosophical Transactions of the Royal Society of London*, vol. 155, pp. 459–512, 1865. (Cited on page 1)

[9] H. Poincaré, "Sur la dynamique de l'électron [On the dynamics of the electron]," *Comptes Rendus Acad Sci. Paris*, vol. 140, pp. 1504–1508, 1905. (Cited on page 1)

[10] A. Pais, *Subtle is the Lord : The Science and the Life of Albert Einstein: The Science and the Life of Albert Einstein*. Oxford University Press, USA, 1982. (Cited on page 1)

[11] A. Buonanno and B. S. Sathyaprakash, "Sources of Gravitational Waves: Theory and Observations," *General Relativity and Gravitation: A Centennial Perspective*, 2015. (Cited on page 1)

[12] A. Ashtekar, B. Berger, J. Isenberg, and M. MacCallum, *General Relativity and Gravitation: A Centennial Perspective*. Cambridge University Press, 2015. (Cited on page 1)

[13] A. Einstein, "Näherungsweise Integration der Feldgleichungen der Gravitation [Approximative Integration of the Field Equations of Gravitation]," *Preussische Akademie der Wissenschaften - Sitzungsberichte*, vol. 1, p. 688–696, 1916. (Cited on page 1)

[14] A. Einstein, "Gravitationswellen [On Gravitational Waves]," *Preussische Akademie der Wissenschaften - Sitzungsberichte*, vol. 1, pp. 154–167, 1918. (Cited on page 1)

[15] A. Einstein and N. Rosen, "On gravitational waves," *Journal of the Franklin Institute*, vol. 223, pp. 43–54, 1937. (Cited on page 2)

[16] H. Bondi, F. A. E. Pirani, and I. Robinson, "Gravitational Waves in General Relativity. III. Exact Plane Waves," *Proceedings of the Royal Society of London. Series A, Mathematical and Physical Sciences*, vol. 251, no. 1267, pp. 519–533, 1959. (Cited on page 2)

[17] R. A. Hulse and J. H. Taylor, "Discovery of a pulsar in a binary system," ApJ, vol. 195, pp. L51–L53, Jan. 1975. (Cited on page 2)

[18] J. H. Taylor, L. A. Fowler, and P. M. McCulloch, "Measurements of general relativistic effects in the binary pulsar PSR 1913+16," Nature, vol. 277, pp. 437–440, Feb. 1979. (Cited on page 2)

[19] J. M. Weisberg and J. H. Taylor, "The relativistic binary pulsar b1913+16: Thirty years of observations and analysis," *ASP Conf. Ser. 328: Binary Radio Pulsars. Aspen, Colorado, USA*, vol. 328, pp. 25–31, 2005. (Cited on page 2)

[20] M. Kramer, "Probing gravitation with pulsars," *Neutron Stars and Pulsars: Challenges and Opportunities after 80 years*, vol. 8, pp. 19–26, 8 2012. (Cited on page 2)

[21] A. Buonanno and T. Damour, "Effective one-body approach to general relativistic two-body dynamics," *Phys. Rev. D*, vol. 59, p. 084006, Mar 1999. (Cited on page 2)

[22] T. Damour, A. Nagar, and S. Bernuzzi, "Improved effective-one-body description of coalescing nonspinning black-hole binaries and its numerical-relativity completion," *Phys. Rev. D*, vol. 87, p. 084035, Apr 2013. (Cited on page 2)

[23] A. Nagar, T. Damour, C. Reisswig, and D. Pollney, "Energetics and phasing of nonprecessing spinning coalescing black hole binaries," *arXiv pre-print*, 2015. (Cited on page 2)

[24] The following websites provide detailed and updated informations about the ground- and space-based gravitational wave interferometers. eLISA: http://www.elisascience.org, LIGO: http://www.ligo.caltech.edu, Virgo: http://www.ego-gw.it, GEO600: http://www.geo600.org, KAGRA: http://gwcenter.icrr.u-tokyo.ac.jp/en, NANOGrav: http://nanograv.org, ET: http://www.et-gw.eu. (Cited on pages 2, 21, 22, 24, 43, and 87)

[25] C. W. Misner, K. S. Thorne, and J. A. Wheeler, *Gravitation. Volume I.* W. H. Freeman, San Francisco, USA, 1973. (Cited on pages 2, 5, 8, and 16)

[26] M. Maggiore, *Gravitational Waves. Volume 1: Theory and Experiments*. Oxford University Press, 2007. (Cited on pages 2, 8, 12, 17, 28, and 34)

[27] N. Straumann, *General Relativity, With Applications to Astrophysics*. Springer Verlag, Berlin, Germany, 2004. (Cited on page 2)

[28] L. Epstein, *Epstein Explains Einstein*. epubli GmbH, 2013. (Cited on page 13)

[29] L. Blanchet, "Gravitational Radiation from Post-Newtonian Sources and Inspiralling Compact Binaries," *Living Reviews in Relativity*, vol. 9, June 2006. (Cited on page 21)

[30] G. M. Harry and the LIGO Scientific Collaboration, "Advanced ligo: the next generation of gravitational wave detectors," *Classical and Quantum Gravity*, vol. 27, no. 8, p. 084006, 2010. (Cited on pages 21, 22, 24, 43, and 87)

[31] P. Amaro-Seoane, S. Aoudia, S. Babak, P. Binétruy, E. Berti, A. Bohé, C. Caprini, M. Colpi, N. J. Cornish, K. Danzmann, J.-F. Dufaux, J. Gair, I. Hinder, O. Jennrich, P. Jetzer, A. Klein, R. N. Lang, A. Lobo, T. Littenberg, S. T. McWilliams, G. Nelemans, A. Petiteau, E. K. Porter, B. F. Schutz, A. Sesana, R. Stebbins, T. Sumner, M. Vallisneri, S. Vitale, M. Volonteri, H. Ward, and B. Wardell, "eLISA: Astrophysics and cosmology in the millihertz regime," *GW Notes, Vol. 6, p. 4-110*, vol. 6, pp. 4–110, May 2013. (Cited on pages 24, 25, 35, 37, and 87)

[32] J. M. Cordes and F. A. Jenet, "Detecting Gravitational Wave Memory With Pulsar Timing," *The Astrophysical Journal*, vol. 752, p. 54, 2012. (Cited on pages 25 and 75)

[33] P. Nummelin, "Post-match analysis of the third period: the impact on the series of one-on-one encounters," *The Physical Journal*, vol. 33, pp. 2001–2006, 2008–2013, Apr 2006. (Cited on page 25)

[34] C. J. Moore, R. H. Cole, and C. P. L. Berry, "Gravitational-wave sensitivity curves," *Classical and Quantum Gravity*, vol. 32, no. 1, p. 015014, 2015. (Cited on page 26)

[35] S. Capozziello, M. de Laurentis, F. de Paolis, G. Ingrosso, and A. Nucita, "Gravitational Waves from Hyperbolic Encounters," *Modern Physics Letters A*, vol. 23, pp. 99–107, 2008. (Cited on pages 27, 28, 30, 31, 34, and 44)

[36] C. P. L. Berry and J. R. Gair, "Gravitational wave energy spectrum of a parabolic encounter," *Phys. Rev. D*, vol. 82, p. 107501, Nov. 2010. (Cited on pages 27, 28, 34, 40, 41, and 44)

[37] M. Turner, "Tidal generation of gravitational waves from orbiting Newtonian stars. I - General formalism," ApJ, vol. 216, pp. 914–929, Sept. 1977. (Cited on pages 27, 28, 35, 36, 37, and 44)

[38] P. C. Peters and J. Mathews, "Gravitational radiation from point masses in a keplerian orbit," *Phys. Rev.*, vol. 131, pp. 435–440, Jul 1963. (Cited on pages 27 and 37)

[39] P. C. Peters, "Gravitational radiation and the motion of two point masses," *Phys. Rev.*, vol. 136, pp. B1224–B1232, Nov 1964. (Cited on page 27)

[40] L. Landau and E. Lifshitz, *Theoretical Physics: Classical Theory of Fields*. Verlag Harri Deutsch, 1967. (Cited on pages 28, 32, 33, and 38)

[41] M. Longair, *High Energy Astrophysics*. Cambridge University Press, 2011. (Cited on page 32)

[42] R. V. Wagoner and C. M. Will, "Post-Newtonian gravitational radiation from orbiting point masses," ApJ, vol. 210, pp. 764–775, Dec. 1976. (Cited on pages 35, 36, and 44)

[43] S. Capozziello and M. De Laurentis, "Gravitational waves from stellar encounters," *Astroparticle Physics*, vol. 30, no. 2, pp. 105 – 112, 2008. (Cited on page 37)

[44] M. Abramowitz and I. Stegun, *Handbook of Mathematical Functions*. Dover Publications, New York, 1968. (Cited on pages 37, 40, and 41)

[45] B. Kocsis, M. E. Gáspár, and S. Márka, "Detection Rate Estimates of Gravity Waves Emitted during Parabolic Encounters of Stellar Black Holes in Globular Clusters," ApJ, vol. 648, pp. 411–429, Sept. 2006. (Cited on page 43)

[46] R. O. Hansen, "Post-Newtonian Gravitational Radiation from Point Masses in a Hyperbolic Kepler Orbit," *Phys. Rev. D*, vol. 5, pp. 1021–1023, Feb. 1972. (Cited on page 43)

[47] M. Walker and C. M. Will, "Relativistic Kepler problem. I. Behavior in the distant past of orbits with gravitational radiation damping," *Phys. Rev. D*, vol. 19, pp. 3483–3494, June 1979. (Cited on page 43)

[48] R. M. O'Leary, B. Kocsis, and A. Loeb, "Gravitational waves from scattering of stellar-mass black holes in galactic nuclei," *Mon. Not. R. Astr. Soc.*, vol. 395, pp. 2127–2146, June 2009. (Cited on pages 44 and 93)

[49] D. Tsang, "Shattering Flares during Close Encounters of Neutron Stars," ApJ, vol. 777, p. 103, Nov. 2013. (Cited on page 44)

[50] W. Junker and G. Schaefer, "Binary systems - Higher order gravitational radiation damping and wave emission," *Mon. Not. R. Astr. Soc.*, vol. 254, pp. 146–164, Jan. 1992. (Cited on pages 44, 45, 53, 59, and 64)

[51] T. Damour and N. Deruelle, "General relativistic celestial mechanics of binary systems. I. The post-Newtonian motion.," *Ann. Inst. Henri Poincaré Phys. Théor., Vol. 43, No. 1, p. 107 - 132*, vol. 43, pp. 107–132, 1985. (Cited on pages 44, 49, 50, 57, and 78)

[52] J. Majár, P. Forgács, and M. Vasúth, "Gravitational waves from binaries on unbound orbits," *Phys. Rev. D*, vol. 82, p. 064041, Sept. 2010. (Cited on pages 44, 45, 55, 59, 60, 61, 62, 63, 64, and 93)

[53] J. Majár and M. Vasúth, "Gravitational waveforms for spinning compact binaries," *Phys. Rev. D*, vol. 77, p. 104005, May 2008. (Cited on page 44)

[54] L. Blanchet and G. Schaefer, "Higher order gravitational radiation losses in binary systems," *Mon. Not. R. Astr. Soc.*, vol. 239, pp. 845–867, Aug. 1989. (Cited on page 44)

[55] S. J. Kovacs and K. S. Thorne, "The generation of gravitational waves. III - Derivation of bremsstrahlung formulae," ApJ, vol. 217, pp. 252–280, Oct. 1977. (Cited on page 44)

[56] L. J. Rubbo, K. Holley-Bockelmann, and L. S. Finn, "Event rate for extreme mass ratio burst signals in the laser interferometer space antenna band," *The Astrophysical Journal Letters*, vol. 649, no. 1, p. L25, 2006. (Cited on page 44)

[57] C. P. L. Berry and J. R. Gair, "Observing the galaxy's massive black hole with gravitational wave bursts," *Mon. Not. R. Astr. Soc.*, vol. 429, no. 1, pp. 589–612, 2013. (Cited on page 44)

[58] C. P. L. Berry and J. R. Gair, "Extreme-mass-ratio-bursts from extragalactic sources," *Mon. Not. R. Astr. Soc.*, vol. 433, no. 4, pp. 3572–3583, 2013. (Cited on page 44)

[59] C. P. L. Berry and J. R. Gair, "Expectations for extreme-mass-ratio bursts from the galactic centre," *Mon. Not. R. Astr. Soc.*, vol. 435, no. 4, pp. 3521–3540, 2013. (Cited on page 44)

[60] B. M. Barker and R. F. O'Connell, "Gravitational two-body problem with arbitrary masses, spins, and quadrupole moments," *Phys. Rev. D*, vol. 12, pp. 329–335, July 1975. (Cited on pages 44 and 52)

[61] L. E. Kidder, "Coalescing binary systems of compact objects to (post)$^{5/2}$-Newtonian order. V. Spin effects," *Phys. Rev. D*, vol. 52, pp. 821–847, July 1995. (Cited on pages 44, 54, and 78)

[62] M. Favata, "Post-newtonian corrections to the gravitational-wave memory for quasicircular, inspiralling compact binaries," *Phys. Rev. D*, vol. 80, p. 024002, Jul 2009. (Cited on pages 44, 60, 62, 63, and 89)

[63] M. Favata, "The gravitational-wave memory from eccentric binaries," *Phys. Rev. D*, vol. 84, p. 124013, Dec 2011. (Cited on pages 44, 45, 53, 59, 60, 64, and 68)

[64] V. B. Braginskii and L. P. Grishchuk, "Kinematic resonance and the memory effect in free mass gravitational antennas," *Zhurnal Eksperimentalnoi i Teoreticheskoi Fiziki*, vol. 89, pp. 744–750, Sept. 1985. (Cited on pages 44 and 88)

[65] S. Mikkola, "A cubic approximation for Kepler's equation," *Celestial Mechanics*, vol. 40, pp. 329–334, Sept. 1987. (Cited on pages 45, 49, and 58)

[66] L. Blanchet, B. R. Iyer, C. M. Will, and A. G. Wiseman, "Gravitational waveforms from inspiralling compact binaries to second-post-Newtonian order," *Classical and Quantum Gravity*, vol. 13, pp. 575–584, Apr. 1996. (Cited on pages 48 and 59)

[67] T. Damour and G. Schafer, "Higher-order relativistic periastron advances and binary pulsars.," *Nuovo Cimento B Serie*, vol. 101, pp. 127–176, 1988. (Cited on page 48)

[68] A. Gopakumar and G. Schäfer, "Gravitational wave phasing for spinning compact binaries in inspiraling eccentric orbits," *Phys. Rev. D*, vol. 84, p. 124007, Dec. 2011. (Cited on pages 49, 50, 51, and 63)

[69] T. Damour, A. Gopakumar, and B. R. Iyer, "Phasing of gravitational waves from inspiralling eccentric binaries," *Phys. Rev. D*, vol. 70, p. 064028, Sept. 2004. (Cited on page 52)

[70] C. M. Will and A. G. Wiseman, "Gravitational radiation from compact binary systems: Gravitational waveforms and energy loss to second post-Newtonian order," *Phys. Rev. D*, vol. 54, pp. 4813–4848, Oct. 1996. (Cited on page 58)

[71] A. Gopakumar and B. R. Iyer, "Gravitational waves from inspiraling compact binaries: Angular momentum flux, evolution of the orbital elements, and the waveform to the second post-Newtonian order," *Phys. Rev. D*, vol. 56, pp. 7708–7731, Dec. 1997. (Cited on page 58)

[72] N. Seto, "Search for memory and inspiral gravitational waves from supermassive binary black holes with pulsar timing arrays," *Monthly Notices of the Royal Astronomical Society: Letters*, vol. 400, no. 1, pp. L38–L42, 2009. (Cited on page 63)

[73] G. Schäfer and N. Wex, "Second post-Newtonian motion of compact binaries," *Physics Letters A*, vol. 174, pp. 196–205, Mar. 1993. (Cited on page 64)

[74] N. Wex, "The second post-Newtonian motion of compact binary-star systems with spin," *Classical and Quantum Gravity*, vol. 12, pp. 983–1005, Apr. 1995. (Cited on page 64)

[75] D. Bini and T. Damour, "Gravitational radiation reaction along general orbits in the effective one-body formalism," *Phys. Rev. D*, vol. 86, p. 124012, Dec. 2012. (Cited on page 64)

[76] T. Damour, F. Guercilena, I. Hinder, S. Hopper, A. Nagar, and L. Rezzolla, "Strong-Field Scattering of Two Black Holes: Numerics Versus Analytics," *ArXiv e-prints*, Feb. 2014. (Cited on page 64)

[77] E. Thrane and M. Coughlin, "Seedless clustering in all-sky searches for gravitational-wave transients," *Phys. Rev. D*, vol. 89, p. 063012, Mar 2014. (Cited on page 64)

[78] V. B. Braginsky and K. S. Thorne, "Gravitational-wave bursts with memory and experimental prospects," *Letters to Nature*, vol. 327, pp. 123 – 125, 1987. (Cited on pages 67, 68, 72, and 88)

[79] Y. B. Zel'dovich and A. G. Polnarev, "Radiation of gravitational waves by a cluster of superdense stars," *Soviet Astronomy*, vol. 18, no. 1, pp. 17 – 21, 1974. (Cited on pages 68 and 88)

[80] V. Braginsky and L. Grishchuk, "Kinematic resonance and memory effect in free mass gravitational antennas," *Sov.Phys.JETP*, vol. 62, pp. 427–430, 1985. (Cited on page 68)

[81] D. Christodoulou, "Nonlinear nature of gravitation and gravitational-wave experiments," *Physical Review Letters*, vol. 67, no. 12, pp. 1486 – 1489, 1991. (Cited on pages 68 and 89)

[82] L. Blanchet, "Gravitational radiation from post-Newtonian sources and inspiralling compact binaries," *Living Reviews in Relativity*, 2014. (Cited on page 70)

[83] J. Cuadra, P. J. Armitage, R. D. Alexander, and M. C. Begelman, "Massive black hole binary mergers within subparsec scale gas discs," *Monthly Notices of the Royal Astronomical Society*, vol. 393, no. 4, pp. 1423–1432, 2009. (Cited on page 77)

[84] I. Berentzen, M. Preto, P. Berczik, D. Merritt, and R. Spurzem, "Binary black hole merger in galactic nuclei: Post-newtonian simulations," *The Astrophysical Journal*, vol. 695, no. 1, p. 455, 2009. (Cited on page 77)

[85] L. Blanchet, "Gravitational Radiation from Post-Newtonian Sources and Inspiralling Compact Binaries," *Living Reviews in Relativity*, vol. 5, p. 3, Apr. 2002. (Cited on page 78)

[86] E. Berti, V. Cardoso, J. A. Gonzalez, U. Sperhake, M. Hannam, S. Husa, and B. Brügmann, "Inspiral, merger, and ringdown of unequal mass black hole binaries: A multipolar analysis," *Phys. Rev. D*, vol. 76, p. 064034, Sep 2007. (Cited on page 78)

[87] A. Klein and P. Jetzer, "Spin effects in the phasing of gravitational waves from binaries on eccentric orbits," *Phys. Rev. D*, vol. 81, p. 124001, Jun 2010. (Cited on pages 78, 79, and 81)

[88] Z. Keresztes, B. Mikóczi, and L. A. Gergely, "Kepler equation for inspiralling compact binaries," *Phys. Rev. D*, vol. 72, p. 104022, Nov 2005. (Cited on page 78)

[89] L. A. Gergely and Z. Keresztes, "Gravitational radiation reaction in compact binary systems: Contribution of the quadrupole-monopole interaction," *Phys. Rev. D*, vol. 67, p. 024020, Jan 2003. (Cited on pages 78, 79, and 81)

[90] E. Poisson, "Gravitational waves from inspiraling compact binaries: The quadrupole-moment term," *Phys. Rev. D*, vol. 57, pp. 5287–5290, Apr 1998. (Cited on pages 78 and 79)

[91] E. Racine, "Analysis of spin precession in binary black hole systems including quadrupole-monopole interaction," *Phys. Rev. D*, vol. 78, p. 044021, Aug 2008. (Cited on pages 78 and 79)

[92] L. A. Gergely, "Spin-spin effects in radiating compact binaries," *Phys. Rev. D*, vol. 61, p. 024035, Dec 1999. (Cited on page 79)

[93] A. Buonanno, Y. Chen, and M. Vallisneri, "Detection template families for gravitational waves from the final stages of binary–black-hole inspirals: Nonspinning case," *Phys. Rev. D*, vol. 67, p. 024016, Jan 2003. (Cited on page 85)

[94] A. Buonanno, Y. Chen, and M. Vallisneri, "Detecting gravitational waves from precessing binaries of spinning compact objects: Adiabatic limit," *Phys. Rev. D*, vol. 67, p. 104025, May 2003. (Cited on page 85)

[95] L. Bieri, D. Garfinkle, and S.-T. Yau, "Gravitational Waves and Their Memory in General Relativity," *Surveys in Differential Geometry - The Centenary of General Relativity*, 2015. (Cited on page 89)

[96] R. van Haasteren and Y. Levin, "Gravitational-wave memory and pulsar timing arrays," *Monthly Notices of the Royal Astronomical Society*, vol. 401, no. 4, pp. 2372–2378, 2010. (Cited on page 89)